


Summer 7-10-2018

# Developing Droplet Based 3D Cell Culture Methods to Enable Investigations of the Chemical Tumor Microenvironment

Jacqueline A. De Lora

*University of New Mexico - Main Campus*

Follow this and additional works at: [https://digitalrepository.unm.edu/biom\\_etds](https://digitalrepository.unm.edu/biom_etds)

 Part of the [Bioimaging and Biomedical Optics Commons](#), [Biological Engineering Commons](#), [Biomaterials Commons](#), [Biomedical Devices and Instrumentation Commons](#), [Biophysics Commons](#), [Biotechnology Commons](#), [Cancer Biology Commons](#), [Cell Biology Commons](#), [Disease Modeling Commons](#), and the [Molecular, Cellular, and Tissue Engineering Commons](#)

---

## Recommended Citation

De Lora, Jacqueline A.. "Developing Droplet Based 3D Cell Culture Methods to Enable Investigations of the Chemical Tumor Microenvironment." (2018). [https://digitalrepository.unm.edu/biom\\_etds/186](https://digitalrepository.unm.edu/biom_etds/186)

This Dissertation is brought to you for free and open access by the Electronic Theses and Dissertations at UNM Digital Repository. It has been accepted for inclusion in Biomedical Sciences ETDs by an authorized administrator of UNM Digital Repository. For more information, please contact [disc@unm.edu](mailto:disc@unm.edu).

Jacqueline A. De Lora

*Candidate*

---

Biomedical Sciences

*Department*

---

This dissertation is approved, and it is acceptable in quality and form for publication:

*Approved by the Dissertation Committee:*

Helen J. Hathaway, Chairperson

---

James P. Freyer

---

Diane S. Lidke

---

Andrew P. Shreve

---

**DEVELOPING DROPLET BASED 3D CELL CULTURE METHODS  
TO ENABLE INVESTIGATIONS OF THE CHEMICAL TUMOR  
MICROENVIRONMENT**

**BY**

**JACQUELINE ALEXANDRIA DE LORA**

B.S., Biology, University of New Mexico, 2011  
B.A., Chemistry, University of New Mexico, 2011

**DISSERTATION**

Submitted in Partial Fulfillment of the  
Requirements for the Degree of

**DOCTOR OF PHILOSOPHY**

**BIOMEDICAL SCIENCES**

The University of New Mexico  
Albuquerque, New Mexico

**July 2018**

## **ACKNOWLEDGMENTS**

I would like to acknowledge my family and friends for their constant support and acceptance throughout every endeavor I have ever undertaken, academic and otherwise. You all have always encouraged, inspired, questioned and most of all cared for me in the best ways possible. Dad, you taught me about dedication, loyalty, and how to care for other humans regardless of circumstance. Moma, you have been a constant source of strength and spirituality, helping me to find the path in life that brings the most happiness and peace. Adam, you are brilliant and always motivating me to be better. I thank you all from the bottom of my heart.

To my husband, Gregory Edward Smith, I cannot imagine a better climbing nor life partner. Your inherent understanding of who I am has made my adventure of becoming a scientist and engineer possible. You have been there with me through all of the valleys and peaks, helping to remind me of the beauty of the route itself in addition to the top out, the summit, the doctorate, the final accomplishment of the goal (whatever it might have been). Thank you for always coming home from work and being happy to see me and the pups, for fixing the espresso machine and supporting my love for coffee/beer/Scotch, for our home both on wheels (Ekroo) and on land (Casa Bonita), for going with me on countless explorations and sharing the experiences of the most amazing places on this Earth. You are the love of my life and the one who makes it all worthwhile.

The writing would never have been as much fun without the pups lying under the desk and cuddling up. Marbell- you are one fearless blind dog and you remind me to take the leap into the unknown daily. Torridon- you are one sweet

spotted dog, reminding me to keep my eye on the ball and to still feel the accomplishment even if the catch is on the rebound. Your companionship and love has brought me through the hardest of times.

I owe my abilities to think logically, to consider all of the perspectives of a problem, and to discover new approaches when the current route isn't working out to my mentors, Jim Freyer and Andy Shreve. I thank you both for initially recognizing the potential I had to become a successful scientist and engineer, for letting me carve my own path, and for spending the time and energy to make sure that I kept/got back on track. To my extended mentoring team, Helen Hathaway and Diane Lidke, I thank you both for keeping open minds to new ideas and for making sure my aspirations to bring engineering into the picture were biologically realistic and feasible. Jessica Houston, your support over the years as a role model and in the reading and editing of my dissertation has made me a better scientist and more organized writer. To my more recent mentor, Nick Carroll, I thank you for providing the opportunity to rediscover cooperative research and to share a love for droplets.

Finally, the greater community and research environment at the Center for Biomedical Engineering at UNM has enabled me to grow into the researcher that I am today. Each and every undergraduate who I mentored and graduate student who I collaborated with made this work achievable and enjoyable. I thank you all for the undying support and camaraderie over the past years. You all made the lab a place to take my creativity and sometimes outrageous ideas to experiment with and for that I will forever be grateful.

**DEVELOPING DROPLET BASED 3D CELL CULTURE METHODS TO  
ENABLE INVESTIGATIONS OF THE CHEMICAL TUMOR  
MICROENVIRONMENT**

**by**

**JACQUELINE ALEXANDRIA DE LORA**

B.S., Biology, University of New Mexico, 2011

B.A., Chemistry, University of New Mexico, 2011

Ph.D., Biomedical Sciences 2018

**ABSTRACT**

Adaptation of cancer cells to changes in the biochemical microenvironment in an expanding tumor mass is a crucial aspect of malignant progression, tumor metabolism, and drug efficacy. In vitro, it is challenging to mimic the evolution of biochemical gradients and the cellular heterogeneity that characterizes cancer tissues found in vivo. It is well accepted that more realistic and controllable in vitro 3D model systems are required to improve the overall cancer research paradigm and thus improve on the translation of results, but multidisciplinary approaches are needed for these advances. This work develops such approaches and demonstrates that new droplet-based cell-encapsulation techniques have the ability to encapsulate cancer cells in droplets for standardized and more realistic

3D cell culture and cancer biology applications. Three individual droplet generating platforms have been designed and optimized for droplet-based cell encapsulation. Each has its own advancements and challenges. Together, however, these technologies accomplish medium to high-throughput generation (10 droplets/second to 25,000 droplets/second) of biomaterial droplets for encapsulation of a range of cell occupancies (5 cells/droplet to 400 cells/droplet). The data presented also demonstrates the controlled generation of cell-sized small droplets for biomolecule compartmentalization, droplets with diameters ranging between 100-400  $\mu\text{m}$  depending on device parameters, and the generation of instant spheroids. Standardized assays for analyzing cells grown within these new 3D environments include proliferation assays of cells grown in mono- and co-cultures, the generation of large and uniform populations of scaffold supported multicellular spheroids, and a new system for culturing encapsulated cells in altered environmental conditions.

## TABLE OF CONTENTS

List of Figures.....	ix
List of Tables.....	xi
Chapter 1 Tools for 3D Cell Culture in Cancer Research.....	1
1.1 Motivation for the Dissertation.....	2
1.2 Heterogeneity in the Tumor Microenvironment and Therapy Efficacy.....	6
1.3 Gradients and Tumor Heterogeneity.....	9
1.4 Hypoxia in the Tumor Microenvironment.....	16
1.5 Oxygen and the Hypoxia Inducible Factor Pathway.....	21
1.6 pH and the Hypoxia Inducible Factor Pathway.....	24
1.7 Conclusions and Outline of Subsequent Chapters.....	29
1.8 List of References .....	31
Chapter 2 Content and Contributions.....	41
2.1 Content in chapters 3-7 and Contributions Made.....	42
Chapter 3 High-Throughput Acoustic Droplet Generation in Air.....	47
3.1 Controlled Mass-Production of Droplets.....	48
3.2 Device Designs.....	51
3.3 Instrumentation Operation.....	54
3.4 Biocompatible Droplet Generation.....	59
3.5 Chemistry and Collection for Stable Droplet Formation.....	70
3.6 Discussion and Future Directions.....	81
3.7 List of References.....	83



Chapter 4	Microfluidics Droplet Generation.....	85
4.1	Generating Droplets with an Improved Microfluidics Approach.....	86
4.2	Biocompatible Device Operation Conditions.....	88
4.3	Cell Suspension and Encapsulation.....	98
4.4	Cell Growth Over Time in Droplets.....	107
4.5	Discussion and Future Directions.....	109
4.6	List of References.....	111
Chapter 5	Centrifugal Droplet Generation for Cell Encapsulation.....	113
5.1	Robust Droplet Generation by Centrifugal Synthesis.....	114
5.2	Centrifuge Tube Assemblies and Hybrid Nozzle Designs.....	117
5.3	Cell-Sized Droplets.....	128
5.4	Cell Encapsulation by Centrifugal Droplet Generation.....	131
5.5	Discussion and Future Directions.....	139
5.6	List of References.....	140
Chapter 6	Droplet Based Cell Encapsulation in Cancer Research.....	142
6.1	Realistic and Standardized Approaches for Cancer Research.....	143
6.2	Adapting 2D Growth Assays to 3D Cell Culture.....	148
6.3	Culture of Instant Spheroids.....	162
6.4	Altered Chemical Environments System.....	165
6.5	Discussion and Future Directions.....	174
6.6	List of References.....	175
Chapter 7	Conclusion of the Dissertation.....	178
7.1	Concluding Remarks for the Dissertation.....	179

## LIST OF FIGURES

Figure 1.1 Homeostatic Tissue.....	10
Figure 1.2 Tumorigenic Tissue.....	11
Figure 1.3 Conventional Model Systems.....	13
Figure 1.4 Hypoxic Tissue.....	18
Figure 1.5 Regulation of HIF-1 $\alpha$ .....	23
Figure 1.6 Tumor Metabolism.....	28
Figure 3.1 Dual Channel Device.....	53
Figure 3.2 Instrumentation Schematic.....	58
Figure 3.3 Alginate Crosslinking.....	60
Figure 3.4 Dual Channel Flow Rates.....	63
Figure 3.5 Hydrodynamic Focusing.....	64
Figure 3.6 Dual Channel Droplets in Air.....	65
Figure 3.7 Single Channel Optimization.....	68
Figure 3.8 Single Channel Droplets in Air.....	69
Figure 3.9 Improved Single Channel Device Operations.....	72
Figure 3.10 Rigid Body Collection.....	74
Figure 3.11 Characterization of Droplet Spacing in Air.....	76
Figure 3.12 Rigid Body Collected Droplets.....	78
Figure 3.13 Attempted Cell Encapsulation.....	80
Figure 4.1 Biopolymer Enrichment.....	89
Figure 4.2 Microfluidics Device Schematic.....	91
Figure 4.3 Characterization of a Microfluidics Device.....	96

Figure 4.4 Device Operating Regimes.....	97
Figure 4.5 Live/Dead Assay.....	102
Figure 4.6 Encapsulation and Proliferation Results.....	106
Figure 5.1 Centrifugal Droplet Generation.....	116
Figure 5.2 Device Schematic.....	119
Figure 5.3 Droplet Generating Flow Regimes.....	121
Figure 5.4 Hybrid Nozzle Characterization.....	124
Figure 5.5 Hybrid Nozzle Optimization.....	125
Figure 5.6 Cell-Sized Droplets.....	130
Figure 5.7 A549 WT Droplet Distribution.....	134
Figure 5.8 A549 KO Droplet Distribution.....	135
Figure 5.9 Instant Spheroid Formation.....	138
Figure 6.1 Droplet-Based Bioassay Applications.....	147
Figure 6.2 Growth Assay Methodologies.....	151
Figure 6.3 HKO3 2D Growth Assay Results.....	153
Figure 6.4 A549 2D Growth Assay Results.....	154
Figure 6.5 A549 WT Qualitative 3D Growth Assay.....	157
Figure 6.6 A549 KO Qualitative 3D Growth Assay.....	158
Figure 6.7 Coculture Proof-of-Principle Results.....	161
Figure 6.8 Instant Spheroid 3D Growth Assay.....	164
Figure 6.9 Experimental Design for Altered Environments.....	166
Figure 6.10 Experimental System for Altered Environments.....	168
Figure 6.11 Preliminary Altered Environments Results.....	171

## LIST OF TABLES

Table 3.1 Table of Flow Rates.....	63
Table 3.2 Hydrodynamic Focusing Table.....	64

## **Chapter 1**

### **Tools for 3D Cell Culture in Cancer Research**

## 1.1 Motivation for the Dissertation

*Droplet based cell culture has the potential to become integrated into standard lab practices as a robust and reliable 3D cell culture platform. Use of these techniques will enable relevant studies of the heterogeneity within the tumor microenvironment.*

The use of animal modeling, 2D cell culture, preestablished 3D culturing methods, and mathematical modeling has facilitated many pioneering studies and overall advancements in understanding the fundamental aspects of the tumor microenvironment.<sup>1</sup> However there is a need and opportunity for the development of manipulable, multivariable model systems that better mimic, control, and measure cellular and chemical heterogeneities in the tumor microenvironment. Using droplet-based cell encapsulation as the foundation for these types of in vitro multivariable model systems provides a platform to investigate cellular behavior in a more complex yet controllable environment. **The over-arching motivation of this dissertation is that improvement in droplet-based cell encapsulation techniques will enable more controllable and realistic investigations of the heterogeneous environments in which cancer develops.**

The main scope of this dissertation is the design and implementation of droplet generating technologies for cell encapsulation and the development of standardized cancer biology applications. Although the actual investigation of a specific biomedical question and hypothesis is out of the scope of this dissertation,

it is worth mentioning that the 3D cell culture technologies designed herein are applicable to biomedical hypotheses that concern topics such as the generation of cellular and biochemical heterogeneities within the tumor microenvironment. The content within this dissertation begins the development of standardized 3D cell culture methods to evaluate tumor cell proliferation and survival in combinatorial acidic/hypoxic microenvironmental conditions. Eventually, cells cultured in 3D droplet-based and altered biochemical environments will enable the investigation of the changes in cellular expression patterns that could arise as mediated by different transcription factors, such as HIF-1 $\alpha$  (hypoxia inducible factor-1 $\alpha$ ).

The remainder of Chapter 1 provides the biological motivation for the development of improved 3D cell culture techniques and methodology by focusing on: the principles of evolutionary biology applied to cancer therapy efficacy (Section 1.2); the generation of biochemical and cellular heterogeneities (Section 1.3); the biology of hypoxia in the tumor microenvironment (Section 1.4); regulation of the hypoxia inducible factor pathway by oxygen (Section 1.5); and the potential influence of pH and metabolism on HIF-1 $\alpha$  (Section 1.6). The interaction of these topics provides an exemplary biomedical system that would be well suited to be addressed using the improved 3D *in vitro* approaches described by this dissertation, which will eventually enable controlled studies of HIF-1 $\alpha$  mediated responses to both coupled and uncoupled variations of hypoxia and acidosis.<sup>2,3</sup>

The development of droplet-based cell encapsulating technologies as well as the standardized cancer biology applications that validate the developed technologies is achieved through two Specific Aims:

***Specific Aim 1: Development and implementation of droplet generation technologies for cell encapsulation***

Droplet generating instrumentation and methodology has been developed and demonstrated to encapsulate cells for 3D cell culture. Chapters 3, 4, and 5 each describes a unique approach for droplet-based cell encapsulation. Specifically, high-throughput droplet generation in the air is addressed in Chapter 3, microfluidic droplet generation using loudspeaker acoustics and water-in-water emulsion chemistries is addressed in Chapter 4, and centrifugal droplet generation for mass production of cell encapsulating droplets is described in Chapter 5. In each technology development chapter, flow rate measurements, parameter optimizations, and overall system implementations are discussed. Droplet populations are evaluated using microscopy and image processing to determine the average diameter of the populations. The metric of droplet diameter serves as a benchmark for the success or improvement of the droplet generating technology. Generally speaking, these developments in droplet generating technologies make advancements in multidisciplinary fields in terms of overall cost, simplicity of device fabrication, high throughput operation, monodispersity, biocompatibility, recovery of intact cells, and overall robustness of the platforms.

***Specific Aim 2: Development of standardized biological assays to measure droplet-based 3D cell cultures***

Cancer research applications are being developed to measure qualities of cells that have been encapsulated and grown (using the approaches described in Chapters 3-5). Chapter 6 focuses on the development, implementation, and in



some cases challenges of biological assays including proliferation assays in 2D vs 3D cell mono- and co-cultures, the formation of multicellular tumor spheroids either instantly by initial high cell loading in droplets or over time with initial low cell loading, and the establishment of 3D culture systems with altered biochemical microenvironments. In general, droplet populations are evaluated with the methods described in Specific Aim 1. Cell populations encapsulated in droplets are measured by dissolving the droplet scaffolding material, isolating the cell population, and analyzing the cells by cell counting and flow cytometry. Chapter 7 concludes the dissertation with a discussion on droplet-based technologies for the investigation of biomedical questions including challenges to be overcome and future directions.

## 1.2 Heterogeneity in the Tumor Microenvironment and Therapy Efficacy

*Principles from evolutionary biology describe why tumor heterogeneity directly impacts the success of therapeutic interventions.*

Cancer is initiated by hyperplasia or uncontrolled reproduction of cells in the microenvironment, driving the development of malignancies affecting millions of individuals worldwide.<sup>4</sup> The economic and social impact of cancer is significant and increasing despite the money and efforts directed at eradication and control over advanced disease states; in 2010 the disease cost approximately US\$ 1.16 trillion and in 2015 was the cause of 1 in 6 deaths globally (8.8 million deaths total).<sup>5</sup> These statistics will be improved by advancing the toolsets cancer researchers use to study the tumor microenvironment and therapeutic efficacy. Complexity within the tumor microenvironment is derived from the increase in cell number offsetting the homeostatic biochemical microenvironment, establishing multifactorial gradients that are either unidentified or poorly understood. For example, many combinatorial biochemical microenvironment parameters influence spatial-temporal dynamics that control cellular behavior (signaling pathways, transcriptional response elements, genetic instability etc.) but have yet to be identified for the purpose of therapeutic intervention. Despite this prodigious context, some simple relationships in the TME have been established, and these have improved our understanding of the complex cellular interactions.<sup>6</sup>

Conventionally, cancer is described as a disease of the genes. A large body of work *in vitro* uses basic experimental model systems (for example, by harvesting cells from a biopsy, culturing by 2D monolayer and sequencing approaches for analysis) to investigate specific genes or mutations and design therapeutic interventions that specifically target these genotypes.<sup>7</sup> This silver bullet idea has yet to be proven globally effective at treating and much less curing the multifaceted disease.<sup>8</sup> Approaching cancer from the framework of development based solely on genetic information neglects the nature of the situation; cancer develops in a dynamically evolving chemical microenvironment with combinatorial selection pressures propagating malignant phenotypes. Darwinian principles of natural selection (namely, phenotypic variation among individuals within a population is heritable, and individuals with heritable traits better suited to environmental pressures will survive) can be used to explain the evolution of heterogeneous phenotypes, genomic instability, and the inability of targeted therapies to comprehensively eradicate a single tumor.<sup>6,9-11</sup>

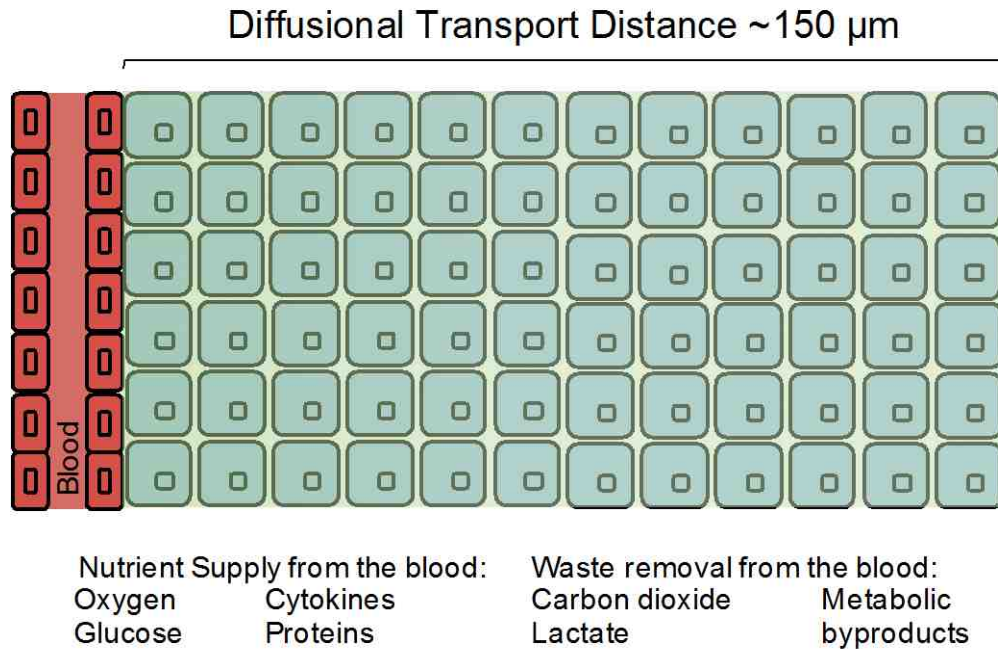
Contemplating cancer through the lens of evolution starts with identifying environmental selection pressures (i.e. hypoxia, acidosis, depleted nutrient availability etc.) working in combination and the adaptive cellular survival mechanisms (i.e. change in genetic expression patterns) that ensue. It then becomes more tractable to map these environmentally derived phenotypes to tissue architecture as well as to genetics and identify therapeutic strategies that could be effective over the wide range of heterogeneity observed in solid tumors. This goal of relating changes in the chemical tumor microenvironment, in genetic

and protein expression, and in the ability of a drug to be effective needs to be evaluated using model systems that can provide more realistic context. Finally, the research paradigm of studying cancer primarily in 2D cell culture followed by preclinical drug discovery investigations needs to be modernized to implement advancements made in multidisciplinary fields. Developing new 3D cell culture methods will enable correlative studies of environmental selection pressures with cellular responses to produce more translatable outcomes.

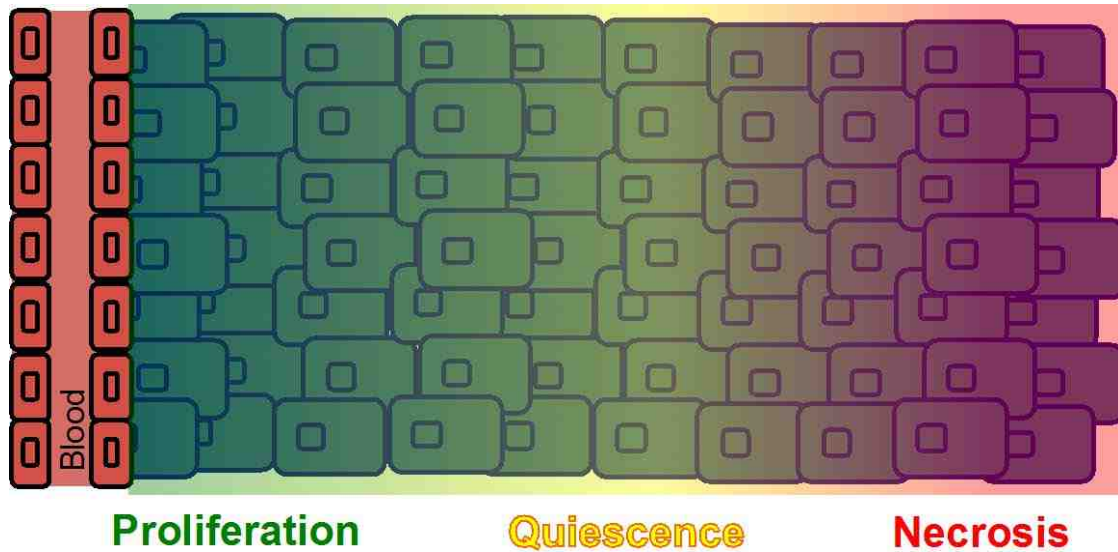
### 1.3 Gradients and Tumor Heterogeneity

*Conventional biomedical research methods are insufficient to generate, control, and investigate correlations within the biochemical tumor microenvironment that develop because of altered cellular metabolism. Cellular adaptations that arise in response further propagate heterogeneity within a tumor and directly impact therapeutic outcomes.*

Cells in a tissue field are conceptually located between nutrient sources and waste removal systems (i.e. the vasculature) that are organized such that cells are no farther than ~150  $\mu\text{m}$  from the nearest blood vessel (Figure 1.1).<sup>12</sup> Cells within this local and radial diffusional transport distance of 150  $\mu\text{m}$  are under strict homeostatic mechanisms that include (1) proliferation regulation; (2) cellular turnover by apoptosis; (3) tightly orchestrated genetic expression; (4) energetics by aerobic metabolism; and (5) ordered extracellular matrix (ECM) and vasculature; thus, the biochemical microenvironment is resistant to large shifts. In contrast, tumorigenic tissues have malfunctioning homeostatic mechanisms. First and foremost, proliferation regulation breaks down, which leads to uncontrolled reproduction of cells, and therefore the proliferative tissue develops nutrient and waste supply and removal demands, respectively, that exceed the capabilities of preestablished vasculature. In addition, genetic regulatory signals are largely ineffectual, cell turnover shifts to necrosis, the ECM and vasculature become chaotic, metabolism shifts to glycolysis and the biochemical microenvironment is



**Figure 1.1 Homeostatic Tissue.** Idealization of a cells in a tissue field with ordered tissue architecture and commensurate time scales for diffusional transport and metabolic processes, leading to minimal accumulations or depletions of biochemicals (wastes and nutrients, respectively). This diagrammatic representation shows the vasculature blood supply on the left-hand side next to a structurally ordered and uniform tissue field with the green overlay demonstrating the uniformity of the biochemical environment (some gradients do arise but for the purpose of comparison to a tumorigenic tissue as depicted in Figure 1.2, small scale gradients are not pictured here).

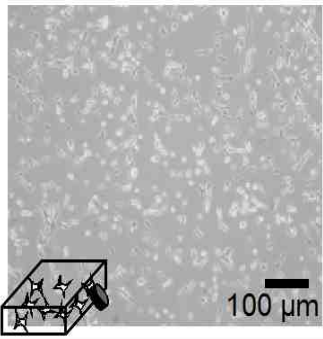
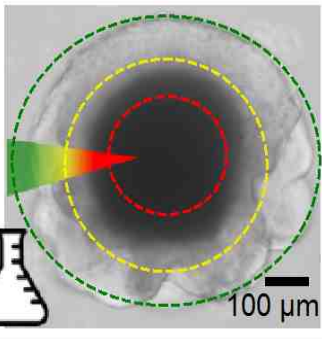
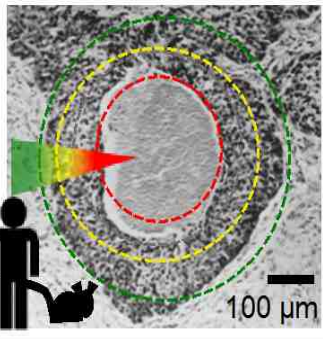


**Figure 1.2 Tumorigenic Tissue.** In early stage tumor progression, biochemical microenvironmental gradients arise when metabolic consumption exceeds diffusional transport and nutrient supply. These biochemical gradients cause the development of heterogeneous phenotypes in the tumor microenvironment. As the figure illustrates, the cells in close proximity to the vasculature are exposed to a nutrient rich perfusate that enables a proliferative phenotype (green overlay). Farther away from the vasculature, the nutrient supply is depleted by the proliferative cell metabolism upstream and thus a quiescent, non-proliferative phenotype is observed (yellow overlay). Finally, necrosis develops at radial distances above  $\sim 150 \mu\text{m}$  away from the vasculature (red overlay) because of extreme nutrient depletion and waste accumulation.

subjected to large variations.<sup>13</sup> As seen in Figure 1.2, these chemical microenvironment variations exist as gradients and give rise to (1) a proliferative region close to the nutrient source with abundant nutrients and high metabolic rates; (2) quiescent cells farther away from the source and in a nutrient depleted environment due to the metabolic activity that occurred upstream; and (3) farthest away from the blood vessel, waste accumulation and necrosis. In short, the dynamic biochemical environment in a tumor causes phenotypic heterogeneity to become the prevailing qualitative characteristic.<sup>14</sup> It is now well accepted that heterogeneity in the TME plays a critical role in the progression of cancer, however existing techniques are not suited to study this heterogeneity.

Different approaches are used to model the tumor microenvironment for analyzing changes in genetic and protein expression in response to changes in the biochemical microenvironment, yet many are insufficient. Existing technologies are lacking in many critical aspects to achieve this goal (Figure 1.3). Models *in vivo*, although currently the gold standard in pre-clinical research, are expensive, complex, and have uncontrollable parameters that make establishing robust model systems intractable.<sup>15,16</sup> For example, mouse xenograft models of cancer (human cell-line implantation) have short-comings including (1) unrealistically higher metabolic and proliferative rates of cells in the system as well as the small size of the organism and shorter lifespan in comparison to the humans it is meant to model; (2) defined lack of parametric control for mechanistic studies because the system is too complex to control all possible variables; and (3) the economical and



	Monolayer Cell Culture	Multicellular Spheroid	<i>In Vivo</i>
Model System			
Advantages	Some techniques measure <b>oxygen</b> consumption rate and extracellular <b>acidification</b> rate Up to 96 well plate <b>throughput</b>	Cellular <b>heterogeneity</b> due to microenvironment Measurements of <b>oxygen</b> by microelectrode	Real tumor Clinical relevance
Disadvantages	Cell plated in a 2D <b>monolayer culture</b> . <b>No gradient information</b> <b>Lacking complexity</b>	Correlation to cellular physiology requires <b>destruction</b> of spheroid Needs improvement in size <b>uniformity</b> and formation	<b>Uncontrollable</b> parameters Measurements in real-time are <b>technically challenging</b> End point assays are <b>destructive</b> /require sacrifice <b>Ethical</b> considerations

**Figure 1.3 Conventional Model Systems.** Diagrammatic comparison of the research paradigm currently accepted in biomedical investigations from 2D to 3D cell culture through pre-clinical and clinical studies.

ethical concerns of the system.

In comparison, widespread 2D cell culture *in vitro* systems are too simplistic to accurately reflect a solid tumor and while being more ethically acceptable, have recently been proven to produce directly untranslatable results.<sup>17</sup> 2D cell culture systems are deficient in that (1) cells are completely removed from the context of a 3D tissue architecture and made to grow on treated polystyrene or glass surfaces; (2) the biochemical environment is by design free of gradients, nutrient enriched past realistic physiological concentrations, and meant to support survival of cells in synthetic conditions; and (3) coculturing is possible although establishing the spatial complexity and localization of cells as observed in tissue cross-sectioning is impossible in conventional 2D systems. Additionally, although cellular metabolism can be measured by instrumentation such as the Seahorse XF Analyzer, there is still a marked lack of chemical, cellular and metabolic heterogeneity<sup>18,19</sup> rendering these 2D systems poor in translation.

3D culture systems have the potential to bridge the gap, so to speak, between the 2D and preclinical *in vivo* model systems. The state of the art in 3D cell culture is the multicellular tumor spheroid (MTS) model, which is defined by aggregations of cells that grow in a spherical manner. Although this model system has been used for nearly 40 years and encompasses key features such as the development of biochemical gradients and the evolution of cellular phenotypes in response, the major drawbacks are (1) the lack of uniformity in formation methods; (2) difficult and destructive measurement of chemical and metabolic gradients; and (3) the lack of co-culture models especially due to cells resisting formation into

spheroids.<sup>14-16,20,21</sup> Other alternatives, such as 3D packed bed bioreactors like the bioartificial liver system, focus on instrumentation that avoids large-scale gradients, instead striving to create uniform extracellular conditions for bioproduction applications.<sup>22,23</sup> A final important point is that the power of multiparameter mathematical models to quantitatively predict parameters related to tumor development and therapy response (proliferation, metabolism, viability, drug transport) are limited by a pronounced lack of experimental data.<sup>13,14,24</sup> Implementing systems that have the ability to measure parameters and establish realistic initial conditions will greatly improve the use of these in silico models.

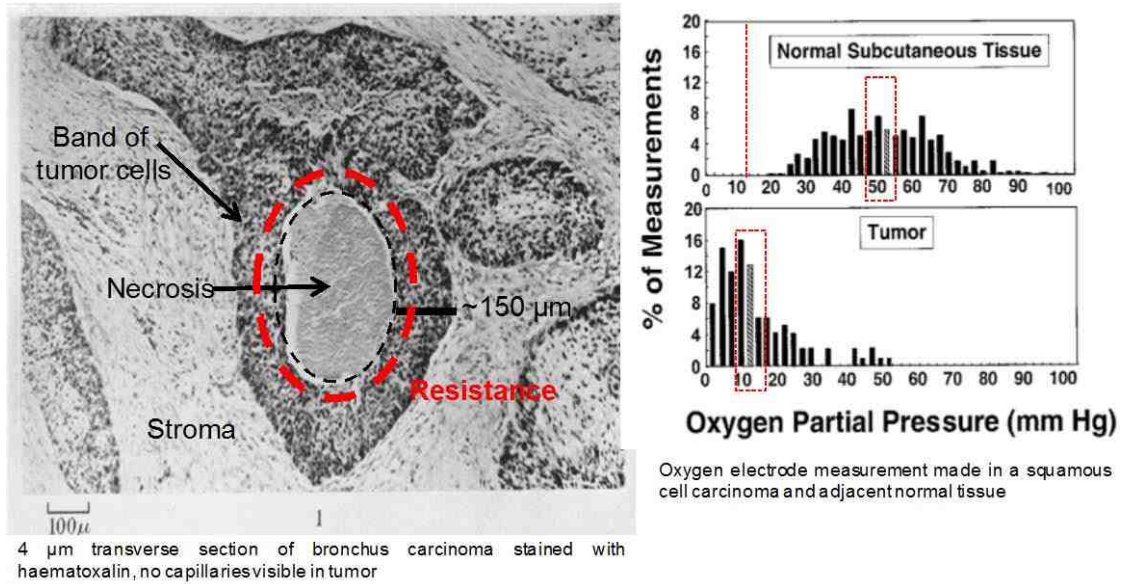
## 1.4 Hypoxia in the tumor microenvironment

*Avascular tumors develop oxygen and morphological gradients that apply selective pressures favoring adaptive and resistant cells during treatment.*

Cellular heterogeneity in the TME as well as resistance to therapeutic routines is accentuated by hypoxic conditions. The term *hypoxia* has been used imprecisely because of the marked increase in investigation of the condition by a large range of disciplines. By definition, tissue hypoxia results from inadequate supply of oxygen for homeostatic function. Biochemists extend the definition to include oxygen limited electron transport especially in the mitochondria<sup>25</sup> whereas physiologists extend the definition to encompass critical thresholds that results in the function of organs, tissues, and cells being eliminated when breached.<sup>26</sup> The inadequate supply of oxygen is caused by factors such as (1) low oxygen partial pressure in arterial blood due to heart disease or high altitude; (2) anemia or the reduced ability of blood to carry oxygen to tissues, including in the case of carbon monoxide poisoning; (3) reduced tissue perfusion; and (4) increased oxygen diffusion distance due to inconsistent blood flow in microvessel structure. In solid tumors, hypoxia is established because of structural abnormalities in tumor microvessels, disturbed microcirculation and therefore diminished oxygen diffusion geometry.<sup>27</sup> This is precisely the type of environmental selection pressure that causes adaptive cellular survival mechanisms to develop, demonstrating that even

in the simplest of cases a multidisciplinary approach is needed to fully understand the implications of cancer and treatment efficacy.

Hypoxia is recognized to render solid tumors more resistant to radiation therapy and recently has been thought to affect the malignant potential of a tumor.<sup>18,28,29</sup> These progressive phenotypes can mitigate the negative impact that oxygen deprivation would otherwise have and enable the preservation of genomic stability as well as the capacity to proliferate upon reoxygenation of the tissue in question. Because of this, tumor hypoxia is typically considered a negative clinical feature of solid tumors. Niches of hypoxia exposed cells are characteristically problematic because ionizing radiation and chemotherapeutic drug approaches target and selectively kill only proliferative cells in normoxic regions.<sup>30</sup> Ionizing radiation produces a DNA-radical that, in the presence of oxygen produces a covalent bond that fixes the damage and leads to cell death. In the absence of oxygen, regular DNA damage repair mechanisms mend the damage and the cell will not die, as in the quiescent zone of a tumor.<sup>31</sup> Conventional chemotherapeutic approaches are designed to target cells actively undergoing mitosis and thus only have an effect on the proliferative region of cells in a tumor, not to mention that the drugs themselves are also subject to high metabolic uptake as well as diffusional transport limitations. This creates a scenario where the nutrient depletion that once prevailed in the quiescent zone is reversed, metabolism becomes aerobic, cells switch to proliferation, and the daughter generation has a high likelihood of being



**Figure 1.4 Hypoxic Tissue.** Tissue sectioning and results from polarographic electrode measurements adapted from Gray et al. and Terris et al.<sup>32,33</sup> The tissue section shows the context in which an avascular tumor mass expands and the resulting phenotypic variation: surrounding stromal regions, proliferative band of tumor cells, quiescent region which gives rise to a radioresistant population of cells, and centralized necrosis. By comparing the histograms from normal vs tumor tissues, it becomes apparent that the oxygen tensions are remarkably distinct, and this supports the original thinking posed by Gray et al. (Images modified from source <sup>32,33</sup>)

phenotypically adapted to survive in increasingly aggressive environmental conditions, driving malignancy.<sup>29</sup>

This heterogeneous pathology was first observed by Thomlinson and Gray<sup>32</sup> in a series of pioneering studies that included tissue sectioning and staining by hematoxylin in the 1950's (Figure 1.4). Tissue cross-sectioning shows that vascular stroma is in contact with either normal or neoplastic epithelium, but capillaries do not penetrate the tissue and so the delivery of nutrients is strictly through diffusion of the tissue. In larger tumors the distance between blood vessels and necrosis is a constant distance ( $>150 \mu\text{m}$ ) and predicted to be the  $\text{O}_2$  diffusion distance (given  $\text{ppO}_2$  and oxygen consumption of cells). Gray et al predicted that viable hypoxic and radioresistant cells would be adjacent to the necrotic regions of tumors. These qualitative results were quantitatively verified with polarographic oxygen electrode experiments from 37 patients.<sup>33</sup> A mounted electrode the size of a needle was automatically advanced through either a normal or tumorigenic tissue and recordings were taken within 1.4s to avoid changes in oxygen tension resulting from pressure artifacts and tissue damage by the electrode itself. Although the discrete location of the electrode was unknown, a resulting histogram of oxygen tensions from multiple points within the tissue is still produced. In oxygenated tissue, the oxygen tensions follow a Gaussian distribution with no values less than 10 mmHg. It is worth noting that the distribution of the oxygenated tissue spans a wide range due to transient oxygen supply from the vasculature as well as changes in metabolic consumption rates as a function of position within the tissue, which as mentioned is not recorded with the electrode technique. In the tumor tissue

measurements, the median of roughly half the tumors have a value less than 10 mmHg. This value correlates to the point at which radiation resistance starts to develop, with full resistance at values less than 0.5 mmHg. In essence, the development of hypoxic conditions directly leads to clonal selection of cells that have accumulated adaptive advantages to survive harsh environmental conditions.



## 1.5 Oxygen and the Hypoxia Inducible Factor Pathway

*HIF-1 $\alpha$  is an oxygen-responsive transcription factor that enables cellular adaptation to hypoxic conditions by modulating expression of proteins.*

At the cellular level, hypoxia-inducible transcription factor 1 (HIF-1) is a classical pathway that enables cells to adapt to harsh environmental conditions by directly upregulating proteins that enhance the ability to survive in poorly oxygenated states.<sup>28</sup> Molecularly speaking, HIF-1 is a well understood, dichotomous pathway in terms of oxygen rich vs depleted levels in the extracellular biochemical microenvironment.<sup>34</sup> HIF-1 is a heterodimer that consists of: (1) HIF-1 $\alpha$ , the hypoxia response factor and (2) the constitutively expressed aryl hydrocarbon receptor nuclear translocator (ARNT, also known as HIF-1 $\beta$ ). In the presence of oxygen, prolyl hydroxylase domain proteins (PHD) covalently modify HIF-1 $\alpha$  by hydroxylation of proline residues 402 and 564.<sup>35</sup> This form of HIF-1 $\alpha$  interacts with the tumor suppressor Von Hippel-Lindau (VHL) protein (with binding further stabilized by acetylation of lysine residue 532 by acetyltransferase ARD1), causing HIF-1 $\alpha$  to become ubiquitylated by an E3 ubiquitin-protein ligase. Ubiquitylation targets HIF-1 $\alpha$  to the 26S proteasome where it is degraded (Top of Figure 1.5).<sup>36,37</sup> In the absence of oxygen, the rate of hydroxylation and acetylation on HIF-1 $\alpha$  decreases, VHL cannot bind, and the degradation rate of HIF-1 $\alpha$  similarly slows. The coactivators, p300 and CBP bind to HIF-1 $\alpha$  in the absence of hydroxylation and the complex translocates to the nucleus where it subsequently

interacts with ARNT/HIF-1 $\beta$ . Finally, DNA polymerase II joins the complex bound to hypoxia-response elements (HREs) on DNA, activating the transcription of target genes (Bottom of Figure 1.5).<sup>38,39</sup> The sheer number of downstream genes that are transcriptionally activated by HIF-1 is remarkable and covers cellular regulation schemes including but not limited to cell proliferation, cell survival, apoptosis, cytoskeletal structure, cell adhesion, erythropoiesis, angiogenesis, vascular tone, transcriptional regulation, drug resistance, tumor acidosis, and metabolism (nucleotide, iron, glucose, ECM, energy, amino acid). The latter two, tumor acidosis and cancer metabolism, have recently been acknowledged to not only add complexity to the idea of survival of the fittest population of cells in the TME but can work in combination with hypoxia to enhance pro tumor effects.



## 1.6 pH and the Hypoxia Inducible Factor Pathway

*Tumor acidosis is a key regulator of tumor progression and metabolic reprogramming that hypothetically stabilizes cytoplasmic HIF-1 $\alpha$ .*

The current understanding of pH homeostasis and metabolism is based on studies using differentiated, nonproliferating cells which provides insight to baseline energetics. For example, in the presence of oxygen, cells metabolize glucose to carbon dioxide by redox reactions in the tricarboxylic acid cycle. This produces NADH which is the currency for oxidative phosphorylation in the mitochondrial membrane to fabricate a maximized amount of ATP, roughly 36 molecules with minimal lactic acid production. In contrast, large amounts of lactic acid are produced only in anaerobic, i.e. hypoxic, conditions when oxygen is unavailable for the oxidation of glycolytic pyruvate where it is instead shunted into lactic acid production and minimal ATP production (about 4 molecules) (Figure 1.6, left hand side).<sup>40</sup> Conventionally, tumor acidosis arises from proliferating cells metabolically undergoing glycolysis regardless of oxygen conditions and as a direct consequence the accumulation of extracellular lactic acid, a concept known as the Warburg effect (Figure 1.6, right hand side). Although this might seem energetically counterintuitive as it does not yield the maximal amount of ATP, it is important to point out that during active mitosis the energy demand of the cell is not only for ATP production but to also double the biomass within the cell for division.<sup>41</sup> With this in mind, for a cell to divide, the energetic fate of a glucose

molecule is not only for carbon catabolism for ATP production but to also supply biomass components for nucleotides, amino acids, and lipids.<sup>42</sup> Nevertheless, this metabolic reprogramming changes both the intracellular and extracellular pH balance, potentially influencing the malignancy of a tumor. Although hypoxia is by far more studied, tumor acidosis has recently been identified as a major hallmark of tumors and a key regulator in tumor progression.<sup>43</sup>

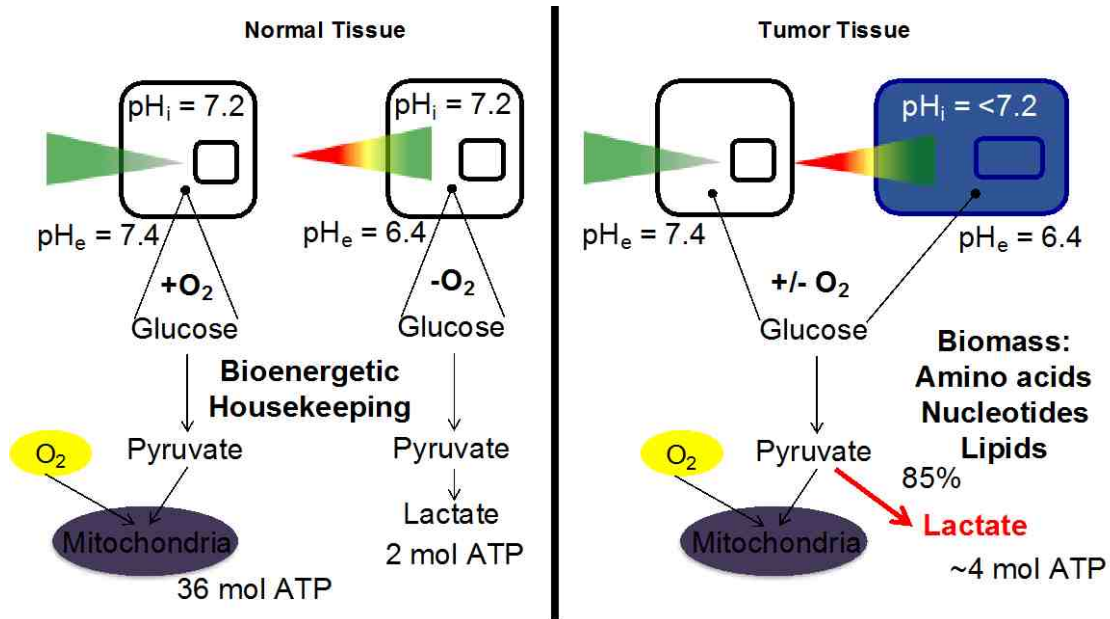
There has been speculation as to the order of operations in cancer pathophysiology as it relates to hypoxia, acidosis and metabolism. That being said, it is not clear if specific relationships between hypoxia, tumor acidosis, and metabolic reprogramming are mutually exclusive or mutually beneficial to the survival of cancer cells. Acidification of the extracellular environment results from the accumulation of H<sup>+</sup> ions as well as lactate likely because of a shift in the intracellular/cytosolic compartments of tumor cells from neutral to acidified.<sup>44,45,46</sup> In the event that intracellular pH is acidic, the efficiency of enzymes changes as some amino acid residues within proteins may become ionized leading to functional alterations, metabolic shifts, and potential triggering of cell death.<sup>47</sup> This effect is a selection pressure that potentially gives rise to phenotypic adaptations which contribute to maintenance of pH in an optimal range.

More globally speaking, chemical and metabolic gradients are established because of uncontrolled cellular proliferation in a tumor mass and therefore extended diffusional mass transfer distances from vasculature, leading to large-scale regions of combined hypoxia and acidosis.<sup>48</sup> Cells with more aggressive phenotypes, as mediated by cytoplasmic stabilization of HIF-1 $\alpha$  in *hypoxia*, are

thought to be resistant to both radiation and chemotherapies, thus driving malignant progression.<sup>49</sup> However, chemoresistance is not characteristic of all hypoxia-exposed cells and the role that extracellular *acidosis* plays in combination with normoxia remains unclear. HIF-1 $\alpha$  activity is implicated in therapy resistance due to pro-tumor effects, although some changes observed in hypoxic cells can result in increased drug sensitivity. Interventions that aim to target cancer by pH disruption require an improved understanding of how altered microenvironmental conditions influence adaptive phenotypes.<sup>50</sup>

In 2D cell culture models, cancer cells have been shown to survive stressed microenvironments by selecting phenotypes that enhance survival including suppressing apoptosis, initiating angiogenesis, and enabling a switch in energy metabolism.<sup>45</sup> However, it is unclear how the microregional distribution of HIF-1 $\alpha$  is modulated by coupled or uncoupled gradients in hypoxia and acidosis because these 2D cell culture models lack the spatial complexity of a 3D model system.<sup>51</sup> HIF-1 $\alpha$  controls the hypoxia induced, adaptive metabolic switch from oxidative phosphorylation to glycolysis, which results in the accumulation of lactic acid. It was once thought that acidosis was only toxic to cells, but it is now clinically recognized that mild acidosis (pH 6.5 and above) is protective and possibly acts as an input to other metabolic pathways.<sup>52</sup> Additionally, lactic acid can indirectly stabilize HIF-1 $\alpha$  and is thought to perpetuate the activation of HIF-1 $\alpha$  independent of hypoxia, but the mechanism has yet to be determined. An increase in the activity of HIF-1 $\alpha$  and subsequent metabolic programs alters the generation of pH and oxygen gradients by cancer cells and directly influences survival.<sup>53</sup> Therefore,

more aggressive cancer cell phenotypes evolve in order to survive stressed microenvironments. We hypothesize that there are combined low pH and high oxygen conditions that enhance HIF-1 $\alpha$  mediated metabolic adaptations, thereby promoting cell survival. This hypothesis is an exemplary case that demonstrates the need for improved technology in order to mechanistically investigate the complex interacting parameters of acidic, hypoxic, and nutrient deprived environments on tumor cell proliferation, survival and metabolism.



**Figure 1.6 Tumor Metabolism.** Diagrammatic representation of the metabolic and pH conditions in normal (left) and tumorigenic (right) tissues. Cells under homeostatic regulatory mechanisms in the presence of oxygen use oxidative phosphorylation as the main energetic pathway in order to maximize ATP production. In the absence of oxygen, cells with intact regulatory conditions undergo the conversion of pyruvate to lactate which in turn acidifies the extracellular environment. Under dysregulated energy control mechanisms cells have been demonstrated to switch metabolic programming regardless of the presence of oxygen in order to meet the energy demands for biomass production, as in highly proliferative cells in a tumor.



## 1.7 Conclusion and Outline of Subsequent Chapters

In summary, this dissertation establishes three distinct droplet-based 3D cell culture techniques that each contributes to the field of droplet generation and develops these technologies for the biological applications of cell encapsulation, 3D proliferation assays, culture of biomaterial supported spheroids, and growth of encapsulated cells in altered biochemical microenvironments. In addition to a review of the cancer research model paradigm and a description of the deficiencies in existing technologies, a classic biomedical research hypothesis is posed to demonstrate the need for improved 3D culture systems when investigating combinatorial parameters.

The remainder of this hybrid dissertation will progress as follows. Because this work is highly multi-disciplinary and cooperative, **Chapter 2** summarizes the specific contributions from collaborators including Professors, fellow graduate students, and undergraduate mentees to make sure due credit is received. **Chapter 3** describes the development of high-throughput droplet generation in air with acoustic modulation and introduces the biomaterial cell encapsulation solutions that are common to all remaining chapters in the work. **Chapter 4** details the controlled generation of monodispersed cell-encapsulating droplets in water-in-water emulsions using a lower throughput microfluidics platform and speaker derived acoustics. **Chapter 5** focuses on centrifugal droplet generation and highlights this as the preferred platform to produce monodispersed and spherical droplets with a medium to high throughput for all relevant biological applications. **Chapter 6**, although sometimes in the context of work in progress, establishes the

development of proliferation tracking assays using both qualitative and quantitative growth curve measurements in 2D vs 3D mono- and co-cultures, the instant formation and culture of biomaterial supported spheroids, and the design considerations for implementation of 3D culture systems that alter and control the biochemical microenvironment for hypoxia and acidosis investigations. **Chapter 7** provides high-level conclusions and discussion for the entirety of the dissertation. Each chapter has its own List of References included as the last section.

## 1.8 List of References

- (1) Maman, S.; Witz, I. P. A History of Exploring Cancer in Context. *Nat Rev Cancer* **2018**, 1–18.
- (2) Riemann, A.; Reime, S.; Thews, O. Tumor Acidosis and Hypoxia Differently Modulate the Inflammatory Program: Measurements in Vitro and in Vivo. *Neoplasia* **2017**, 19 (12), 1033–1042.
- (3) DelNero, P.; Lane, M.; Verbridge, S. S.; Kwee, B.; Kermani, P.; Hempstead, B.; Stroock, A.; Fischbach, C. 3D Culture Broadly Regulates Tumor Cell Hypoxia Response and Angiogenesis via Pro-Inflammatory Pathways. *Biomaterials* **2015**, 55, 110–118.
- (4) Global Burden of Disease Cancer Collaboration; Fitzmaurice, C.; Allen, C.; Barber, R. M.; Barregard, L.; Bhutta, Z. A.; Brenner, H.; Dicker, D. J.; Chimed-Orchir, O.; Dandona, R.; Dandona, L.; Fleming, T.; Forouzanfar, M. H.; Hancock, J.; Hay, R. J.; Hunter-Merrill, R.; Huynh, C.; Hosgood, H. D.; Johnson, C. O.; Jonas, J. B.; Khubchandani, J.; Kumar, G. A.; Kutz, M.; Lan, Q.; Larson, H. J.; Liang, X.; Lim, S. S.; Lopez, A. D.; MacIntyre, M. F.; Marczak, L.; Marquez, N.; Mokdad, A. H.; Pinho, C.; Pourmalek, F.; Salomon, J. A.; Sanabria, J. R.; Sandar, L.; Sartorius, B.; Schwartz, S. M.; Shackelford, K. A.; Shibuya, K.; Stanaway, J.; Steiner, C.; Sun, J.; Takahashi, K.; Vollset, S. E.; Vos, T.; Wagner, J. A.; Wang, H.; Westerman, R.; Zeeb, H.; Zoeckler, L.; Abd-Allah, F.; Ahmed, M. B.; Alabed, S.; Alam, N. K.; Aldhahri, S. F.; Alem, G.; Alemayohu, M. A.; Ali, R.; Al-Raddadi, R.; Amare, A.; Amoako, Y.; Artaman, A.; Asayesh, H.;

Atnafu, N.; Awasthi, A.; Saleem, H. B.; Barac, A.; Bedi, N.; Bensenor, I.;  
Berhane, A.; Bernabé, E.; Betsu, B.; Binagwaho, A.; Boneya, D.;  
Campos-Nonato, I.; Castañeda-Orjuela, C.; Catalá-López, F.; Chiang, P.;  
Chibueze, C.; Chittheer, A.; Choi, J.-Y.; Cowie, B.; Damtew, S.; Neves,  
das, J.; Dey, S.; Dharmaratne, S.; Dhillon, P.; Ding, E.; Driscoll, T.;  
Ekwueme, D.; Endries, A. Y.; Farvid, M.; Farzadfar, F.; Fernandes, J.;  
Fischer, F.; G hiwot, T. T.; Gebru, A.; Gopalani, S.; Hailu, A.; Horino, M.;  
Horita, N.; Hussein, A.; Huybrechts, I.; Inoue, M.; Islami, F.; Jakovljevic,  
M.; James, S.; Javanbakht, M.; Jee, S. H.; Kasaeian, A.; Kedir, M. S.;  
Khader, Y. S.; Khang, Y.-H.; Kim, D.; Leigh, J.; Linn, S.; Lunevicius, R.;  
Razek, El, H. M. A.; Malekzadeh, R.; Malta, D. C.; Marcenes, W.; Markos,  
D.; Melaku, Y. A.; Meles, K. G.; Mendoza, W.; Mengiste, D. T.; Meretoja,  
T. J.; Miller, T. R.; Mohammad, K. A.; Mohammadi, A.; Mohammed, S.;  
Moradi-Lakeh, M.; Nagel, G.; Nand, D.; Le Nguyen, Q.; Nolte, S.; Ogbo,  
F. A.; Oladimeji, K. E.; Oren, E.; Pa, M.; Park, E.-K.; Pereira, D. M.;  
Plass, D.; Qorbani, M.; Radfar, A.; Rafay, A.; Rahman, M.; Rana, S. M.;  
Søreide, K.; Satpathy, M.; Sawhney, M.; Sepanlou, S. G.; Shaikh, M. A.;  
She, J.; Shiue, I.; Shore, H. R.; Shrim, M. G.; So, S.; Soneji, S.;  
Stathopoulou, V.; Stroumpoulis, K.; Sufiyan, M. B.; Sykes, B. L.; Tabarés-  
Seisdedos, R.; Tadese, F.; Tedla, B. A.; Tessema, G. A.; Thakur, J. S.;  
Tran, B. X.; Ukwaja, K. N.; Uzochukwu, B. S. C.; Vlassov, V. V.;  
Weiderpass, E.; Wubshet Terefe, M.; Yebyo, H. G.; Yimam, H. H.;  
Yonemoto, N.; Younis, M. Z.; Yu, C.; Zaidi, Z.; Zaki, M. E. S.; Zenebe, Z.

- M.; Murray, C. J. L.; Naghavi, M. Global, Regional, and National Cancer Incidence, Mortality, Years of Life Lost, Years Lived with Disability, and Disability-Adjusted Life-Years for 32 Cancer Groups, 1990 to 2015. *JAMA Oncol* **2017**, 3 (4), 524–525.
- (5) Ferlay, J.; Soerjomataram, I.; Ervik, M.; Dikshit, R.; Eser, S.; Mathers, C.; Rebelo, M.; Parkin, D. M.; Forman, D. Cancer Incidence and Mortality Worldwide: IARC CancerBase No. 11. Lyon, France.
- (6) Gillies, R. J.; Verduzco, D.; Gatenby, R. A. Evolutionary Dynamics of Carcinogenesis and Why Targeted Therapy Does Not Work. *Nat Rev Cancer* **2012**, 12 (7), 487–493.
- (7) Gerlinger, M.; Rowan, A. J.; Horswell, S.; Larkin, J.; Endesfelder, D.; Gronroos, E.; Martinez, P.; Matthews, N.; Stewart, A.; Tarpey, P.; Varela, I.; Phillimore, B.; Begum, S.; McDonald, N. Q.; Butler, A.; Jones, D.; Raine, K.; Latimer, C.; Santos, C. R.; Nohadani, M.; Eklund, A. C.; Spencer-Dene, B.; Clark, G.; Pickering, L.; Stamp, G.; Gore, M.; Szallasi, Z.; Downward, J.; Futreal, P. A.; Swanton, C. Intratumor Heterogeneity and Branched Evolution Revealed by Multiregion Sequencing. *N Engl J Med* **2012**, 366 (10), 883–892.
- (8) Gerlinger, M.; Swanton, C. How Darwinian Models Inform Therapeutic Failure Initiated by Clonal Heterogeneity in Cancer Medicine. *Br J Cancer* **2010**, 103 (8), 1139–1143.
- (9) Greaves, M.; Maley, C. C. Clonal Evolution in Cancer. *Nature* **2012**, 481 (7381), 306–313.

- (10) Gillies, R. J.; Gatenby, R. A. Metabolism and Its Sequelae in Cancer Evolution and Therapy. *The Cancer Journal* **2015**, *21* (2), 88–96.
- (11) De Sousa E Melo, F.; Vermeulen, L.; Fessler, E.; Medema, J. P. Cancer Heterogeneity—a Multifaceted View. *Nature Publishing Group* **2013**, *14* (8), 686–695.
- (12) Bertout, J.; Patel, S.; Simon, C. The Impact of O<sub>2</sub> Availability on Human Cancer. *Nat Rev Cancer* **2008**, *8* (12), 967–975.
- (13) Kiran, K. L.; Jayachandran, D.; Lakshminarayanan, S. Mathematical Modelling of Avascular Tumour Growth Based on Diffusion of Nutrients and Its Validation. *Can. J. Chem. Eng.* **2009**, *87* (5), 732–740.
- (14) Carmona-Fontaine, C.; Bucci, V.; Akkari, L.; Deforet, M.; Joyce, J. A.; Xavier, J. B. Emergence of Spatial Structure in the Tumor Microenvironment Due to the Warburg Effect. *Proceedings of the National Academy of Sciences* **2013**, *110* (48), 19402–19407.
- (15) Bracken, M. B. Why Animal Studies Are Often Poor Predictors of Human Reactions to Exposure. *J R Soc Med* **2009**, *102* (3), 120–122.
- (16) McMillin, D. W.; Negri, J. M.; Mitsiades, C. S. The Role of Tumour–Stromal Interactions in Modifying Drug Response: Challenges and Opportunities. **2013**, 1–12.
- (17) Breslin, S.; O'Driscoll, L. The Relevance of Using 3D Cell Cultures, in Addition to 2D Monolayer Cultures, When Evaluating Breast Cancer Drug Sensitivity and Resistance. *Oncotarget* **2016**, *7* (29), 1–12.

- (18) Parks, S. K.; Mazure, N. M.; Counillon, L.; Pouysségur, J. Hypoxia Promotes Tumor Cell Survival in Acidic Conditions by Preserving ATP Levels. *J. Cell. Physiol.* **2013**, *228* (9), 1854–1862.
- (19) Estrella, V.; Chen, T.; Lloyd, M.; Wojtkowiak, J.; Cornell, H. H.; Ibrahim-Hashim, A.; Bailey, K.; Balagurunathan, Y.; Rothberg, J. M.; Sloane, B. F.; Johnson, J.; Gatenby, R. A.; Gillies, R. J. Acidity Generated by the Tumor Microenvironment Drives Local Invasion. *Cancer Research* **2013**, *73* (5), 1524–1535.
- (20) Alessandri, K.; Sarangi, B. R.; Gurchenkov, V. V.; Sinha, B.; Kiessling, T. R.; Fetler, L.; Rico, F.; Scheuring, S.; Lamaze, C.; Simon, A.; Geraldo, S.; Vignjevic, D.; Domejean, H.; Rolland, L.; Funfak, A.; Bibette, J.; Bremond, N.; Nassoy, P. Cellular Capsules as a Tool for Multicellular Spheroid Production and for Investigating the Mechanics of Tumor Progression in Vitro. *Proceedings of the National Academy of Sciences* **2013**, *110* (37), 14843–14848.
- (21) Jiang, Y.; Pjesivac-Grbovic, J.; Cantrell, C.; Freyer, J. P. A Multiscale Model for Avascular Tumor Growth. *Biophysical Journal* **2005**, *89* (6), 3884–3894.
- (22) Kang, C.-W.; Wang, Y.; Tania, M.; Zhou, H.; Gao, Y.; Ba, T.; Tan, G.-D. S.; Kim, S.; Leo, H. L. Computational Fluid Modeling and Performance Analysis of a Bidirectional Rotating Perfusion Culture System. *Biotechnol Progress* **2013**, *29* (4), 1002–1012.

- (23) Markov, D. A.; Lu, J. Q.; Samson, P. C.; Wikswo, J. P.; McCawley, L. J. Thick-Tissue Bioreactor as a Platform for Long-Term Organotypic Culture and Drug Delivery. *Lab Chip* **2012**, *12* (21), 4560–4569.
- (24) Roose, T.; Chapman, S. J.; Maini, P. K. Mathematical Models of Avascular Tumor Growth. *SIAM Rev.* **2007**, *49* (2), 179–208.
- (25) Boyer, P. D.; Chance, B.; Ernster, L.; Mitchell, P.; Racker, E.; Slater, E. C. Oxidative Phosphorylation and Photophosphorylation. *Ann. Rev. Biochem.* **1977**, *46*, 955–1026.
- (26) Peter Vaupel, F. K.; Okunieff, P. Blood Flow, Oxygen and Nutrient Supply, and Metabolic Microenvironment of Human Tumors: a Review. *Cancer Research* **1989**, *49*, 6449–6465.
- (27) Michael Hockel, P. V. Tumor Hypoxia: Definitions and Current Clinical, Biologic, and Molecular Aspects. *Journal of the National Cancer Institute* **2001**, 1–11.
- (28) Harris, A. L. Hypoxia — a Key Regulatory Factor in Tumour Growth. *Nat Rev Cancer* **2002**, *2* (1), 38–47.
- (29) Vaupel, P.; Mayer, A. Hypoxia in Cancer: Significance and Impact on Clinical Outcome. *Cancer Metastasis Rev* **2007**, *26* (2), 225–239.
- (30) Riffle, S.; Hegde, R. S. Modeling Tumor Cell Adaptations to Hypoxia in Multicellular Tumor Spheroids. **2017**, 1–10.
- (31) Brown, J. M. The Hypoxic Cell: a Target for Selective Cancer Therapy. *Cancer Research* **1999**, 1–9.



- (32) Gray, L. H.; Thomlinson, R. H. Histological Structure of Some Human Lung Cancers and the Possible Implications for Radiotherapy. *Br J Cancer* **1955**, *4*, 1–13.
- (33) Adam, M. F.; Gabalski, E. C.; Bloch, D. A.; Oehlert, J. W.; Brown, J. M.; Elsaid, A. A.; Pinto, H. A.; Terris, D. J. Tissue Oxygen Distribution in Head and Neck Cancer Patients. *Head Neck* **1999**, *21* (2), 146–153.
- (34) Majmundar, A. J.; Wong, W. J.; Simon, M. C. Hypoxia-Inducible Factors and the Response to Hypoxic Stress. *Molecular Cell* **2010**, *40* (2), 294–309.
- (35) Fong, G.-H.; Takeda, K. Role and Regulation of Prolyl Hydroxylase Domain Proteins. *Cell Death and Differentiation* **2008**, 1–7.
- (36) Cockman, M. E.; Masson, N.; Mole, D. R.; Jaakkola, P.; Chang, G.-W.; Clifford, S. C.; Maher, E. R.; Pugh, C. W.; Ratcliffe, P. J.; Maxwell, P. H. Hypoxia Inducible Factor- $\alpha$  Binding and Ubiquitylation by the Von Hippel-Lindau Tumor Suppressor Protein. *J. Biol. Chem.* **2000**, *275* (33), 25733–25741.
- (37) Masson, N.; William, C.; Maxwell, P. H.; Pugh, C. W.; Ratcliffe, P. J. Independent Function of Two Destruction Domains in Hypoxia-Inducible Factor- $\alpha$  Chains Activated by Prolyl Hydroxylation. *EMBO Journal* **2013**, 1–10.
- (38) Semenza, G. L. Targeting HIF-1 for Cancer Therapy. *Nat Rev Cancer* **2003**, *3* (10), 721–732.

- (39) Yamashita, K.; Discher, D. J.; Hu, J.; Bishopric, N. H.; Webster, K. A. Molecular Regulation of the Endothelin-1 Gene by Hypoxia. *J. Biol. Chem.* **2001**, *276* (16), 12645–12653.
- (40) Vander Heiden, M. G.; Cantley, L. C.; Thompson, C. B. Understanding the Warburg Effect: the Metabolic Requirements of Cell Proliferation. *Science* **2009**, *324* (5930), 1029–1033.
- (41) Lunt, S. Y.; Vander Heiden, M. G. Aerobic Glycolysis: Meeting the Metabolic Requirements of Cell Proliferation. *Annu. Rev. Cell Dev. Biol.* **2011**, *27* (1), 441–464.
- (42) Hatzivassiliou, G.; Zhao, F.; Bauer, D. E.; Andreadis, C.; Shaw, A. N.; Dhanak, D.; Hingorani, S. R.; Tuveson, D. A.; Thompson, C. B. ATP Citrate Lyase Inhibition Can Suppress Tumor Cell Growth. *Cancer Cell* **2005**, *8* (4), 311–321.
- (43) Corbet, C.; Feron, O. Tumour Acidosis: From the Passenger to the Driver's Seat. *Nat Rev Cancer* **2017**, *17* (10), 577–593.
- (44) Corbet, C.; Pinto, A.; Martherus, R.; de Jesus, J. P. S.; Polet, F.; Feron, O. Acidosis Drives the Reprogramming of Fatty Acid Metabolism in Cancer Cells Through Changes in Mitochondrial and Histone Acetylation. *Cell Metabolism* **2016**, *24* (2), 311–323.
- (45) Khacho, M.; Tarabay, M.; Patten, D.; Khacho, P.; MacLaurin, J. G.; Guadagno, J.; Bergeron, R.; Cregan, S. P.; Harper, M.-E.; Park, D. S.; Slack, R. S. Acidosis Overrides Oxygen Deprivation to Maintain

- Mitochondrial Function and Cell Survival. *Nature Communications* **1AD**, 5, 1–15.
- (46) Andreucci, E.; Peppicelli, S.; Carta, F.; Brisotto, G.; Biscontin, E.; Ruzzolini, J.; Bianchini, F.; Biagioni, A.; Supuran, C. T.; Calorini, L. Carbonic Anhydrase IX Inhibition Affects Viability of Cancer Cells Adapted to Extracellular Acidosis. **2017**, 1–13.
- (47) Srivastava, J.; Barber, D. L.; Jacobson, M. P. Intracellular pH Sensors: Design Principles and Functional Significance. *Physiology* **2007**, 22 (1), 30–39.
- (48) Vaupel, P.; Frinak, S.; Bicher, H. I. Heterogeneous Oxygen Partial Pressure and pH Distribution in C3H Mouse Mammary Adenocarcinoma. *Cancer Research* **1981**, 5, 2008–2013.
- (49) Jain, R. K.; Helmlinger, G.; Yuan, F.; Dellian, M. Interstitial pH and pO<sub>2</sub> Gradients in Solid Tumors in Vivo High-Resolution Measurements Reveal a Lack of Correlation. *Nature Medicine* **2004**, No. 3, 177–182.
- (50) Neri, D.; Supuran, C. T. Interfering with pH Regulation in Tumours as a Therapeutic Strategy. **2011**, 1–11.
- (51) Strese, S.; Fryknas, M.; Larsson, R.; Gullbo, J. Effects of Hypoxia on Human Cancer Cell Line Chemosensitivity. *BMC Cancer* **2013**, 13 (1), 1–11.
- (52) Hirschhaeuser, F.; Sattler, U. G. A.; Mueller-Klieser, W. Lactate: a Metabolic Key Player in Cancer. *Cancer Research* **2011**, 71 (22), 6921–6925.

- (53) Kareva, I.; Hahnfeldt, P. The Emerging “Hallmarks” of Metabolic Reprogramming and Immune Evasion: Distinct or Linked? *Cancer Research* **2013**, *73* (9), 2737–2742.

## **Chapter 2**

### **Content and Contributions**

## 2.1 Content in Chapters 3-7 and Contributions Made

*A high-level overview of each subsequent chapter is provided along with a description of the contributions to the experimental designs, results and data analysis as well as conclusions.*

Chapter 3 presents the design, construction, and optimization of a droplet generating instrumentation platform that enables high-throughput droplet formation in air using acoustic actuation of a flow stream. The design and implementation of different device designs, fluorescence and freeze frame imaging in real-time, optimized device parameters, and two different droplet collection mechanisms is reported. The use of biocompatible chemistries is investigated and demonstrates a first attempt at the use of aqueous two-phase separation in high-throughput droplet generation by acoustic modulation in air.

The majority of the work was carried out by Jacqueline De Lora, working with the advisement of Professors James Freyer and Andrew Shreve. Her contributions included leading the effort on device design and construction, developing the chemistry and cell culture methods, designing and implementing the pneumatic flow system and optical imaging system, implementing electronic and acoustic approaches to assist droplet generation, characterizing the device performance over a range of flow rates and frequencies and implementing and assessing droplet capture methods. For portions of this work, she was assisted by undergraduate students Jason Velasquez and Emily Innis, both of whom she

mentored during their undergraduate research experience. She also acknowledges the assistance of graduate students Daniel Kalb and Travis Woods for help in the acoustic and electronic components of the work.

Chapter 4 presents a highly collaborative work that demonstrates the use of an integrated microfluidics/acoustics approach to encapsulate cells in an aqueous two-phase system. The acoustic break-up of an aqueous two-phase system into droplets in the microfluidics device is characterized using enriched polymer solutions that are designed for 3D cell culture applications, flow rate/frequency optimization matrices for monodisperse droplet generation, rheology and index of refraction measurements to characterize physical properties of the polymer solutions, and the influence of acoustic modulation on droplet diameter. Cell concentrations are investigated and optimized for producing cell encapsulating droplets that are demonstrated to proliferate in optimized suspension culture for 9 days. The use of an Annexin V/PI flow cytometric assay to assess the biocompatibility of the polymer solutions used for cell encapsulation is also reported. This droplet-based cell encapsulation approach validates the use of aqueous two-phase systems in microfluidics and for 3D cell culture applications in cancer research.

Jacqueline De Lora led the portions of this effort that involved development and adaptation of polymer solutions for cell culture applications, development and implementation of the protocols for cell encapsulation and suspension culture, all cell assays such as cell counting and flow cytometry measurements, working under the advisement of faculty members Andrew Shreve and Nick Carroll. She

also worked closely with graduate student Frank Fencel, and assisted his efforts to develop and implement the microfluidic device design, and worked closely with both Frank Fencel and undergraduate student Aidira Dora Yajaira Macias Gonzales, who led the work characterizing the aqueous two-phase separation properties. In addition, New Mexico State University graduate student Alireza Bandegi and Professor Reza Foudazi are acknowledged for their work in measuring rheology data of the polymer/cell solutions.

Chapter 5 describes the use of centrifugal force to synthesize cell encapsulating droplets with a moderate throughput and optimized control over droplet size as well as cell concentration in the droplets. This chapter demonstrates improvement of centrifuge tube assemblies with new hybrid nozzles, optimization of droplet generating regimes and control over droplet size in device operation, as well as applications that include the first instance of generation of super small droplets, and the encapsulation and measurement of low and high cell occupancy droplets. This chapter sets the stage for using this preferred method for all cancer biology applications discussed and in progress in Chapter 6.

Jacqueline De Lora carried out the majority of the work in Chapter 5 with the advisement of Professors James Freyer and Andrew Shreve. Her contributions include leading the design and construction of centrifuge tube assemblies with hybrid nozzles for both cell encapsulating droplet generation as well as cell-sized droplet generation. For portions of this work, she was assisted by undergraduate students Jason Velasquez (optimization and image analysis) and Cody Moezzi



(cell-sized droplet generation), both of whom she mentored during their undergraduate research experiences.

Chapter 6 begins the exploration of using cell encapsulated droplets, primarily generated using technology developed in Chapter 5, to establish more realistic 3D culture environments with standardized biological assays. The growth rate of two relevant cancer cell lines in 2D mono- and co-cultures are measured using cell counting growth curves and fluorescence membrane dye dilution flow cytometric assays. Then these assays are adapted to 3D culture using cell encapsulated droplets generated by centrifugal synthesis in proof-of-principle experiments, demonstrating feasibility. High cell occupancy droplets are generated and grown in suspension culture for 7 days to demonstrate the use of the platform as an improved approach for the generation of scaffold supported instant multicellular tumor spheroids. Finally, an experimental system for the 3D culture of low cell occupancy droplets in altered and combinatorial chemical environments is designed and constructed towards the end of establishing an improved method to investigate the biomedical question posed in Chapter 1.

Jacqueline De Lora is responsible the experimental designs and results obtained in Chapter 6 under the advisement of Professors James Freyer and Andrew Shreve. She performed the growth curves and fluorescence dilution curves in 2D and 3D, she designed and implemented the instant multicellular spheroid experiments, and she constructed the system for altered environment experimentation. Jacqueline is continuing to work towards taking the experiments for 3D growth curve and fluorescence dilution as well as altered environments past

the level of “proof-of-principle” for inclusion in publications in preparation. For portions of this work, she was assisted by undergraduate students Jason Velasquez and Emily Innis, as mentioned before.

Chapter 7 provides a discussion of the work accomplished in the dissertation and the future directions of the work.

## **Chapter 3**

### **High-throughput Acoustic Droplet Generation in Air**

### 3.1 Controlled Mass-Production of Droplets

*Development of new high-throughput droplet generating instrumentation and devices that enables use of highly viscous biomaterial polymers, high speed droplet formation by acoustic modulation, and two potential approaches to droplet solidification mechanisms is presented.*

2D cancer model systems are the standard laboratory approach for the investigation of mechanisms underlying the biology of cancer. More recently, motivated by the disparate results when comparing 2D cell culture to *in vivo* experiments, researchers have realized the need to use more complex and physiologically realistic 3D model systems that can closely mimic the tumor microenvironment (TME).<sup>1,2</sup> With the need to use more biomimetic 3D cell culture models comes the realization that new instrumentation is required to facilitate this shift in standard lab practices. In order to achieve more accurate representations of cancer tissues and greatly accelerate progress, especially as applied to high-throughput drug screening for personalized medicine<sup>3</sup>, many investigators have used existing model systems such as (1) multicellular tumors spheroids grown in suspension by conventional formation methods<sup>4</sup>; (2) microfluidic systems to generate and culture 3D cell containing scaffolds<sup>5</sup>; (3) gel embedding into extracellular matrix analogue materials<sup>6</sup>; or (4) cell bioprinting to make layer by layer 3D tissue constructs<sup>7</sup>. However, many of these technical approaches face technical challenges that make them unrealistic in terms of fully replacing 2D cell

culture as the standard lab practice. These challenges include the overall throughput of the system, which tends to be low in microfluidic systems; difficulty in flowing highly viscous biomaterial solutions through devices; generating small constructs of uniform composition and size; as well as the cost and time it takes to implement these new platforms into lab practices. Taking these challenges into consideration, it is clear that an approach combining knowledge from many technical fields is best suited for accomplishing the design, construction, and use of a system with the ability to generate large populations of uniform 3D cell scaffolds that can easily interface with existing high-throughput technologies.

With these factors in mind, the design of the in-air acoustic droplet generator is inspired by the field of flow cytometry (droplet-based cell sorting) to produce a robust droplet generating instrumentation platform that operates at high frequency (up to 25,000 droplets/second), can handle highly viscous biomaterial solutions through the integration of amplification electronics, has a narrow and small size distribution for droplets generated in the air (down to 100  $\mu\text{m}$  diameter drops), and uses devices and optical components constructed from inexpensive materials. The high-level goal of this new instrumentation platform (described in section 3.3) is to produce 100  $\mu\text{m}$  diameter calcium alginate droplets with encapsulated cells for 3D cell mono- and co-culture applications. A droplet diameter of 100  $\mu\text{m}$  is desirable to therefore prevent the generation of intra-droplet gradients (generally accepted to develop past  $\sim 150$   $\mu\text{m}$  radial distances<sup>8</sup> depending on cell occupation, the availability of nutrients, and cellular consumption rates).

Interestingly, one of the challenges of this method arises from its high-throughput nature. The flow conditions needed for stable droplet generation in the desired size range correspond to high linear flow velocities. In turn, this set of conditions leads to difficulties in capturing and cross-linking individual spherical droplets, and many design iterations have been explored in an attempt to generate and solidify stable droplets. There is still further optimization to be done for the cell encapsulation aspect of this work, but the results presented provide the first instance of high speed droplet generation using an instrumentation platform that would be as easy to implement into a laboratory as a flow cytometer.

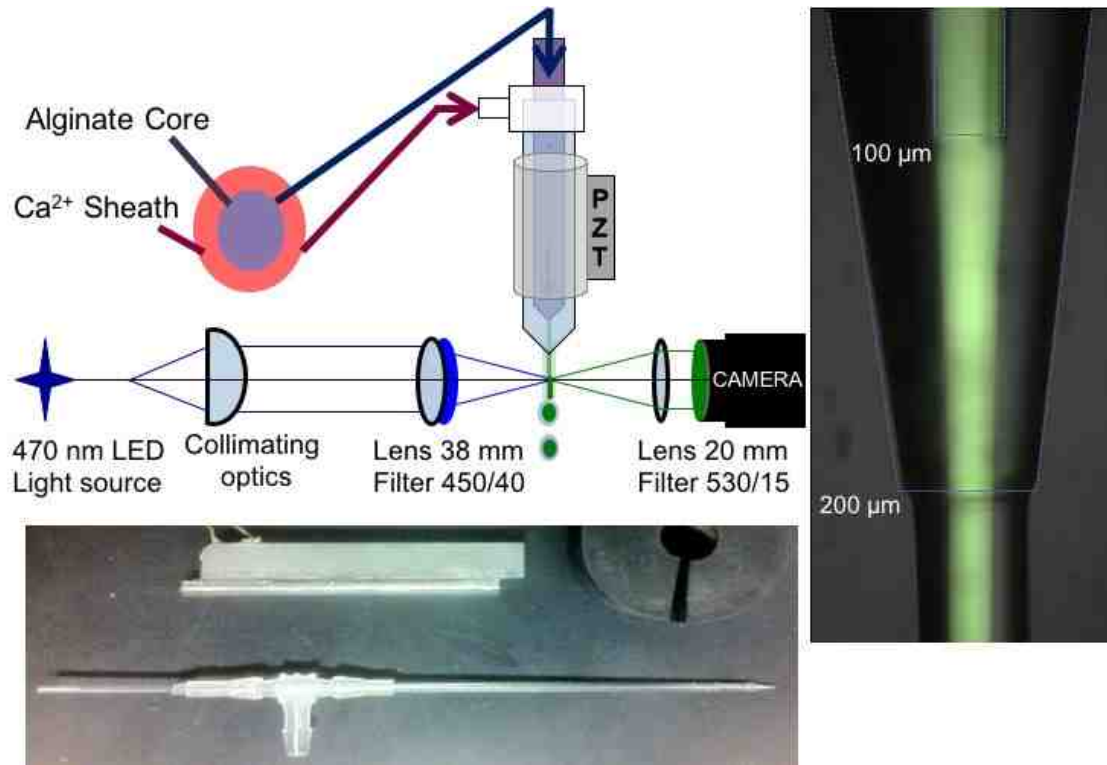
### 3.2 Device designs

*Glass capillary devices and piezoelectric transducers are interfaced to produce either dual or single channel droplet generating devices.*

Two device designs have been investigated for use in the high-throughput acoustic droplet generating instrumentation platform. The first devices are designed with a nesting core/annular fluidic profile to use the principle of hydrodynamic focusing to help control the size of the biomaterial droplet produced and possibly enable droplet crosslinking in air. The second devices are designed with a more simplified, single stream profile to enable the direct acoustic modulation of droplet formation in air. Dual channel devices are constructed using a simple tee-junction tubing connector (Cole Parmer 1/16" Nylon Tee Fitting) and slip-fit tubing (Cole Parmer Rubber tubing 2.4 mm O.D. 0.70 mm I.D.) serving as the anchoring point for the nesting of two capillaries. The capillaries are two different dimensions matched for housing one within the other (Borosilicate Glass from World Precisions Instruments, Outer Capillary 1.5 mm O.D. 1.12 mm I.D. and Inner Capillary 1.0 mm O.D. 0.58 mm I.D. both 155 mm long). They are pulled to a taper using a P-97 Flaming/Brown Micropipette Puller (Sutter Instrument Co.) and soldered or cut to a defined nozzle diameter using a MF-830 Microforge (Narishige Group), typically 100  $\mu\text{m}$  inner nozzle and 200  $\mu\text{m}$  outer nozzle diameter. To assemble the nesting dual channel device, the slip-fit flexible tubing junctions are placed onto the two long axis ports of the tee-junction connector.

Then the 11.2 cm long inner capillary is threaded through the long axis of the tee connector/slip-fitted tubing and secured closer to the blunt end capillary/tee connector arm, making sure to position it so that the inner capillary will not push through the outer nozzle once it is in place. The 7.2 cm short outer capillary is threaded over the inner capillary with the 100  $\mu\text{m}$  nozzle end and carefully pushed up into the slip-fit piece of tubing to attach it to the tee-junction as well. To connect the piezoelectric element in the dual channel device, a rectangular piezoelectric transducer (5 cm, Boston Piezo Optics) is super glued to a 5 cm long, 3.2 mm O.D. 1.7 mm I.D. stainless-steel tube (Valco). This method is preferable in comparison to direct attachment of the rectangular piezoelectric transducer to one side of the glass capillaries, as the unevenly distributed weight of the crystalline material in the latter case causes misalignment of the nesting nozzles. Finally, a small amount of ultrasound gel (LiquaSonic Ultrasound Gel) is applied to the length of the outer capillary of the dual channel device and the entire device is carefully threaded into the stainless-steel tubing/piezoelectric assembly, establishing an acoustic energy transducing interface between the glass capillaries and the piezoelectric transducer (Figure 3.1). Single channel devices are simple in their design and implementation. A capillary nozzle is fabricated as described above using the pulling and soldering method to any desired nozzle diameter (usually between 50-100  $\mu\text{m}$  diameter). The piezoelectric transducer is super glued directly onto the side of the glass capillary and fluidic lines are attached by slip fitting rubber tubing over the blunt end of the capillary. The device is mounted by clamping directly onto the glass capillary above the piezoelectric transducer.





**Figure 3.1 Dual Channel Device.** Diagram depicting the core-annular flow profile of a dual channel device with fluorescence light path in the instrument as well as the actual two channel device assembled with a tee junction and the piezoelectric transducer coupled to the stainless-steel mounting tube. On the right is an image of an operating dual channel device at the nozzle, with dye incorporated into the core flow stream. This image shows the nesting capillaries as well as hydrodynamically focused core/sheath fluid flow.

### 3.3 Instrumentation operation

*Fluidic, optical, and electronic design of the droplet generating instrumentation enables robust pressure driven fluid flow and device optimization through real-time imaging during operation.*

The droplet generating instrument is primarily built using materials obtained from ThorLabs optomechanic kits, including components such as an aluminum breadboard as the base, posts and post holders, optical mounts, lenses and filters, translation stages, and a self-centering mount to vertically secure the device in a suspended position (Figure 3.2). Specifically, post holders are arranged so that all optical components are held above the breadboard in an orientation such that the optical paths orthogonally intersect the vertical, downward flow stream of the device. The device and the camera mount can both be translated in x, y and z directions. For imaging droplet generation in real-time, the device is back-lit with a broad spectrum white LED strip (Super Bright LEDs) and homemade diffuser (simply a microscope slide with a strip of cloudy scotch tape mounted in front of the LED). The LED is synced to strobe at the same piezoelectric modulation frequency that governs the droplet formation rate by using a Tektronix AFG 3102 dual channel function generator (Figure 3.2 C and D). This technique produces a freeze frame effect to image the high-frequency droplet generation. A 25.4 mm diameter lens with a 25.4 mm focal length (Bi-Convex Uncoated Lens Model KBX046, Newport) is used to collect light from the region of the stream and image

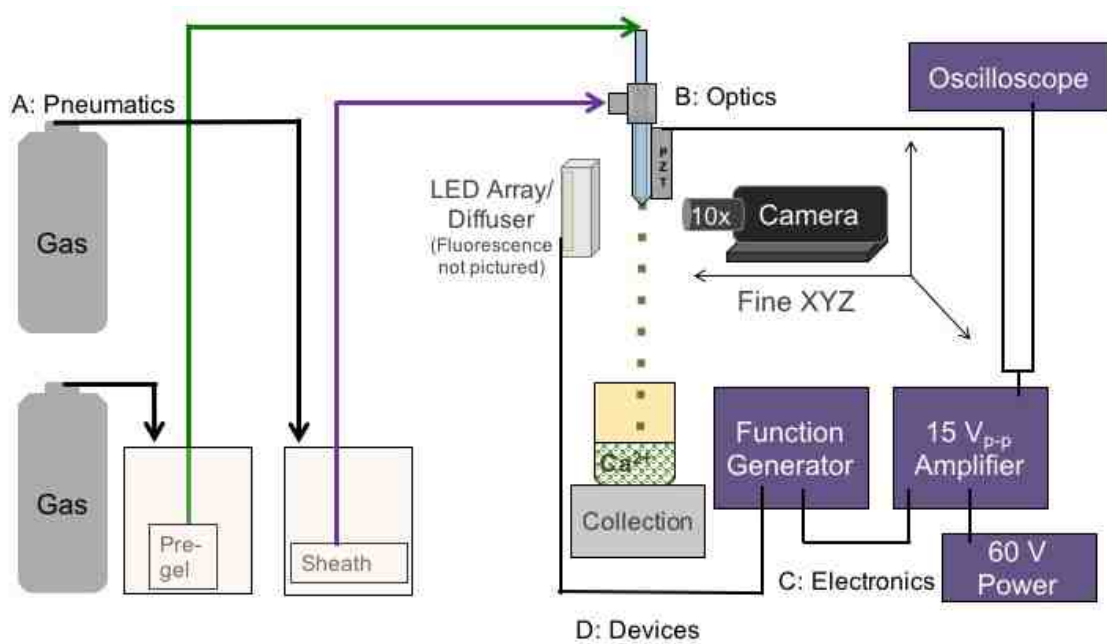
relay to create an image on a ThorLabs Compact USB 2.0 CMOS Camera (Figure 3.2 B). The capability to image fluorescence in addition to the backlit image is integrated into the optics by assembling a 25 mm diameter collimating aspheric lens with a 20.1 mm focal length (Asphere Lens Model ACL2520U-A, ThorLabs) and a 25.4 mm lens with a 38 mm focal length (Plano-Convex Lens Model KPX079, Newport) in sequence orthogonally to the white LED light path (Figure 3.1). Fluorescein is used as the fluorophore in dual channel device operations and as such, the excitation source used is a point source blue LED, which emanates diffuse light. This diffuse light is collected into a lens tube assembly containing the aspheric lens to broadly focus the light that then travels into the 25.4 mm,  $f = 38$  mm focusing lens with a 450/40 filter (here, 450/40 refers to a bandpass spectral filter of 40 nm full-width-at-half-maximum transmission, centered on 450 nm wavelength; similar notation is used throughout this section) to ultimately focus the blue light to a roughly 1 mm spot size, which intersects the flow stream. For fluorescence imaging, a 530/15 filter is placed in front of the CMOS camera. Additionally, an amplifier (Acoustic Cytometry System, Los Alamos NM, Model H7 PIN 103) with an external power supply (BK Precision DC Power Supply Model 1711) is integrated into the electronic set up to increase the strength of the acoustic driving field, and an oscilloscope (Tektronix TDS 2004B) is used to measure the resulting voltage and waveform as drawn in Figure 3.2 C.

Fluid flow into the device is produced using a pneumatics system rather than syringe pumps (Figure 3.2 A). This is an important distinction as it was discovered that the highly viscous nature of the biomaterial solutions used in this

work overcomes the power of the syringe pump driver arm, creating a back pressure and causing the fluid to be injected with oscillations rather than uniformly. Therefore, two gas cylinders of 5% CO<sub>2</sub> BAL AIR are connected to the in-ports of two stainless steel pressure tanks (reclaimed from a Becton Dickinson FACS instrument) using Tygon tubing and hose-barbed brass tubing adapters. The steel pressure tanks contain the fluids for supply to the inner and outer capillaries and are equipped with precise low pressure digital pressure gauges (Grainger Industrial Supplies). Details of the solution content are discussed in section 3.4, and the fluids inside each pressure tank are contained in glass beakers with a Silastic tubing line (Cole Parmer) submerged to the bottom of the beaker. This tubing line extends through the out-port of the pressure chamber and connects by slip fit to the blunt end of the inner capillary for the core flow injection or to the orthogonal hose barb on the tee connector of the device for the sheath injection. In the case of single channel device operations, only one pneumatic line is needed and the Silastic fluid flow tubing is slip fit directly onto the glass capillary (Figure 3.2 A).

Finally, this work investigates the necessary physical properties and feasibility of the collection and solidification of high-speed droplets. Two different droplet collection methods have been explored. Regardless of the mechanical droplet collection method used, it is integrated into the instrument and positioned underneath the device on the breadboard. The first collection method uses a stir plate (VWR Magnetic Stirrer Model C2) and beaker containing the droplet solidification solution with a stir bar to mix the solution as the droplets are collected.

The second collection method uses an Arrow 850 driver (Arrow Engineering Co. Inc.) connected to a bearing attached to a small aluminum breadboard with an O-ring. The bearing is used to rotate a cardboard platform that securely holds flasks of different diameters and heights containing the droplet solidification solution. This rigid body rotating design creates a non-turbulent mixing environment.

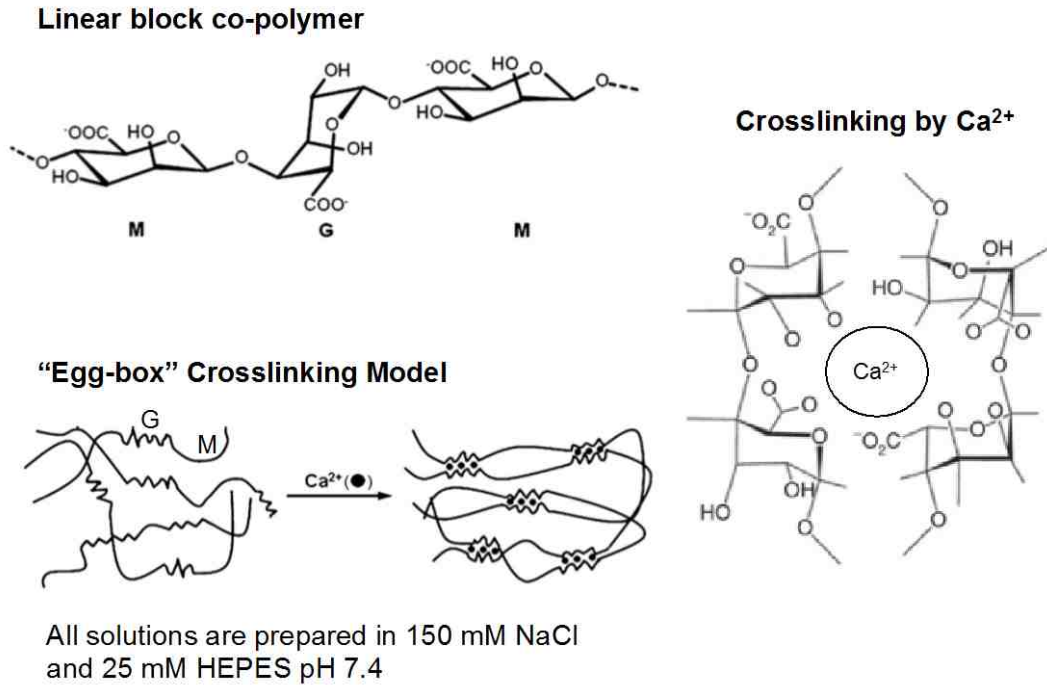


**Figure 3.2 Instrumentation Schematic.** Droplet generating device schematic depicting the integration of (A) pneumatics, (B) optics, and (C) electronics to produce an instrument that has fine control over the fluid dynamics in the device (D) with the capability to image in both brightfield and fluorescence modes. For detailed description of the construction and operation of the instrument, acoustics and devices (see Sections 3.2 and 3.3).

### 3.4 Biocompatible Droplet Generation

*The basic biomaterial approach using alginate is characterized and investigated in both dual and single channel droplet generation with collection by stir plate mixing/collection mechanism.*

Alginate is a linear block copolymer containing mixed blocks of (1,4)-linked  $\beta$ -D-mannuronate (M) and  $\alpha$ -L-guluronate (G) residues that is derived from brown seaweed and processed into powders of differing compositions. It is now very well understood how different block lengths, combinations of G/M, and the source of the alginate itself influences its physical properties such as molecular weight and viscosity. The G-blocks crosslink in the presence of divalent cations to form hydrogels with a porous structure that may be tuned depending on the composition of G:M (Figure 3.3).<sup>9</sup> In general, the alginate (ALG) powder is measured in weight percent by volume and dissolved in a physiological buffer of 25 mM HEPES and 150 mM NaCl (Sigma-Aldrich) overnight with vigorous stirring. Because of the highly viscous nature of all biomaterial solutions, a special pH electrode that can more accurately measure viscous and colloidal solutions (Orion™ Ross™ Sure-Flow™ pH Electrode with Sure-Flow Junction, Thermo-Fisher) is used to adjust the pH to 7.4. Sterilization of the solutions is also required for cell culturing. Sterilization by autoclave is not an option as the high heat changes the polymer structure and the ability to crosslink. The viscosity of ALG solutions higher than 1% w/v make it impossible to filter through the standard 0.2  $\mu$ m pore size for sterilization but it was



**Figure 3.3 Alginate Crosslinking.** Molecular structure of alginate (left top) and representation of the interaction between sterically available carboxylic acid groups of G-blocks solidifying the gel by the egg box model (left bottom) as well as a depiction of the intermolecular forces that cause crosslinking by the arrangement of carboxylic acid groups of the G-blocks around divalent cations, in this case calcium (right).<sup>9,10</sup>

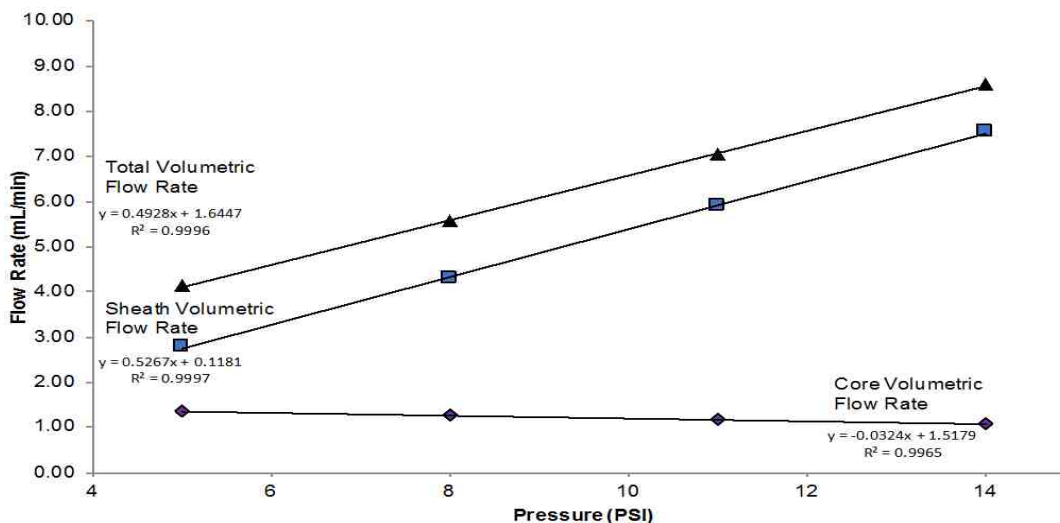


found that sterile filtering through a 0.45  $\mu\text{m}$  bottle top filter assembly (Nalgene, VWR) is possible under high vacuum.

Dual channel device operations were first completed using 2% ALG in the inner core flow with the sheath solution consisting of the physiological buffer without ALG. The solidification buffer was a separate 1M  $\text{CaCl}_2$  solution stirred in a beaker below the nozzles. The flow rates in the device are measured by pressurizing the core chamber to 5 PSI (for this example) and keeping it consistent through the characterization. The sheath flow rate is measured for a range of pressures from 5 to 14 PSI in the corresponding sheath fluid chamber. The individual flow rates for the sheath and core are measured in triplicate by first weighing the volume of each fluid before placing into the pressure chamber. The fluid chambers are pressurized to the desired PSI and the combined fluids are run through the device for a precise amount of time. The fluid flow is stopped and the weight of the fluids in the core and sheath chamber are re-weighed. The density of the core and sheath fluids are also necessary to determine the flow rate. The densities are measured in triplicate by zeroing an analytical balance with a weigh boat and a 1000  $\mu\text{m}$  pipette tip. Then 1 mL of the solution in question is pipetted up into the tip and the entire 1 mL of solution and tip is placed on to the weigh boat on the analytical balance and the weight in grams is recorded. These values are then used to determine the flow rate in mL/min (Figure 3.4 and Table 3.1). Additionally, the hydrodynamic focusing of the flow rate pairs is measured in triplicate by taking three fluorescent images of the nozzle interface within the device and using ImageJ to threshold the images and measure the thinning

diameter of the core flow stream. The focusing is calculated assuming the sheath O.D. is consistent with the 200  $\mu\text{m}$  diameter outer nozzle (Table 3.2 and Figure 3.5).

The droplet modulation frequency by the piezoelectric transducing crystal has been optimized over a range of frequency/flow rate combinations. For these experiments, the core fluid flow is held constant while the sheath flow is incrementally increased and the modulation frequency is scanned across a range to find stable droplet formation. It was observed that an increase in sheath flow rate typically requires a higher modulation frequency and will shift the droplet formation downstream. In the majority of frequency/flow rate combinations attempted, amplification of the signal up to 50 Vp-p is required to modulate the droplet formation (Figure 3.6). Finally, the solidification of core-annular droplets both in a collection bath and during transit in the air has been attempted. In most cases, collecting core-annular droplets directly into a 100 mM  $\text{CaCl}_2$  solidification bath did not produce solidified, spherical particles. Crosslinking of the droplets during transit in air was investigated by adding up to 38 mM of  $\text{CaCl}_2$  to the sheath solution in an attempt to create a crosslinked shell around the droplet and aid in particle stabilization. However, this experiment was not successful because of the spatial arrangement of the fluid flow within the nozzle. There is a short distance before exiting the nozzle where the alginate core and calcium sheath begin to gel and cause clogging. In the dual channel droplet generation, successful solidification of spherical alginate particles formed within sheathed droplets has yet to be demonstrated.

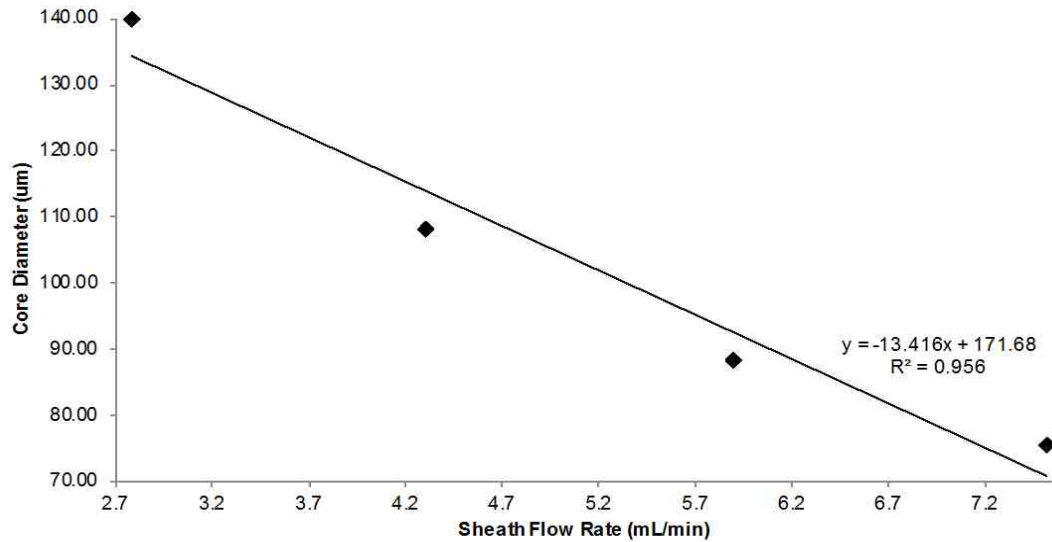


**Figure 3.4 Dual Channel Flow Rates.** Measured volumetric flow rates by increasing the sheath pressure and holding the core pressure constant. The negative slope observed in the core volumetric flow rate is consistent with the increased sheath volume being displaced over time and at higher pressures, indicating that hydrodynamic focusing in the device is achieved. Error bars are smaller than the points on the plot and standard deviations are reported Table 3.1

3.1

PSI	CORE (mL/min)			Sheath (mL/min)			Combined (mL/min)		
	Average	SD	CV	Average	SD	CV	Average	SD	CV
5	1.36	0.04	0.03	2.78	0.08	0.03	4.14	0.11	0.03
8	1.25	0.03	0.02	4.30	0.02	0.00	5.56	0.05	0.01
11	1.15	0.05	0.04	5.89	0.09	0.02	7.03	0.04	0.01
14	1.07	0.09	0.08	7.52	0.06	0.01	8.58	0.04	0.00

**Table 3.1 Table of flow rates.** Flow rates determined by measuring the total volumetric displacement of solutions over a range of pressures.

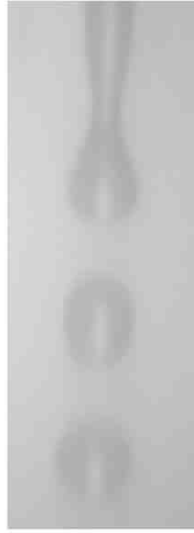


**Figure 3.5 Hydrodynamic Focusing.** Plot demonstrating that as the sheath flow rate is increased in the pressure-drive flow system, the diameter of the core stream decreases. This principle of hydrodynamic focusing is well described in the field of flow cytometry and can be used here to further influence the diameter of the droplets. Each measurement was recorded in triplicate and the standard deviation as well as CV are reported in Table 3.2.

PSI	Sheath Average Flow Rate (mL/min)	Core Average Diameter (um)	SD	CV
5	2.78	139.84	0.29	0.00
8	4.3	108.08	0.94	0.01
11	5.89	88.50	2.64	0.03
14	7.52	75.43	3.48	0.05

**Table 3.2 Hydrodynamic Focusing Table.** Measured sheath flow rates and the corresponding core diameter measured by ImageJ analysis.

8 psi core flow



8 psi sheath flow  
1.58 kHz  
0.5 cm breakoff



10 psi sheath flow  
1.98 kHz  
0.5 cm breakoff



12 psi sheath flow  
2.18 kHz  
0.7 cm breakoff



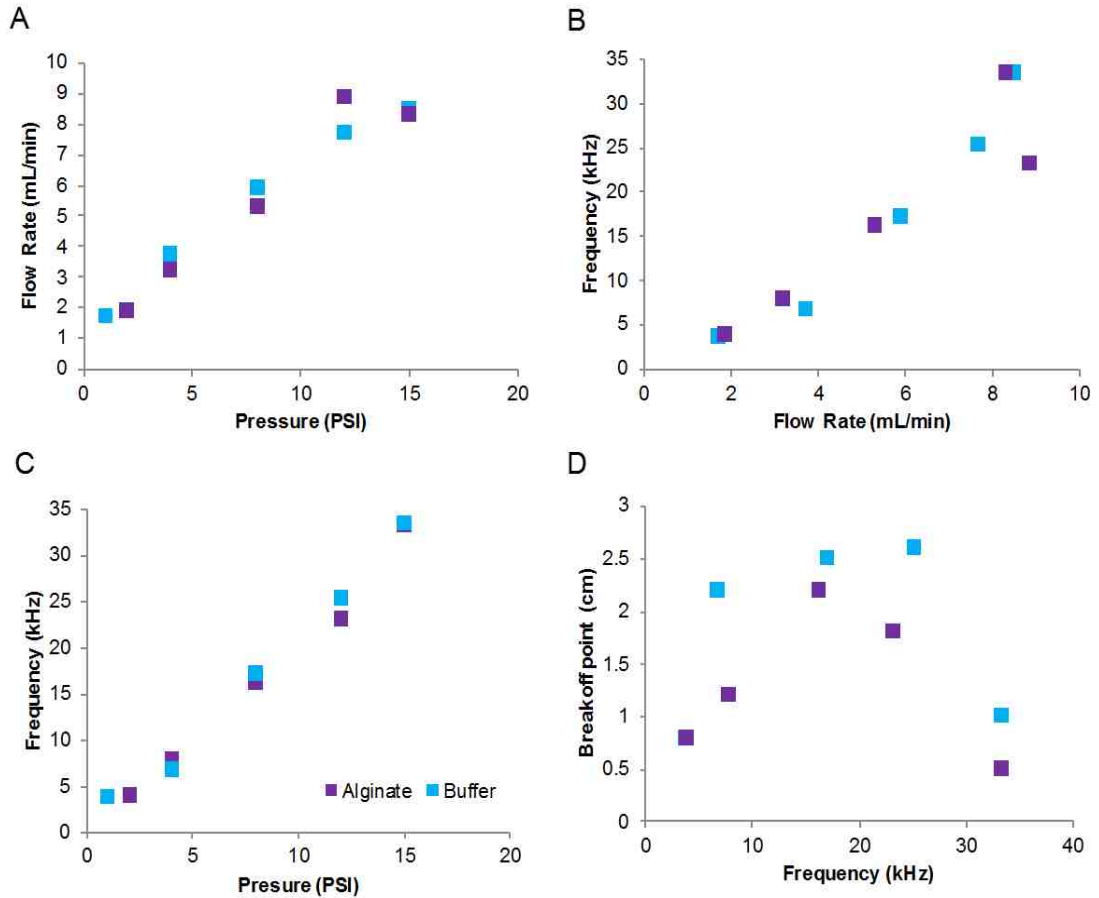
14 psi sheath flow  
2.28 kHz  
0.7 cm breakoff

**Figure 3.6 Dual Channel Droplets in Air.** Optimization of the dual channel device with a constant core flow rate and increasing sheath flow rates. The images of droplets transiting in the air are captured at the same location downstream of the nozzle. The piezoelectric modulation frequency increases with increasing sheath flow rate and at a certain threshold the droplet break off point is driven farther upstream/towards the nozzle.

A simpler method is used to measure the flow rate in single channel devices (100  $\mu\text{m}$  nozzle diameter). The flow rate of the alginate fluid is measured by weighing the amount of solution displaced over a given time. The measurements were done in triplicate and compared against buffer as a reference (Figure 3.7 A). The density of each solution is also measured in triplicate by zeroing an analytical balance with a weigh boat and a 1000  $\mu\text{m}$  pipette tip. Then 1 mL of the alginate is pipetted up into the tip and the entire 1 mL of solution and tip is placed on to the weigh boat on the analytical balance and the weight in grams/mL is recorded. At different flow rates it was observed that droplet formation can be tuned over a wide range of frequencies (1-40 kHz), but there is an optimal frequency that best matched the flow rate in terms of sphericity and spacing of the droplets in air (Figure 3.7 B) which is important in timing the collection of individual droplets. This result can also be expressed by comparing the optimal frequency to the pressure (Figure 3.7 C). Once the flow rate and frequency parameters have been set, the distance out of the nozzle to the droplet break off point, the shape of the droplet break off and the uniformity of the droplets after the breakoff point are used as measures of optimized parameter combinations. Generally, these interacting parameters are considered optimized once the droplet breakoff point has been minimized to less than 2.5 cm from the nozzle with spherical particle shape (Figure 3.7 D). This optimization scheme is visually demonstrated by comparing the droplets in air over the pressure/frequency combinations by imaging (Figure 3.8).

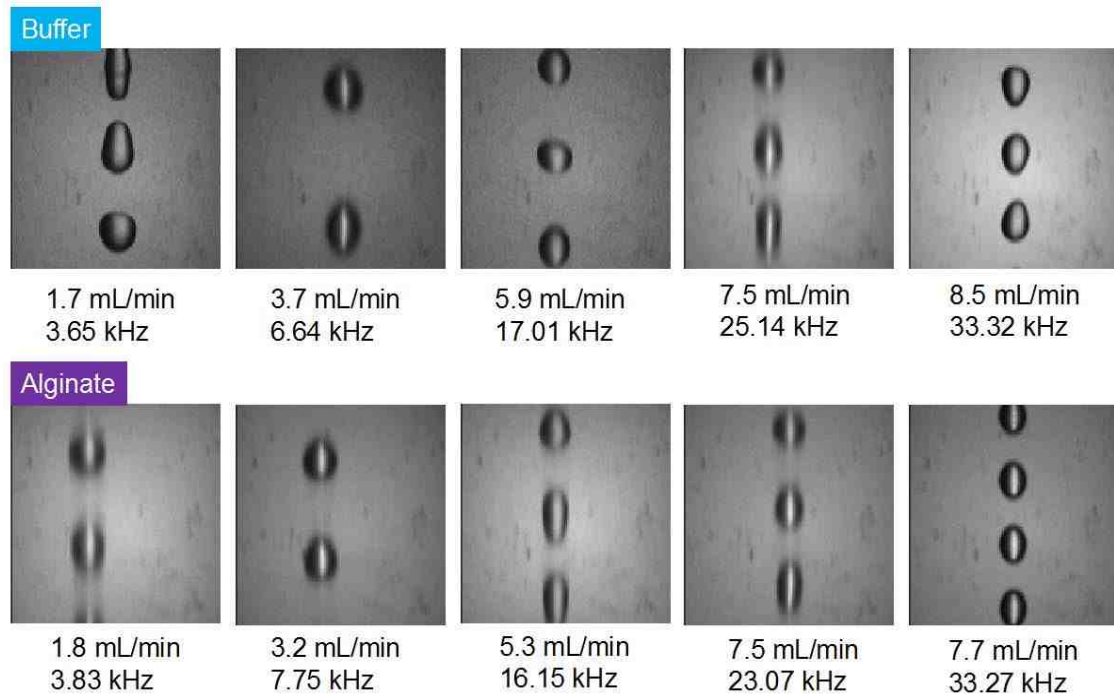
In both the dual channel and the single channel device design platforms, using simplified alginate solutions and a collection method that captures the

droplets in a stirred solidification bath has never produced particles that are consistent in shape with droplets observed in the air. Although the method here is an important demonstration of high-throughput droplet generation using highly viscous biomaterial solutions, parameters such as the crosslinked droplet diameter, monodispersity, and reproducibility are critical factors when considering the biological application of 3D cell culture for cancer research. We therefore undertook another iteration of device design and implementation to attempt to improve upon performance in capturing uniform and spherical alginate hydrogels for 3D cell culture.



**Figure 3.7 Single Channel Optimization.** Characterization of a 100  $\mu\text{m}$  single channel device over a range of (A) pressure driven measured flow rates, (B) optimal frequencies and flow rate combinations that can also be expressed as (C) the relationship of pressure to the optimal acoustic modulation frequency for spherical droplet generation as well as (D) the measured droplet breakoff as it related to the optimized modulation frequency that is coupled to a given flow rate.





**Figure 3.8 Single Channel Droplets in Air.** Droplet imaging (corresponding to the parameters measured in Figure 2.7 A-D) showing how different frequency/flow rate combinations as well as solution viscosity (by comparing buffer solution to higher viscosity 2% alginate solution) alters the volumetric shape of the droplets generated in air.

### 3.5 Chemistry and Collection for Stable Droplet Formation

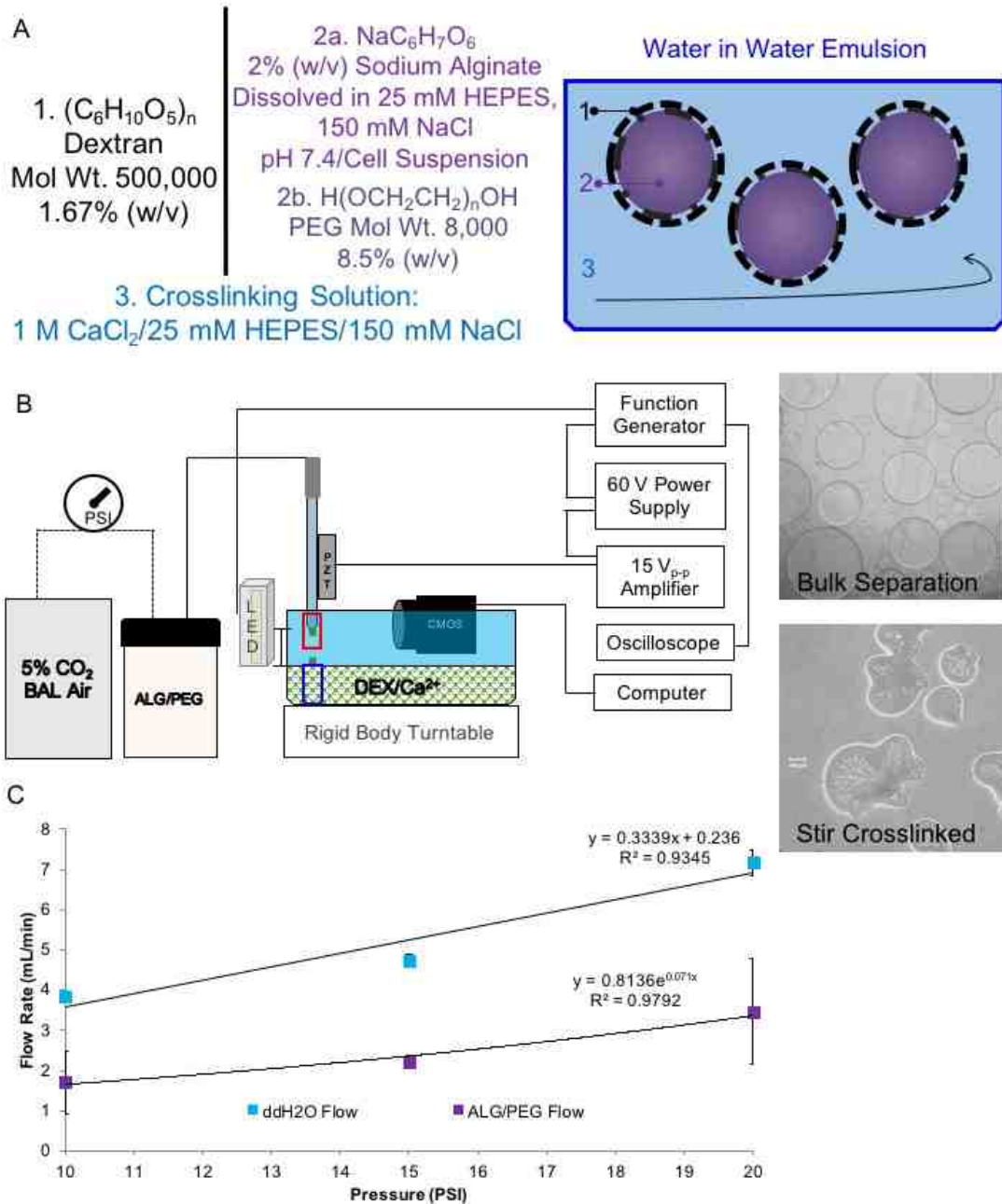
*Aqueous two-phase separation chemistry is investigated to produce a more stable droplet formation environment and solidification by rigid body rotation.*

Aqueous two-phase separation (ATPS) is a chemical phenomenon where two high molecular weight polymers are mixed in water and form an emulsion similar to the interaction when water and oil are mixed. ATPS systems of high molecular weight poly ethylene glycol (PEG) and dextran (DEX) are the most well characterized system. These systems have advantages over conventional oil-water emulsions because of cytocompatibility but have only been demonstrated to form monodisperse droplets using microfluidics systems.<sup>11</sup> Varnell et al. demonstrated the ability to incorporate alginate into the disperse phase of a PEG/DEX ATPS system and crosslink the disperse phase as it jetted in a microfluidics device.<sup>12</sup> We hypothesized that we could use a similar ATPS system in our high-throughput droplet generating instrumentation and gain improved control over the physical properties of the high-speed droplets generated with single channel devices. In parallel, we also optimized the use of a rigid body rotation system as the collection mechanism for these ATPS droplets.

The disperse (or droplet) phase is prepared by making a 4% w/v sodium alginate solution in physiological buffer containing 150 mM NaCl, 25 mM HEPES (Sigma-Aldrich), dissolved overnight, and pH adjusted to 7.4 using a high viscosity pH electrode. A separate but equal volume of 17% w/v 8 kDa PEG (Sigma-Aldrich)

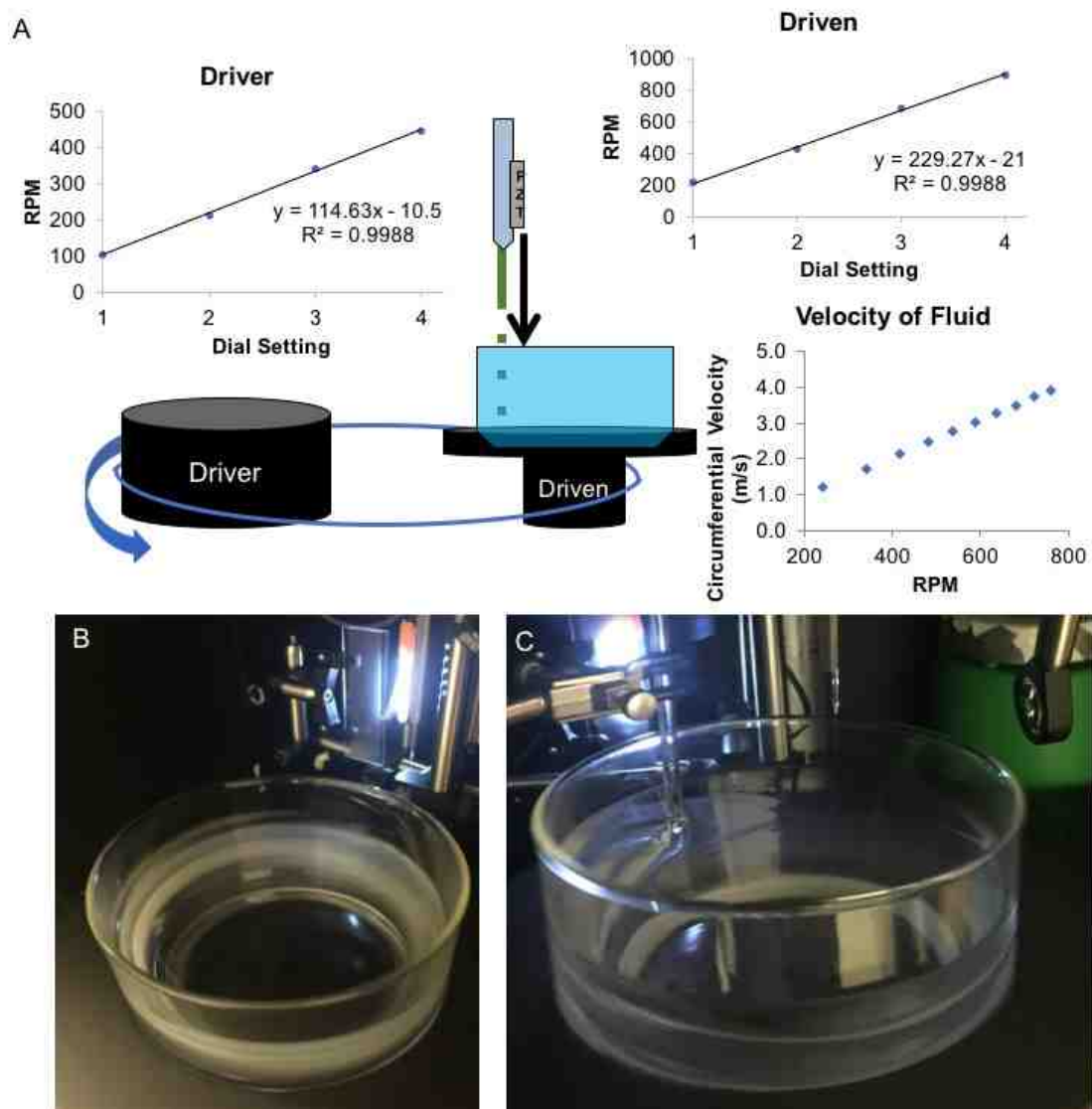
is also prepared in physiological buffer. To combine these two solutions, they are passed through a 0.45  $\mu\text{m}$  Nalgene bottle top filter and stirred. Upon mixing, the final weight percentages are 2% ALG and 8.5% PEG (Figure 3.9 A). The continuous phase is composed of 1.67% w/v 500kDa DEX (Sigma-Aldrich), 1 M  $\text{CaCl}_2$  in physiological buffer at pH 7.4 and was also sterile filtered using the 0.45  $\mu\text{m}$  bottle top assembly (Figure 3.9 A). We performed some initial characterization to be sure that this solution chemistry did indeed form an ATPS, to measure flow rates of ALG/PEG in the device to make sure it was possible to use this highly viscous composite biomaterial for acoustically modulated droplet formation with the single channel device instrumentation (Figure 3.9 B and C), and to attempt a crosslinking experiment using the stirring collection method. We found that ALG/PEG is able to flow through nozzles down to 50  $\mu\text{m}$  in diameter, can be modulated into droplets in the air with an amplified signal, and (in the absence of  $\text{CaCl}_2$ ) the disperse and continuous phase did separate in bulk and also formed an emulsion upon vortexing. However, attempting to collect droplets from a single channel device with the disperse phase flowing through the device and the continuous phase stirring in the collection bath did not produce individual spherical collected particles (Figure 3.9 B, right). Similar to the results reported above, this observation further motivated our investigations into an alternative droplet collection mechanism.

Thinking about high-throughput droplet crosslinking and why the collection attempts investigated thus far had fallen short, a simple model was developed to better understand the physics involved in the system. During droplet formation in



**Figure 3.9 Improved Single Channel Device Operations.** (A) Schematic of the ATPS chemistry, highlighting the ALG/PEG droplet phase stabilized against the continuous DEX/Ca<sup>2+</sup> phase. (B) Schematic of the droplet generating instrument and phase separation, crosslinking of droplets by stirring. (C) Flow rates of ALG/PEG compared to water as a reference.

the air, the droplets of the dispersed phase travel downward in direction with a linear velocity that depends on the nozzle diameter, the flow rate, and the acoustic modulation/droplet generation rate of the flow stream (on order 100's cm/second). Then, as the droplets submerge into the solidification bath they undergo an instantaneous change in speed and direction which we found influences droplet morphology before full solidification has occurred and produces tear drop shapes. A stirring collection bath has flow conditions that are (1) turbulent, and thus impose unpredictable impact forces on the droplets as well as shear stress, and (2) difficult to measure and calibrate in detail, making it challenging to achieve an accurate and reproducible result. So, to simultaneously simplify the system and gain more control over the environment in the crosslinking bath, a concept from classical mechanics was used to enable a more tuned and laminar droplet collection. This concept is that of rigid body rotation (RBR) where a solution (crosslinking fluid for this case in particular) contained in a flask that is spinning at a high angular frequency has centrifugal acceleration applied away from the axis of rotation and reduced shear stress because of the absence of lateral shear forces.<sup>13,14</sup> We hypothesized that the non-turbulent nature of the solution would aid in maintaining a spherical particle geometry. The fluid acceleration towards walls of the flask, (determined by the radius, angular momentum, and gravitational acceleration) causes the fluid to take on a smooth parabolic shape with an increase in height at the walls of the flask (Figure 3.10 B). The circumferential velocity of the spinning solution at a radial position towards the wall of the flask can be easily estimated


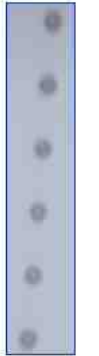
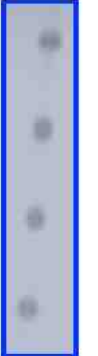
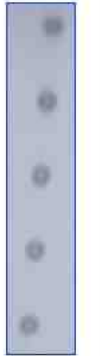

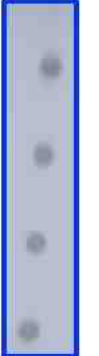
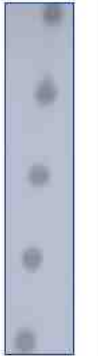
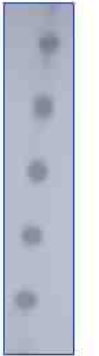


**Figure 3.10 Rigid Body Collection.** Characterization of the circumferential velocity in the RBR using a flask and the driver set up described in Section 3.3. (A) shows the gearing apparatus with driver belt and the spin characterization used to determine the circumferential velocity at different driver settings in (rev/min) for a 15 cm diameter flask. (B) shows the parabolic flow profile without mixing and (C) shows the stir rod for localized mixing in the flask just before droplet submersion.

using the gear ratio of our spin apparatus and based on the radius of the spinning flask (Figure 3.10 A).

After experimenting with many different sizes of flasks and volumes of collection solution, it was found that a 19x10 cm (diameter x height) flask with 200 mL of collection solution provides the most controllable and stable environment for high-throughput ATPS droplet generation. The system was calibrated by measuring the revolutions per minute at different driver dial settings and using the radial distance from the center of the flask to the droplet submersion location to determine the velocity (Figure 3.10 A). In fact, the first time the experiment was attempted, the constructed RBR system was so stable and uniform that the droplets were submerging into the solution repeatedly in the exact same location and ultimately created a ring of solidified gel rather than individual particles. So, a localized mixing environment was implemented into the solution by placing a glass stir rod into the solution at an angle just before the droplet submersion point, introducing enough mixing to prevent droplet recurrences in the same submersion location and solidify individual particles (Figure 3.10 C). Furthermore, the timing of the system to produce individual solidified particles rather than instances of doublet, triplets, or even beads-on-a-string morphologies is estimated to optimize a parameter that reproducibly produces individual particles in collection. For example, 100  $\mu\text{m}$  diameter droplets with an acoustic modulation of 4 kHz will need to move at least 2.5x their own length in 250  $\mu\text{s}$  to create enough space in between droplet submersions to prevent droplet piling. By manipulating flow rate and frequency combinations, it was found that up to 600  $\mu\text{m}$  of droplet spacing in air is

possible and the best set parameter to guarantee collection of individual droplets (Figure 3.11).

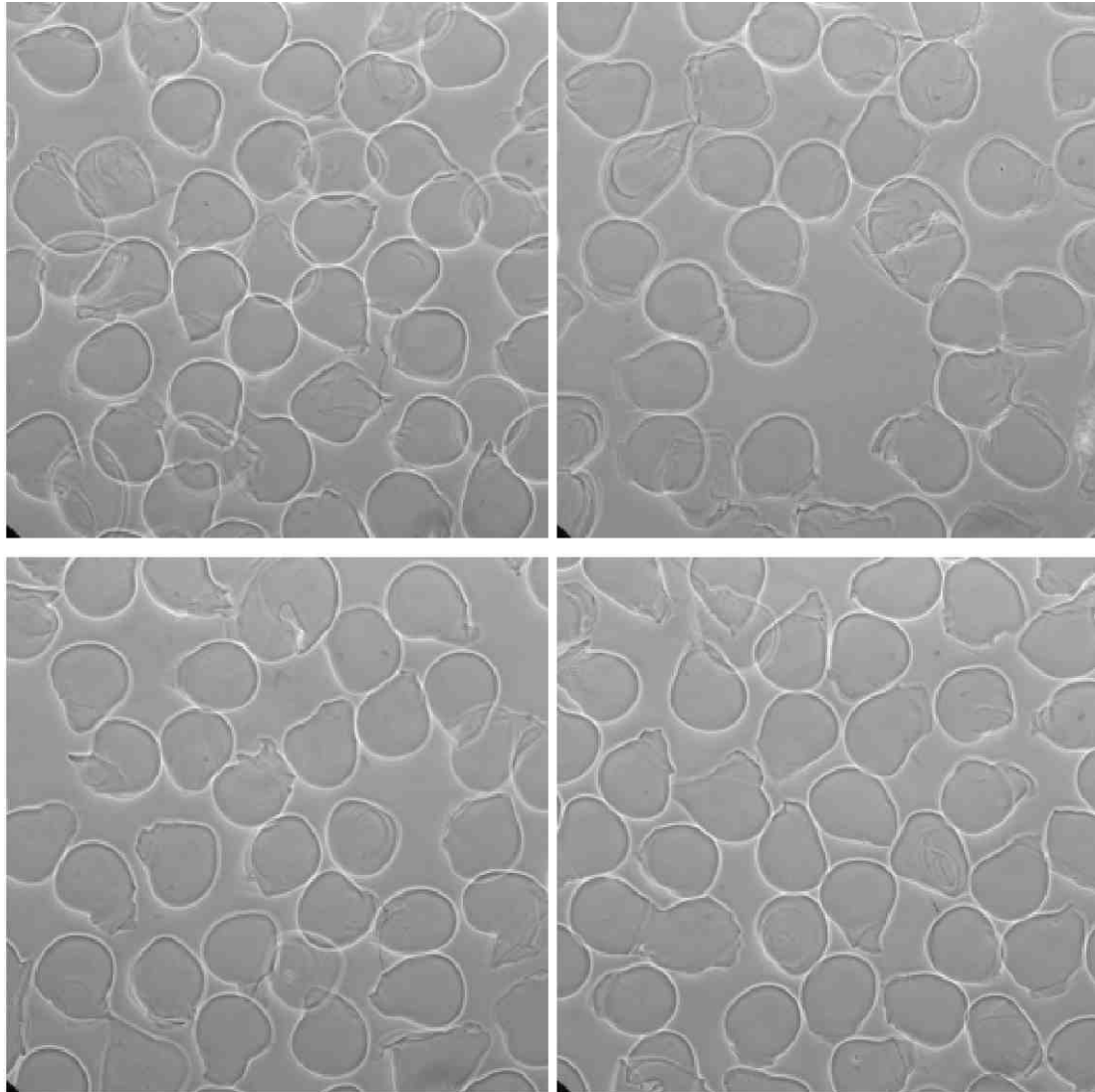
Pressure	16 PSI	16 PSI	20 PSI	20 PSI	25 PSI	25 PSI	30 PSI	35 PSI
Flow Rate	1.7 mL/min	1.7 mL/min	1.9 mL/min	1.9 mL/min	2.2 mL/min	2.2 mL/min	2.4 mL/min	2.5 mL/min
Frequency	13.27 kHz	15.59 kHz	13.25 kHz	15.59 kHz	13.25 kHz	15.64 kHz	19.14 kHz	27.27 kHz
Drop Diameter	191 $\mu\text{m}$	187 $\mu\text{m}$	201 $\mu\text{m}$	193 $\mu\text{m}$	200 $\mu\text{m}$	202 $\mu\text{m}$	202 $\mu\text{m}$	200 $\mu\text{m}$
Spacing	475 $\mu\text{m}$	379 $\mu\text{m}$	594 $\mu\text{m}$	471 $\mu\text{m}$	727 $\mu\text{m}$	580 $\mu\text{m}$	541 $\mu\text{m}$	373 $\mu\text{m}$
Microscopy of droplets generated in air								

**Figure 3.11 Characterization of Droplet Spacing in Air.** Device parameters for generating ALG/PEG droplets in the air with different spacings measured. The bolded blue boxes highlight conditions that meet the  $\sim 600 \mu\text{m}$  spacing required to produce individual solidified droplets. It is also worth noting that optimal spacing appears to be a combined effect of flow rate and frequency.



High-throughput droplets without cells have been generated and collected rather successfully using the ATPS/RBR approach. The droplets were generated using 20.2 PSI or a 2 mL/min flow rate with a piezoelectric driving signal amplified to 40 V p-p at a modulation frequency of 4.78 kHz. The RBR had a circumferential velocity of 1 m/s which was slightly more than double what the model predicted is necessary for individual droplet collection. Using ImageJ analysis to measure the geometric mean diameter (GMD) of the droplets, the population was found to have an average GMD of  $224 \mu\text{m} \pm 13 \mu\text{m}$  and an aspect ratio of 1.3 ( $n = 100$ ). As demonstrated in Figure 3.12, the collected particles are not perfectly spherical and there are some instances of shear forces causing particle elongation into tear drop shapes, however the GMD is within the diffusional mass transport limitation and particles of this morphology could still be used as scaffolding constructs for cell encapsulation and 3D cell culture.

Two conditions for cell encapsulation were investigated in the context of this approach to droplet generation in air. A human-skin malignant melanoma cell line, MEL28, was obtained from ATCC and cultured using standard 2D cell culture practices. Briefly, cells are maintained in tissue culture polystyrene T-75 flasks (Corning) with 15 mL of complete Minimal Essential Media supplemented with 10% Cosmic Calf Serum and 1% Penicillin/Streptomycin (Hyclone) in an incubator at 37° C with 5% CO<sub>2</sub> BAL AIR. MEL28 cells were harvested from dishes using 0.05% Trypsin with 1 mM EDTA (Hyclone) digestion for 10 minutes, mixed into a single cell suspension using complete media and counted using a Z1 Series Coulter Counter. The cell suspension was pelleted by centrifugation at 1500 RPM for 10



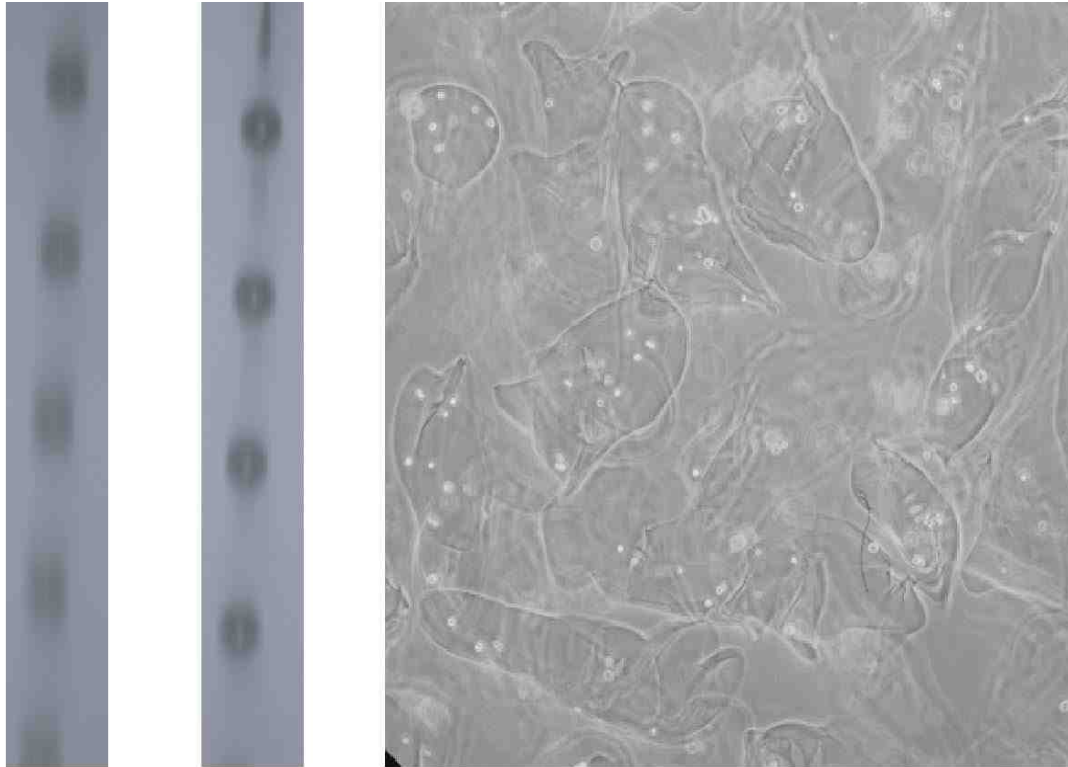
Generation Conditions:  
20.2 psi (~2 mL/min)  
4.78 kHz 40 V p-p  
RBR ~1 m/s Circumferential  
Velocity

Average Diameter: 24  $\mu\text{m}$   
SD: 13.03  
Aspect Ratio: 1.3

**Figure 3.12 Rigid Body Collected Droplets.** Brightfield microscopy of ALG/PEG droplets collected in DEX/ $\text{Ca}^{2+}$  using the RBR collection mechanism. Although particle sphericity is not perfect, the droplets are viable options for use in cell encapsulation.

minutes and resuspended with the physiological buffer of 150 mM NaCl, 25 mM HEPES, pH 7.4 with 1 mM EDTA. The cells were spun down once more into a pellet at 1500 RPM for 10 minutes and this time resuspended into 1 mL of physiological buffer with an additional 1 mM EDTA to prevent premature calcium ion crosslinking, taken up into an 18G needle/syringe (BD) and then added dropwise to 5 mL of vortexing ALG/PEG. This 6 mL cell suspension is then mixed into 39 mL of ALG/PEG to produce the final dispersed phase cell suspension with a concentration of  $1 \times 10^6$  cells/mL. This cell suspension is loaded into the pressure chamber and droplets in air were generated as described above. However, with cells added, stable well-shaped droplets are found to be generated under only limited ranges of conditions. Two sets of partially stable droplet formation conditions found were: (1) 20.2 PSI, ~2 mL/min, 6.28 kHz and (2) 25.3 PSI, ~2.2 mL/min, and 8.98 kHz with RBR collection spinning at 1 m/s with localized mixing.

In general, it was observed that adding cells to the droplet generation process shifts the robustness of the droplet formation in air. The freeze-frame droplets appear to be slightly destabilized as they transit in air, which suggests that the shift in solution viscosity by the addition of cells or even just the presence of cells in the solution alone influences the physical properties of high-throughput droplet generation in air. Additionally, when attempting to collect this population of cell encapsulating droplets by RBR, no spherical particles were captured. Instead the collection for both cases of attempted droplet capture produced a diffuse and shapeless gel (Figure 3.13).



20.2 psi  
6.28 kHz

25.3 psi  
8.98 kHz

$1 \times 10^6$  cells/mL MEL28 in ALG/PEG

**Figure 3.13 Attempted Cell Encapsulation.** Images from left to right of droplets with cells generated in the air under two conditions and an example of what is recovered from collection by RBR droplet solidification.

### 3.6 Discussion and Future Directions

The high rate of droplet generation achieved by the acoustic high-throughput droplet generation in air instrumentation platforms described provides a substantial improvement in large-scale biocompatible droplet generation compared to microfluidics and other droplet synthesis approaches. This new method of generating droplets is optimized to provide frequency-flow rate matches that enable real-time control of the droplet diameter during generation, with examples of droplet generation in air down to 100  $\mu\text{m}$  diameter using both complex (dual channel devices, ATPS chemistries) and simplified (single channel devices, RBR collection) methods. In dual channel device operations, we note that although core/sheath droplet generation in air is robust and well characterized, further optimization for particle capture and solidification is needed to fully realize the potential implications of the new method. We expect that using a redesigned ATPS solution chemistry (developed subsequently to this work and described in Chapter 4) with the *dual channel device* and instrumentation platform will enable the generation of core/sheath droplets with stabilized interfacial surface tensions. Attempting this in the future is hypothesized to produce core alginate droplets that have a sheath cushioning layer. This construct might (1) produce stable core/sheath droplets in air during transit and (2) serve to reduce impact forces and shearing effects in collection by providing a protective layer to the core droplet before full solidification is achieved in the collection bath. Similarly, the redesigned ATPS chemistries of Chapter 4 could be applied to single-channel device operations with RBR collection mechanisms. Here the droplets containing cells

would be generated out of a solution with a higher viscosity, which supports more stable droplet formation and can be acoustically modulated by an amplified signal driving the piezoelectric transducer. Further, the composition of this system would allow collection into an immiscible solution, which would enhance sphericity. Other droplet collection methods, perhaps as in bioprinting and with more advanced automation technologies could make the high-speed droplet formation amenable to collection.

The work presented in this chapter has demonstrated very high throughput production of biocompatible spherical droplets, but the ultimate long-term goal of cell encapsulation in such droplets was not realized. In subsequent work, presented in later chapters, that goal has been realized both in lower throughput microfluidic constructs (Chapter 4) and higher throughput centrifugal droplet generation methods (Chapter 5). In addition, in the course of that subsequent work, a great deal more was learned about both ATPS chemistry and control of viscosity in concentrated alginate solutions with added cells. In the future, these new insights could be applied to the techniques of high-throughput acoustic droplet generation in air presented in this chapter, with the potential of producing cell-containing droplets using these methods.

### 3.7 List of References

- (1) Wang, C.; Tang, Z.; Zhao, Y.; Yao, R.; Li, L.; Sun, W. Three-Dimensional in vitro Cancer Models: a Short Review. *Biofabrication* **2014**, *6* (2), 022001–022010.
- (2) Kim, B. J.; Hannanta-anan, P.; Chau, M.; Kim, Y. S.; Swartz, M. A.; Wu, M. Cooperative Roles of SDF-1 $\alpha$  and EGF Gradients on Tumor Cell Migration Revealed by a Robust 3D Microfluidic Model. *PLoS ONE* **2013**, *8* (7), e68422–e68429.
- (3) Colella, G.; Fazioli, F.; Gallo, M.; De Chiara, A.; Apice, G.; Ruosi, C.; Cimmino, A.; de Nigris, F. Sarcoma Spheroids and Organoids—Promising Tools in the Era of Personalized Medicine. *IJMS* **2018**, *19* (2), 615–615.
- (4) Kelm, J. M.; Timmins, N. E.; Brown, C. J.; Fussenegger, M.; Nielsen, L. K. Method for Generation of Homogeneous Multicellular Tumor Spheroids Applicable to a Wide Variety of Cell Types. *Biotechnol. Bioeng.* **2003**, *83* (2), 173–180.
- (5) Zervantonakis, I. K.; Hughes-Alford, S. K.; Charest, J. L.; Condeelis, J. S.; Gertler, F. B.; Kamm, R. D. Three-Dimensional Microfluidic Model for Tumor Cell Intravasation and Endothelial Barrier Function. *Proceedings of the National Academy of Sciences* **2012**, *109* (34), 13515–13520.
- (6) Wozniak, M. A.; Keely, P. J. Use of Three-Dimensional Collagen Gels to Study Mechanotransduction in T47d Breast Epithelial Cells. *Biol. Proced. Online* **2005**, *7* (1), 144–161.

- (7) Ligon, S. C.; Liska, R.; Stampfl, J.; Gurr, M.; Mülhaupt, R. Polymers for 3D Printing and Customized Additive Manufacturing. *Chem. Rev.* **2017**, *117* (15), 10212–10290.
- (8) Bertout, J.; Patel, S.; Simon, C. The Impact of O<sub>2</sub> Availability on Human Cancer. *Nat Rev Cancer* **2008**, *8* (12), 967–975.
- (9) Lee, K. Y.; Mooney, D. J. Alginate: Properties and Biomedical Applications. *Progress in Polymer Science* **2012**, *37* (1), 106–126.
- (10) Destruel, P.-L.; Zeng, N.; Maury, M.; Mignet, N.; Boudy, V. In Vitro and in Vivo Evaluation of in Situ Gelling Systems for Sustained Topical Ophthalmic Delivery: State of the Art and Beyond. *Drug Discovery Today* **2017**, *22* (4), 638–651.
- (11) Moon, B.-U.; Abbasi, N.; Jones, S. G.; Hwang, D. K.; Tsai, S. S. H. Water-in-Water Droplets by Passive Microfluidic Flow Focusing. *Anal. Chem.* **2016**, *88* (7), 3982–3989.
- (12) Varnell, J.; Weitz, D. A. Microfluidic Fabrication of Water-in-Water (W/W) Jets and Emulsions. *Biomicrofluidics* **2012**, *6* (1), 012808–012809.
- (13) Jansson, I.; Åkerstedt, H. O. The Dynamics of Cylinder in a Confined Swirling Flow with Constant Vorticity. *European Journal of Mechanics B/Fluids* **2015**, *54*, 98–104.
- (14) Munson, B. R.; Young, D. F.; Okiishi, T. H.; Huebsch, W. W. *Fundamentals of Fluid Mechanics, 7th Edition*.



## Chapter 4

### Microfluidics Droplet Generation

The work in Chapter 4 is the basis of a manuscript in preparation titled “Acoustically Assisted Droplet Generation using Water-in-Water Systems for Cell Culturing Microgels” with authors: Jacqueline A. De Lora<sup>1\*</sup>, Frank A. Fencel<sup>1\*</sup>, Aidira Dora Yajaira Macias Gonzales<sup>1\*</sup>, Alireza Bandegi<sup>2</sup>, Reza Foudazi<sup>2</sup>, Gabriel P. Lopez<sup>1</sup>, Andrew P. Shreve<sup>1</sup>, Nick J. Carroll<sup>1</sup>

\* Indicates co-equal contributions

<sup>1</sup>University of New Mexico, Albuquerque, NM, USA

<sup>2</sup>New Mexico State University, Las Cruces, NM, USA

#### 4.1 Generating Droplets with an Improved Microfluidics Approach

*A new microfluidics method for synthesis of size-controlled droplets useful for 3D cell culturing is achieved by coupling acoustic modulation of flow with droplet capture and solidification.*

Alginate matrices produce a robust, exceptional and inexpensive environment for 3D culture of mammalian cells, which is important in the development of therapeutics for cancer as well as in the fabrication of synthetic tissue by bioprinting.<sup>1-3</sup> Composite alginate matrices are being investigated as model biocompatible materials for cell culture because tunable compositions can be engineered to imitate properties of natural extracellular polymers and promote cell adhesion.<sup>3</sup> Alginate-based biomaterials have previously been integrated into droplet microfluidics to create droplets for 3D cell culturing. However, methods of synthesizing these droplets by conventional microfluidic devices are limited in that the drops are stabilized using oil-water emulsion solutions.<sup>4</sup> Although perfect spheres are produced by microfluidic devices owing to the high interfacial tension between emulsions of oil and water within the channels, this combination of immiscible fluids is not ideal for cell culturing because water soluble nutrients and waste products are unable to diffuse through the oil phase to maintain a homeostatic environment in the aqueous droplet. Additionally, biomolecules such as proteins may be disrupted by denaturation upon exposure to the oil phase.<sup>5</sup>

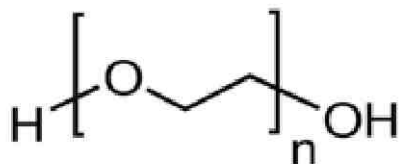
Introducing improved droplet fluidic methods to create uniform droplet hydrogels for biocompatible 3D cell culturing applications is therefore necessary. This new system uses acoustic force to break up an aqueous two-phase fluidic jet into monodispersed droplets that are then captured and crosslinked for 3D hydrogel formation and use in cell culture studies. The work emphasizes the low-cost adaptation of a household speaker (i.e. the working components removed from the housing of a portable Bluetooth speaker) and glass capillary microfluidic devices using alginate as a gelling agent within a DEX/PEG system to produce stable 3D cell encapsulating hydrogel droplets.

## 4.2 Biocompatible Device Operation Conditions

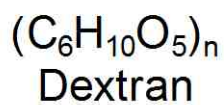
*A new microfluidic aqueous two-phase system (ATPS) for 3D hydrogel synthesis without the use of cytotoxic oils is presented and used to form stable emulsions through droplet formation by integration of acoustic modulation.*

When dissolved in water, certain multicomponent polymer solutions exhibit phase separation related to thermal equilibrium and polymer properties that include density.<sup>6</sup> Of these polymers, dextran (DEX) and poly(ethylene) glycol (PEG) exhibit phase separation at specific mass percent concentrations. This phase separation of DEX and PEG enables the creation of immiscible droplets of either phase after the solution is physically mixed and enriched. To prepare the solutions for enrichment, 5% w/w of a 100mL aqueous solution of 550 kDa DEX in 25mM HEPES buffer, 150 mM NaCl at pH of 7.4 is dissolved thoroughly. A 17% w/w 100mL aqueous solution of 8 kDa (PEG) 25mM HEPES buffer, 150mM NaCl at pH of 7.4 is dissolved separately. The two clear solutions are added to a 200 mL glass separatory funnel, mixed thoroughly, and allowed to separate into distinct, enriched phases at room temperature over 48 hours. The higher density DEX-enriched phase separates as the bottom phase in the funnel with approximately 24 mL final volume, giving it an approximate final composition of  $\approx 25\%$  DEX (w/w). The lower density PEG-enriched phase remains as the top phase in approximately 176 mL of volume, with a final concentration of  $\approx 9.4\%$  PEG w/w (Figure 4.1). The estimated phase compositions are further

Solutions mixed and enriched using a separatory funnel for 48 HRS

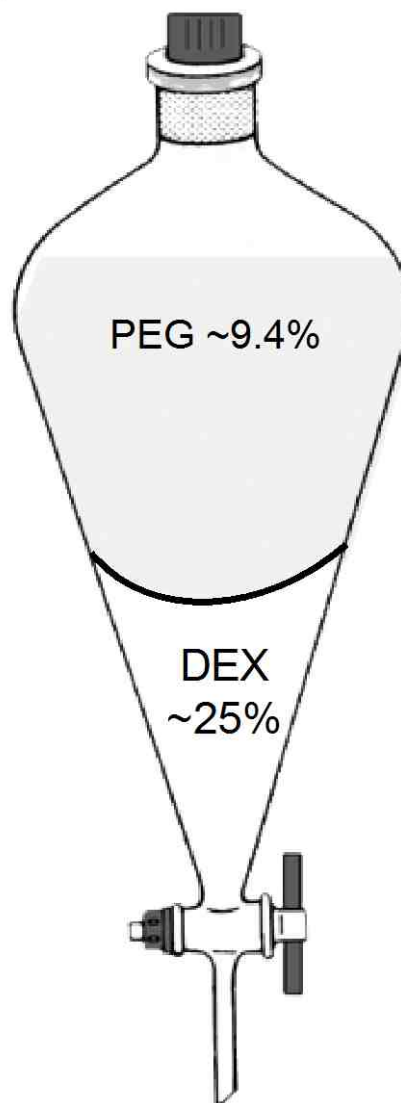


PEG Mol Wt. 8,000  
17% (w/w)



Mol Wt. 550,000  
5% (w/w)

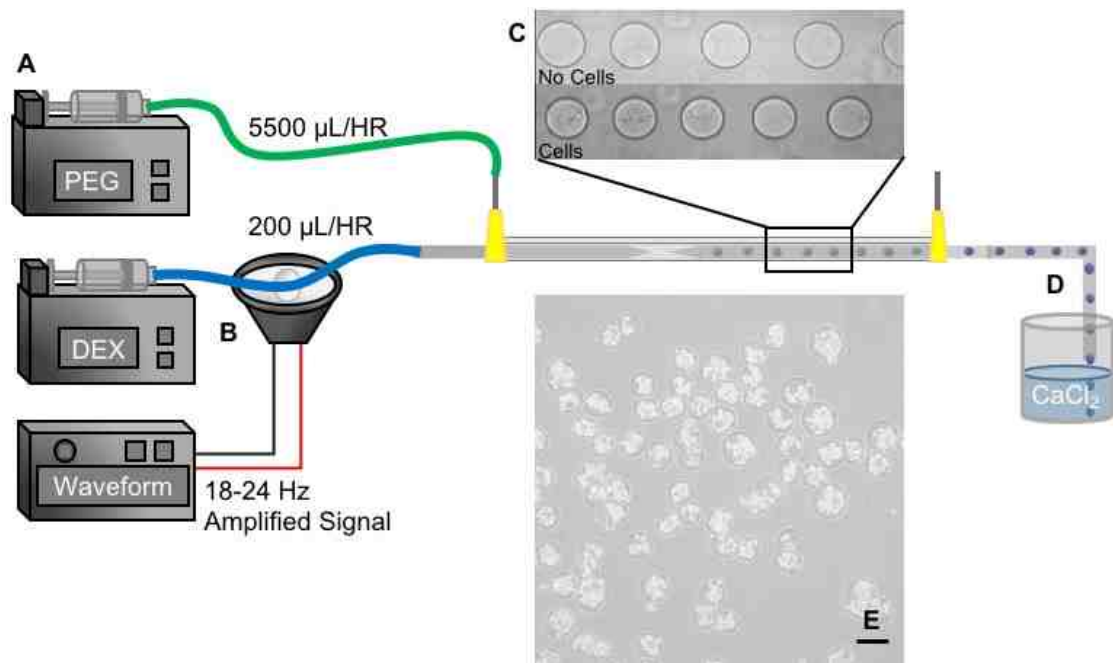
150 mM NaCl  
25 mM HEPES  
pH 7.4



**Figure 4.1 Biopolymer Enrichment.** Experimental design for phase separation, describing the initial polymer concentrations before enrichment (left) and a diagram of the partitioned phases in bulk solution within a separatory funnel.

confirmed by measuring the index of refraction of the bottom phase and comparing the value to a calibration curve of increasing w/w% DEX solutions ranging from 5% to 30% DEX (Figure 4.3 F). A small fraction of DEX and PEG is, of course, also present in the opposite phase at equilibrium (i.e., the DEX-enriched phase contains a small amount of PEG, and vice versa). Even though both of these phases are water-based, they are immiscible, including when injected into a co-flowing microfluidic device.

After this equilibration process, the majority of each phase is then slowly collected from the separatory funnel into separate vials, taking care to maintain purity by separate collection and discarding of the interfacial region as necessary. 0.5% w/w alginate is added to the collected DEX-enriched phase and stirred for 24 hours for complete mixing. The DEX-alginate and PEG solutions are filtered using a 0.2  $\mu\text{m}$  Nalgene bottle top filter to sterilize for cell culture. Oil-water interfacial tensions are on the order of tens of millinewtons/meter (mN/m), favoring stable phase separation. In contrast, the DEX and PEG aqueous solutions exhibit a very low interfacial tension on the order of hundreds of micronewtons/meter ( $\mu\text{N}/\text{m}$ ), requiring higher input energy to produce separation in microfluidic systems.<sup>5,7,8</sup> Previous work has shown that incorporating these fluids in a microfluidic device can lead to droplets only after a secondary physical force is applied to break up the fluidic jet.<sup>9</sup> This secondary force overcomes the low interfacial tension of the two aqueous phases, enhancing droplet breakup in a co-flowing system. In this new system, the secondary force is supplied by an amplified signal from a speaker to cause the breakup of DEX-alginate surrounded by PEG continuous solutions



**Figure 4.2 Microfluidics Device Schematic.** Integrating a speaker into the microfluidics device operation enables break-up of the low interfacial tension ATPS fluidic jet and provides control over the droplet size. (A) Syringe pumps serve to inject the inner and outer phase fluids into the microfluidics device. (B) The function generator/amplifier/speaker is coupled to the inner phase fluidic line and oscillates at a frequency within a small tunable range to modulate droplet formation in the device, which is observed in (C), with and without cells. (D) The droplets are collected into a bath containing calcium ions, which crosslinks the alginate in the inner phase. Subsequently, the cell-containing droplets are transferred to suspension culture for up to 9 days where (E) cell growth is observed (scale bar 100 µm).

into droplets. By directly attaching the fluidic inlet of the inner phase to a speaker, an acoustic oscillation force leads to downstream droplet breakup of a co-flowing fluidic jet and produces spherical and highly monodispersed droplets with modest throughput (Figure 4.2).

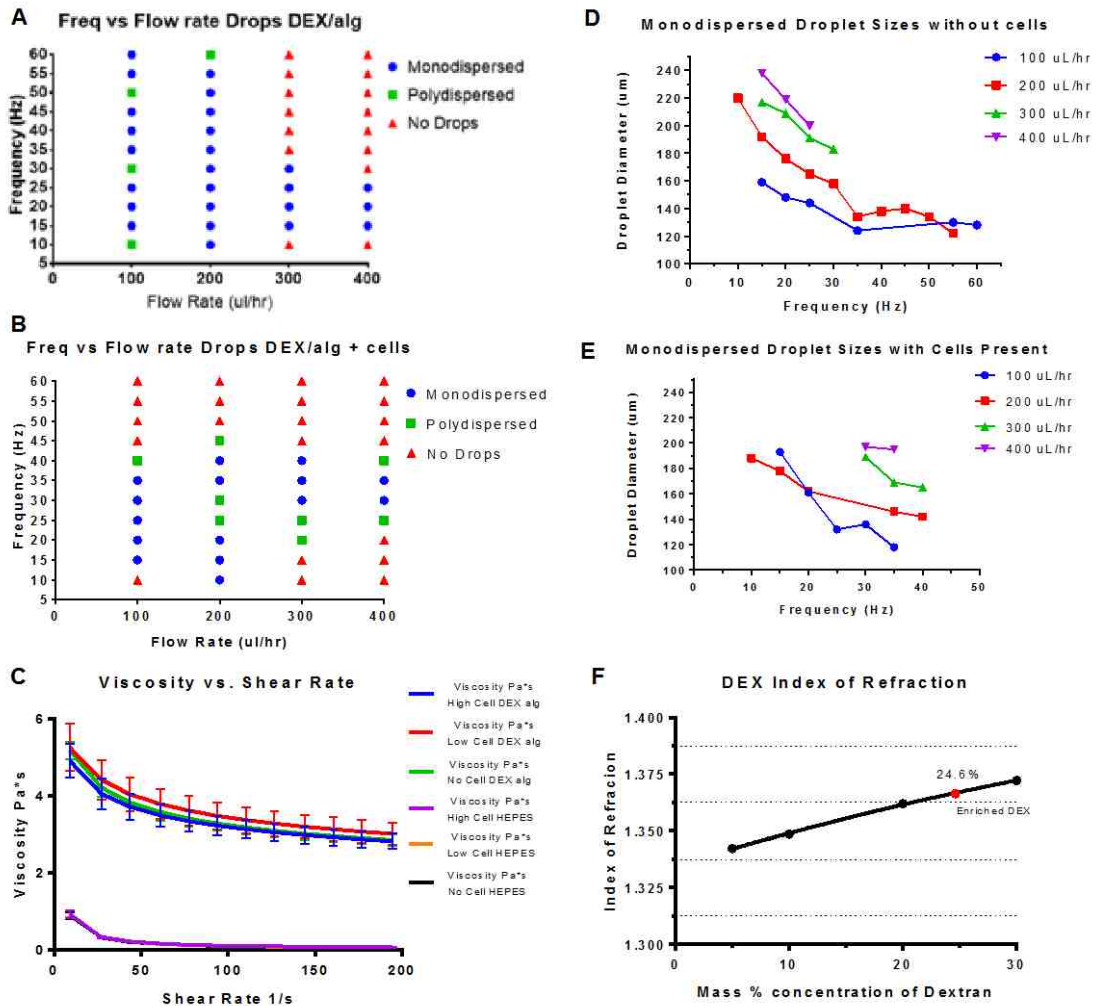
Specifically, the microfluidic glass capillary devices are built upon 25 x 75 x 1 mm Swiss glass slides. The fluidic channels are made using cylindrical borosilicate glass capillaries (World Precision Instruments, 1.0 mm O.D.) pulled to a taper with a Sutter Instrument Co. P-97 Micropipette Puller and filed with fine sand paper to produce a 100  $\mu\text{m}$  I.D. injection capillary and 200  $\mu\text{m}$  I.D. collection capillary. The injection and collection capillaries are housed in a 1.5 mm O.D. Harvard borosilicate glass square capillary tube, with tapered/filed ends interfacing in the center of the square tube. The ends of the square capillary are covered with Probe Needles M919 plastic-steel syringe tips normal to the surface of the horizontal orientation of the glass capillaries. A square pattern is cut on either side of the syringe tips to snugly cover the capillary components of the device and then sealed to the Swiss glass slide by applying Deycon Epoxy (Figure 4.2 C). The capillaries are aligned using a Zeiss Axio brightfield microscope at 10X magnification before the epoxy dries. The capillary ends and syringe tips are coupled to Scientific Commodities, Inc. LDPE 1.3208 mm OD Micro Medical Tubing and the device remains on the microscope stage for droplet synthesis. The injection tubing, coupled to the injection capillary for inner phase infusion, is taped directly to the dust cover surface of a household speaker. The speaker is connected to a Fosi Audio Stereo Audio Amplifier Mini Hi-Fi Professional Amp for



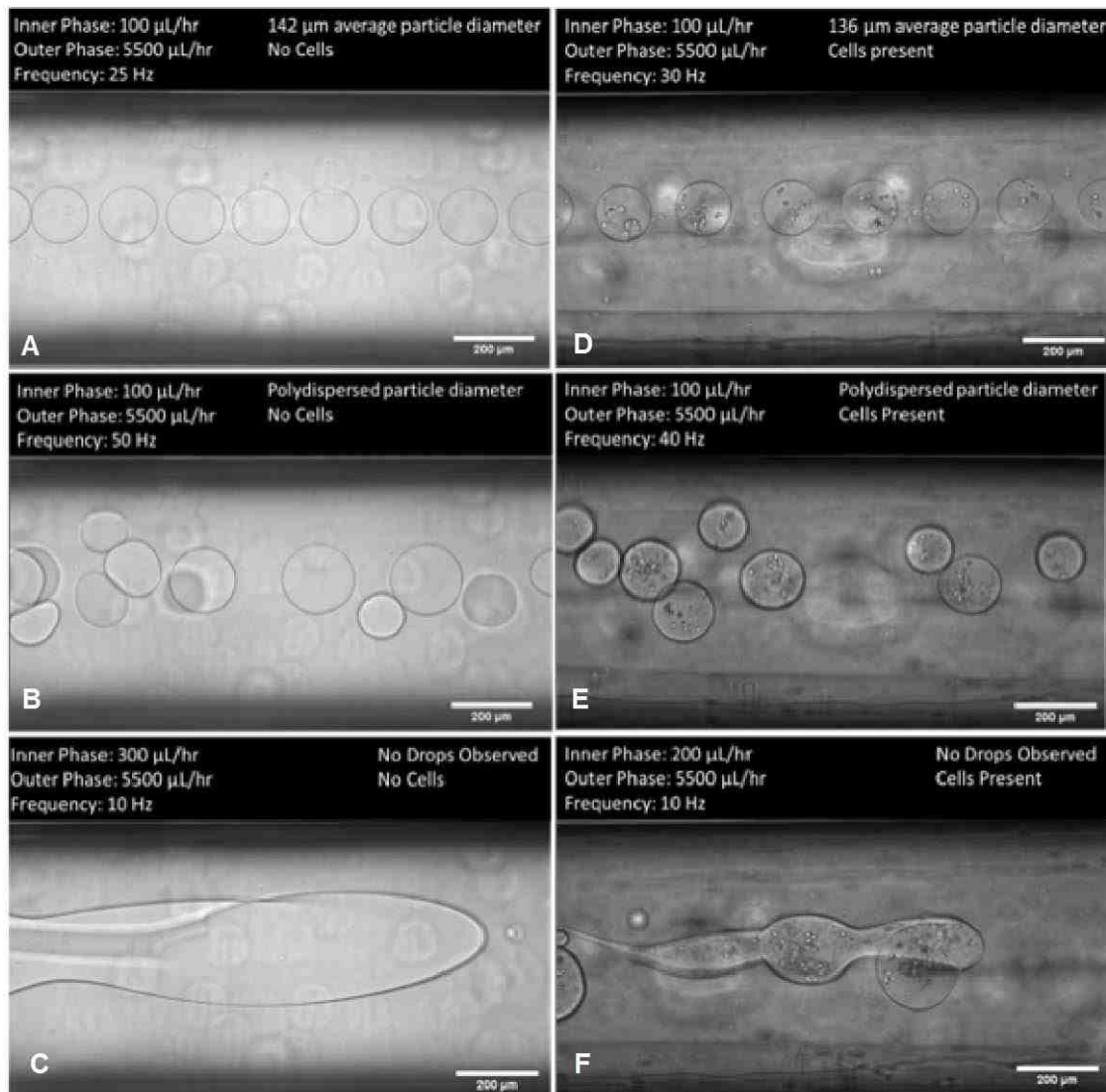
Home Speakers (50W 4 ohms, 20 Hz - 20 kHz, 0.04% THD) approximately 10 cm from the microfluidic device. The signal source for frequency input through the amplifier and into the loudspeaker is an Agilent Technologies 33250A Function/Arbitrary Waveform Generator (Figure 4.2 B) where the initial input peak-to-peak voltage is set to 10 V for all experiments. The inner phase injection tubing is connected to a Becton Dickson 10mL plastic syringe and Harvard Apparatus PHD 200 Infuse/Withdraw Syringe Pump approximately 74 cm from the microfluidic device. The inner phase syringe contains the EMT6 mouse mammary carcinoma cells (preparation described in Section 4.3) in  $\approx$ 25% enriched 550 kDa Dextran 25mM HEPES, 150mM NaCl, pH 7.4 with 0.5% by weight alginate (all chemicals from Sigma Aldrich). The tubing connected to the outer phase infusion syringe tip is connected to a Becton Dickson 60mL plastic syringe on another Harvard Apparatus Syringe Pump approximately 80 cm from the microfluidic device (Figure 4.2 A). The 60mL syringe contains the outer phase solution of  $\approx$ 10% enriched 8 kDa poly(ethylene) glycol, 25mM HEPES, 150mM NaCl solution at pH 7.4. The second syringe tip distal to the injection side is coupled with the same Micro Medical Tubing and connected to a Becton Dickson 10 mL plastic syringe for excess outer phase waste approximately 20 cm from the device. The collection capillary is connected with a short 2.38 mm O.D. Tygon tubing to another 1.0 mm O.D. World Precision Instruments borosilicate glass capillary with a  $\sim$ 90° elbow that is submerged in a 20 mL Scintillation vial with a solution of 1 M CaCl<sub>2</sub>, 150 mM NaCl, 25 mM HEPES, and pH 7.4 crosslinking solution (Figure 4.2 D).

The frequency/flow rate coupling within the device is determined by varying the input waveform signal in 5 Hz intervals from 10 Hz to 60 Hz and the inner phase flow rate across a narrow range to generate a lookup chart for optimized device operation (Figure 4.3 A without cells and B with cells). Although certain frequency and flow rate combinations produced polydispersed droplet populations (Figure 4.4 B and E), the droplet generation rate and average size of the droplets varies in accordance with the flow rate and frequency parameters to produce monodispersed droplet populations under many conditions (Figure 4.3 D, Figure 4.4 A without cells and Figure 4.3E, Figure 4.4 D with cells). Controlling the input frequency and inner phase flow rate allows the user to manipulate the size of the hydrogel droplets within the device. The droplets are sized for the longest axis using Image J and the average diameter of at least  $n = 3$  is reported in Figure 4.3 D and E, error bars are smaller than the points. This effect of droplet size variation by frequency modulation was observed in our preliminary work where enriched PEG (outer phase) was co-flowed with enriched DEX (droplet phase) and monodispersed DEX drops were formed. These observations motivated the idea to use this method as a mode of generating monodispersed hydrogels for cell culturing by incorporating alginate as a simple crosslinkable matrix for cell encapsulation. Varying the weight percent concentrations of alginate drastically changes the viscosity of the already highly viscous DEX droplet phase. High concentrations of alginate inhibit the breakup of the inner phase even with incorporation of an amplified signal to the loudspeaker. Scaling down the amount of alginate to 0.5% in the DEX droplet phase enables droplet generation after

increasing the amplitude of the applied acoustic force generated from the speaker. Collecting the flowing droplets into a  $\text{CaCl}_2$  bath allows for rapid crosslinking of the DEX-alginate gels which results in hydrogels with an almost perfect spherical shape in some cases. After characterizing the DEX-alginate droplet generation, the use of a model cancer cell line (EMT6 mouse mammary carcinoma) was investigated to determine the efficacy of using this method for 3D cell culturing over extended lengths of time.



**Figure 4.3 Characterization of a Microfluidic Device.** Measurements across a range of flow rate/frequency combinations both with and without cells have been taken. Dispersity is characterized for frequency and flow rate combinations (A and B) and monodispersed populations are sized as a function of frequency (D and E). The solution rheology with and without cells is measured across a range of shear rates (C), and the measured index of refraction for the DEX-enriched phase is placed on a calibration curve to verify that the phase separation produces DEX as the higher density, lower phase, with enriched composition matching that estimated from volume changes (F).



**Figure 4.4 Device Operating Regimes.** Microscopy examples of different droplet generation regimes. Droplets with and without cells formed as monodispersed populations (A and D), polydispersed regime (B and E), and jetting/no droplet formation (C and F).

### 4.3 Cell Suspension and Encapsulation

*Methods are developed for suspending cells in highly viscous DEX-alginate solutions for droplet generation, collection, and subsequent suspension culture for growth into spheroid-like structures.*

The EMT6 mouse mammary carcinoma cell line is used for these encapsulation studies. This cell line is well characterized to grow in conventional tumor spheroid models in standard culture conditions,<sup>10</sup> and a protocol is developed here for preparing a single cell suspension in the DEX-alginate droplet phase. EMT6 mouse mammary carcinoma cells are maintained using standard sterile cell culture conditions (37°C, 5%CO<sub>2</sub>) in 150 mm tissue culture treated polystyrene dishes (Corning) with 20 mL of Minimal Essential Media supplemented with 10% Fetal Bovine Serum and 1% Penicillin/Streptomycin (Sigma-Aldrich) to grow up for encapsulation. The concentration of cells/droplet is easily adjusted for desired occupancies by changing the initial cell encapsulation concentration. In general, if desired cell/droplet occupancy is 10 cells/100 µm diameter droplet then 2x10<sup>7</sup> cells/mL is required for the encapsulation protocol. Cells at ~80% confluence in 150 mm dishes (depending on the desired final concentration) are washed with 3 mL of 0.5% Trypsin and then incubated in 5 mL of 0.5% Trypsin (Sigma-Aldrich) for up to 30 minutes to release attached cells. The cells are then washed off the dish with gentle pipetting by adding 5 mL of media to the 5 mL of trypsin and cells. This 10 mL cell suspension is transferred into a 50 mL centrifuge tube (and

combined with cells recovered from additional 150 mm dishes if applicable), a sample is taken for cell counting using a Z1 Series Coulter Counter and centrifuged at 1500 RPM for 10 minutes to pellet. The cell concentration to be used is determined, the cell pellet is resuspended into 20 mL physiological buffer (25 mM HEPES, 150 mM NaCl, pH 7.4), and the volume corresponding to the desired final cell concentration is transferred to a fresh 50 mL centrifuge tube. This adjusted cell suspension is then centrifuged at 1500 RPM for 10 mins to wash and pellet. The physiological buffer supernatant is then aspirated and the cell pellet is resuspended into 500  $\mu$ L of sterile filtered DEX-alginate by gentle pipetting using a 1000  $\mu$ L pipette. The 500  $\mu$ L of DEX-alginate cell suspension is drawn up into an 18G needle/10 mL syringe (BD) and then added dropwise to 2.5 mL of DEX-alginate in a 50 mL centrifuge tube while vortexing. The 3 mL cell suspension is then passed through a 40  $\mu$ m cell strainer test-tube filter insert (BD Falcon) into a fresh 50 mL centrifuge tube to produce the final single cell suspension in DEX-alginate. A sample is taken from this solution to count the final cell concentration as there is some cell loss (roughly 5% of the population) during the protocol due to the highly-viscous nature of the DEX-alginate and the filtering out of any cell clumps. This dropwise vortex, mixing, and filtering of the DEX-alginate and cells guarantees a single cell suspension which is paramount to avoiding clogs in the microfluidics device. The cell suspension is loaded into the 10 mL syringe described in Section 4.2 for droplet synthesis in the microfluidics system.

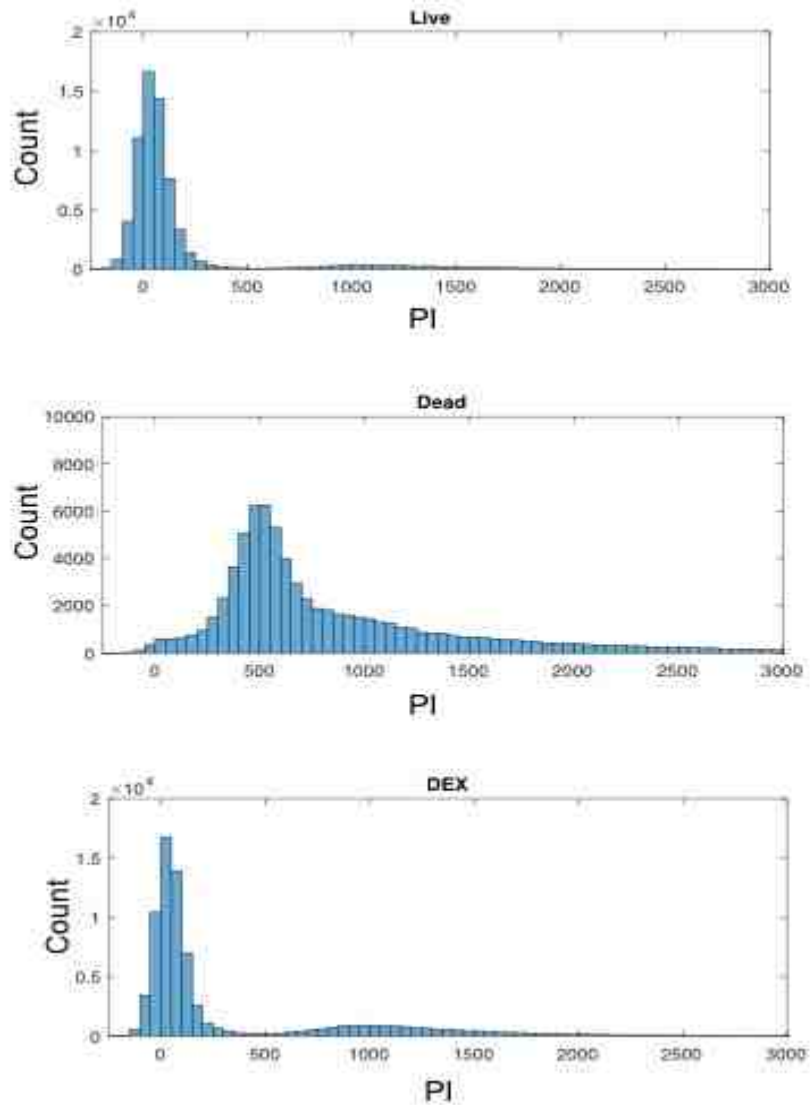
After adding the cells to the DEX-alginate phase, we operated the system at various inner phase flow rate and frequency combinations to determine if the

addition of the cells would affect droplet generation. The resultant matrix of droplet generation with cells varies from that of the inner phase solutions without cells incorporated (Figure 4.3 A and B). This observation motivated the investigation of the rheological properties of the fluid components both with and without cells. Rheological analysis was completed using a Discovery Hybrid Rheometer HR-3 with a 40 mm 2.0 cone plate and Peltier plate steel geometry for temperature-controlled experiments. The samples analyzed are as follows: (1) DEX-alginate in physiological buffer with no cells, “low”  $3 \times 10^6$  cells/mL, and “high”  $3 \times 10^7$  cells/mL and (2) physiological buffer with no cells, “low”  $3 \times 10^6$  cells/mL, and “high”  $3 \times 10^7$  cells/mL. Comparing the viscoelastic behavior of these solutions would indicate whether an order of magnitude change in cell concentration affects viscosity, which could hypothetically then affect the droplet generation capabilities of the microfluidic device. Each sample was placed on the rheometer twice and the experiments were repeated in triplicate per sample. The rheological characteristics of the samples were analyzed with two different methods. The first method is by frequency sweep with the angular frequency from 628 to 0.1 rad/s and the second by flow ramp with shear rate from 0.01 to 1000/s. The Young’s and Storage modulus as well as complex viscosity is calculated from the frequency sweep test. The dynamic viscosity is obtained from the flow ramp test. The variations in viscosity in the DEX-alginate groups as well as in the buffer groups are within error of each other for each solution which leads to the conclusion that the presence of cells in the droplet phase at both low and high cell concentrations does not substantially change the viscosity (Figure 4.3 C). However, the droplet



generation matrix with cells is still limited upon addition of cells (Figure 4.3 A and B). This may be caused by an observed cell aggregation within the inner phase solution over the duration of a droplet synthesis experiment. As mentioned in Section 4.1, a well-known challenge with the interface of microfluidic droplet generation and cell culture is the necessity for low volumetric flow rates, where cells in a biomaterial suspension may be out of ideal culture conditions for up to hours at a time. The aggregation of cells over time is a natural phenomenon that has been exploited for conventional tumor spheroid formation<sup>11</sup>, but in our case, influences the injection of the inner phase solution out of the glass microcapillary and therefore changes the dynamic rate of flow affecting the droplet generation.

To demonstrate that our new method of 3D cell encapsulation with an ATPS system and the time to synthesize enough droplets for relevant biological assays is still a biocompatible approach, we measured the fraction of live to necrotic cells recovered from the inner phase directly after droplet generation using a Propidium iodide flow cytometric assay (Figure 4.5). Briefly, upon completion of droplet synthesis we assay the cells from the remaining cell suspension in DEX-alginate for necrosis by propidium iodide. The DEX-alginate cell suspension is compared to LIVE and DEAD control populations. The LIVE cells are processed with trypsinization into a single cell suspension and remain in complete media on ice during the experiment while the DEAD control cells are generated by suspension in 50% ethanol for 60 minutes at 37°C and 5% CO<sub>2</sub> in the incubator. Once the

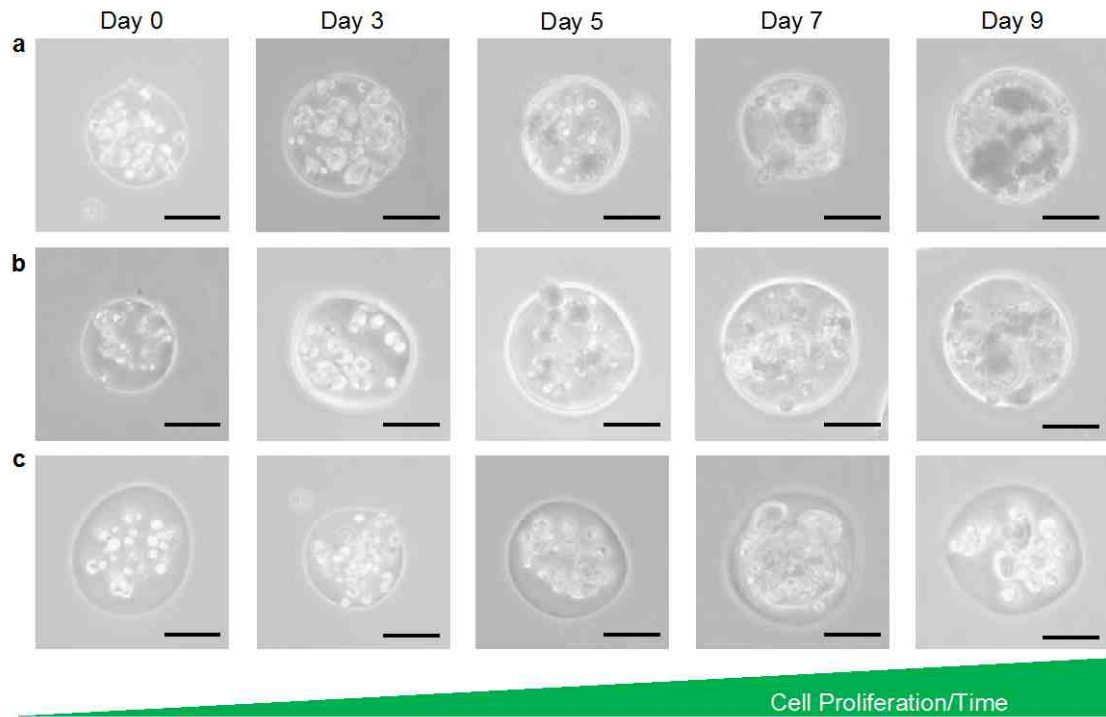


**Figure 4.5 LIVE/DEAD Assay.** The results from a necrosis (propidium iodide) flow cytometric assay indicate that the polymer solutions and the method to encapsulate the cells are biocompatible and the slight elevation in necrosis in the DEX sample in comparison to the live control is because of post processing effects due to centrifugation of cells out of the DEX-alginate solution.

DEX-alginate cell suspension has been in ambient conditions for the duration of droplet generation (~2 hours), it is transferred to a 15 mL centrifuge tube and diluted by the addition of physiological buffer to dilute the viscosity of the solution. The suspension is centrifuged at 3000 RPM for 10 minutes. In this first wash, the cells form a band towards the bottom of the test tube but have not yet been fully pelleted, so ~5 mL of the diluted DEX-alginate is removed by aspiration and 5 mL of physiological buffer is added and vortexed. The tube is centrifuged at 3000 RPM for 10 minutes. This wash/centrifugation protocol is repeated once more to pellet the cells at the bottom of the tube and remove as much residual DEX-alginate solution as possible. The DEX-alginate-buffer supernatant is aspirated and the cells are washed in 10 mL of physiological buffer followed by aliquoting into 4, 15 mL test tubes and centrifugation at 2000 RPM for 10 minutes. The staining protocol is then followed as described in Alexa Fluor 488® annexin V/Dead cell apoptosis Kit with Alexa Fluor 488® annexin V and PI for flow cytometry from Invitrogen, but in this case only for necrotic cell death. The samples are analyzed (100,000 events per group on the gated population) using an Attune NxT flow cytometer. Quantitatively, there is no statistically significant difference between the live control group and our experimental (cells in DEX-alginate) group for necrosis. There was a small qualitative increase in the necrosis of the cells in the DEX-alginate however this is likely due to rigorous dilution, washing, and centrifugation protocol necessary to recover the cell population from the viscous DEX-alginate pre-gel and not due to exposure to the biomaterial.

Over the course of droplet synthesis (about once/hour), crosslinked droplets are removed from the setup and allowed to settle in the 1 M CaCl<sub>2</sub> buffer so that the excess Ca<sup>2+</sup> may be removed and the cell encapsulating droplets can be transferred by gentle pipetting into a temperature equilibrated 125 mL spinner flask bioreactor (Corning) with 125 mL of complete media adjusted to pH 7.4 with 25 mM HEPES. For the  $t_0$  initial time point, a 20  $\mu$ L sample of droplets is pipetted onto a microscope slide (VWR) and placed onto a brightfield microscope for imaging using a Nikon camera and SPOT Basic software. Once the total cell encapsulating droplet population has been transferred into the spinner flask bioreactor, the head space is backfilled with 5% CO<sub>2</sub> and placed onto a slow stir plate in a warm room maintained at 37°C for the duration of the time course (9 days). Cells have been encapsulated on 3 separate occasions to demonstrate the reproducibility of the methodology and at days 3, 5, 7, and 9, samples are taken from the cultures for imaging (Figure 4.6) as described above. At these times, the culture media is also changed. In that process, the spinner flask bioreactor is removed from the stir plate, allowing the droplets to settle to the bottom of the flask. Once settled, the media is aspirated being careful to leave about 20 mL at the bottom so as to not aspirate droplets and then refilled to a final volume of 125 mL with temperature equilibrated complete media and backfilled as before. To validate a cell recovery solution that can dissolve the alginate crosslinks and recover the cells into a droplet-free suspension, on day 9 the total droplet population is collected by allowing the droplets to settle and then aspirating the media until 20 mL of media and droplets remain in the spinner flask. The 20 mL of droplets and media is

pipetted into a 50 mL centrifuge tube and the droplets are allowed to settle once more (~10 minutes). The remaining media is carefully aspirated and 20 mL of a droplet dissolving buffer (0.5% trypsin, 50 mM sodium citrate, 25 mM HEPES, 150 mM NaCl pH 7.4) is added to the droplets in the 50 mL tube. The tube is incubated at 37°C for 30 minutes with vortexing every 5 minutes to encourage dissociation of cell aggregates. The recovered cells in dissolving buffer are then centrifuged at 1500 RPM for 10 minutes, resuspended into 1 mL of physiological buffer and counted using the Coulter Counter. Although the data is relevant but not conclusive due to the limitation of a small sample size, droplet dissolution and cell pelleting was observed. This method will be applicable for quantitative growth rate studies in the future.



**Figure 4.6 Encapsulation and Proliferation Results.** Encapsulating cells in DEX-alginate droplets produces a reliable platform for cell proliferation and eventual formation into multicellular tumor spheroids. EMT6 mouse mammary carcinoma cell encapsulation was performed in triplicate at initial concentrations (rows a, b, and c) and observed to proliferate up to the end of the culture time course of 9 days. (scale bars 50  $\mu\text{m}$ )

#### 4.4 Cell Growth Over Time in Droplets

*Acoustically assisted droplet generation for cell encapsulation in a microfluidics device is demonstrated to be a reliable method for controlling the initiation of 3D cell cultures.*

The viability of these microgels proved exceptional after 9 days of suspension culture in spinner flask bioreactors. We demonstrated the robustness of the system by encapsulating EMT6 cells on 3 separate occasions, imaged the proliferation of each culture immediately after encapsulation and at 3, 5, 7 and 9 days, and developed a method to recover cells from the hydrogels for counting (Figure 4.6). The cell counting results are not presented because of difficulties in acquiring enough cells to count a sample above the limit of detection of the cell counter. Having a large enough droplet population to then have enough cells in a sample is a systematic limitation for microfluidics discussed before and so the growth curve presented is qualitative. It appears that there is a lag phase in the proliferation rate of the cells from initial encapsulation to day 3 which is likely caused by a low cell encapsulation concentration (~10 cells/droplet) and the cells being isolated from one another. Once cell-cell contact is established, the growth rate appears to become more exponential and cellular aggregation as in tumor spheroid formation is observed. Acoustically assisting water/water droplet generation for 3D cell culturing hydrogels provides a low cost and reproducible method to grow and study cell systems across multiple applications. This

technology provides a robust method to generate 3D hydrogels for cell culture and has the potential to be used alongside drug discovery platforms or for 3D printing applications.



#### 4.5 Discussion and Future Directions

This work has demonstrated the design and implementation of a technologically robust microfluidics droplet generating platform for the encapsulation and growth of cells. However, the overall throughput of the microfluidics device operations is a concern when looking to employ these types of systems for downstream biological assays. Although miniaturization can be viewed as a cost-effective approach to using less material for greater experimental output<sup>6,7</sup>, the small-scale channel dimensions (both in soft-lithography PDMS designs and glass capillary microfluidic assemblies) limit volumetric flow rates to the order of  $\mu\text{L}/\text{hour}$ . This flow rate translates to droplets being generated on the order of about 10 droplets/second, depending on the viscosity of the solutions, geometry in the device, external forces, and total flow rate. This droplet production rate is considerably smaller than other platforms (such as those detailed in Chapters 3 and 5), which must be taken into account when the droplet population is intended for biological applications. Generally, growth curves and other flow cytometric bioassays require recovery of  $2 \times 10^5$  cells from 3D cell cultures per time point for robust statistical analysis. In order to produce  $1 \times 10^6$  droplets from a microfluidics device with a droplet phase flow rate of  $100 \mu\text{L}/\text{hour}$  it would take 10 hours plus device initiation, which is nowhere near the throughput required to complete a curve that extends over 7 days. Because of this time limitation for cytocompatibility, we only operated the device for 2 hours and were therefore limited in the types of downstream biological assays possible.

Generally speaking during device operations, the cells may be at room temperature without gas or humidity control and likely out of a sterile environment. Essentially, the cells suspended in the droplet phase would be out of cell culture conditions for lengths of time that are not explicitly cytocompatible and possibly cytotoxic depending on the cell line being used. Techniques to increase cytocompatibility are being established. Examples include (1) having stringent sterilization standards if the instrumentation cannot be setup in a biological safety hood (which then also limits the types of cells one may use for encapsulation); (2) building the entire system in a sterile incubator chamber; (3) if the instrumentation must be under ambient conditions on the benchtop, sequential injection of the cell containing droplet phase by integration of switch valves such that the cell suspension being injected is only out of compatible conditions for a minimized time period; and (4) parallelizing the device so that many side-by-side channels (on order 100 channels/chip), all with the same task and branched fluidic injections, are operated simultaneously to increase the throughput.

Our initial work provides a microfluidics platform with feasibility for scaling up by incorporating higher volume microfluidics with an acoustic actuator to yield larger, uniform populations of 3D cell encapsulating hydrogels. This method of encapsulating biological components might also be used to trap biological structures such as giant unilamellar vesicles (GUVs), which have notoriously limited stability in vitro.<sup>12</sup> Finally, using this gentle method to encapsulate biological components may prove to aid in study for drug discoveries since the alginate matrix provides a biomimetic 3D matrix for cell growth.

#### 4.6 List of References

- (1) Andersen, T.; Auk-Emblem, P.; Dornish, M. 3D Cell Culture in Alginate Hydrogels. *Microarrays* **2015**, *4* (2), 133–161.
- (2) Tabriz, A. G.; Hermida, M. A.; Leslie, N. R.; Shu, W. Three-Dimensional Bioprinting of Complex Cell Laden Alginate Hydrogel Structures. *Biofabrication* **2015**, *7* (4), 045012–045012.
- (3) Knight, E.; Przyborski, S. Advances in 3D Cell Culture Technologies Enabling Tissue-Like Structures to Be Created in Vitro. *J. Anat.* **2014**, *227* (6), 746–756.
- (4) Baroud, C. N.; Gallaire, F.; Dangla, R. Dynamics of Microfluidic Droplets. *Lab Chip* **2010**, *10* (16), 2032–14.
- (5) Ziemecka, I.; van Steijn, V.; Koper, G. J. M.; Rosso, M.; Brizard, A. M.; van Esch, J. H.; Kreuzer, M. T. Monodisperse Hydrogel Microspheres by Forced Droplet Formation in Aqueous Two-Phase Systems. *Lab Chip* **2011**, *11* (4), 620–624.
- (6) Mace, C. R.; Akbulut, O.; Kumar, A. A.; Shapiro, N. D.; Derda, R.; Patton, M. R.; Whitesides, G. M. Aqueous Multiphase Systems of Polymers and Surfactants Provide Self-Assembling Step-Gradients in Density. *J. Am. Chem. Soc.* **2012**, *134* (22), 9094–9097.
- (7) Jian, C.; Poopari, M. R.; Liu, Q.; Zerpa, N.; Zeng, H.; Tang, T. Reduction of Water/Oil Interfacial Tension by Model Asphaltenes: the Governing Role of Surface Concentration. *J. Phys. Chem. B* **2016**, *120* (25), 5646–5654.

- (8) Peters, F.; Arabali, D. Interfacial Tension Between Oil and Water Measured with a Modified Contour Method. *Colloids and Surfaces A: Physicochemical and Engineering Aspects* **2013**, *426*, 1–5.
- (9) Song, Y.; Shum, H. C. Monodisperse W/W/W Double Emulsion Induced by Phase Separation. *Langmuir* **2012**, *28* (33), 12054–12059.
- (10) Freyer, J. P.; Sutherland, R. M. Proliferative and Clonogenic Heterogeneity of Cells From EMT6/Ro Multicellular Spheroids Induced by the Glucose and Oxygen Supply. *Cancer Research* **1986**, *46*, 3513–3520.
- (11) Kelm, J. M.; Timmins, N. E.; Brown, C. J.; Fussenegger, M.; Nielsen, L. K. Method for Generation of Homogeneous Multicellular Tumor Spheroids Applicable to a Wide Variety of Cell Types. *Biotechnol. Bioeng.* **2003**, *83* (2), 173–180.
- (12) Trantidou, T.; Friddin, M.; Elani, Y.; Brooks, N. J.; Law, R. V.; Seddon, J. M.; Ces, O. Engineering Compartmentalized Biomimetic Micro- and Nanocontainers. *ACS Nano* **2017**, *11* (7), 6549–6565.

## **Chapter 5**

### **Centrifugal Droplet Generation for Cell Encapsulation**

Chapters 5 and 6 are the basis of a manuscript in preparation titled “Alginate droplet generation for high-throughput cell encapsulation and formation of multicellular spheroids using modified centrifugal synthesis methods” with authors: Jacqueline A. De Lora, Jason Velazquez, James P. Freyer, and Andrew P. Shreve

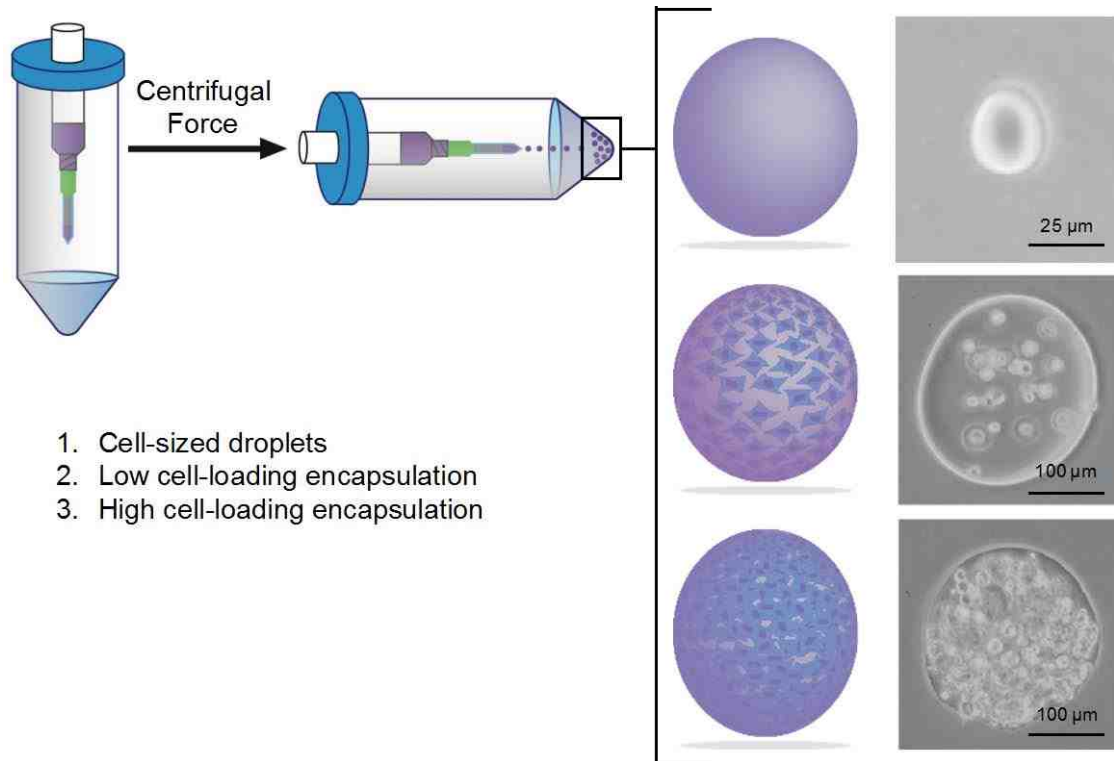
University of New Mexico, Albuquerque, NM, USA

## 5.1 Robust Droplet Generation by Centrifugal Synthesis

*An improved high-throughput 3D culture method is presented using simple alginate gelation chemistry to encapsulate cells in large and uniform droplet populations produced by centrifugal force in a standard laboratory centrifuge.*

Cell encapsulation in droplet-based alginate hydrogels is conventionally divided into two general approaches. The first is direct droplet generation where alginate is dispensed out of a nozzle (sometimes by pressure driven fluid flow), forms droplets in an air gap, and submerges into a calcium solidification solution. These types of platforms can achieve high-throughput droplet generation depending on engineered enhancements to the system but are more complex in construction. Implementation into the laboratory is difficult as the costly and complex instrumentation comes with the need for a skilled user to operate.<sup>1</sup> The second is indirect droplet generation using microfluidic emulsion systems to form droplets within microchannels using the difference in surface tension between two immiscible fluids to generate droplets. Although more biocompatible chemistries are being investigated to avoid the use of oils in these types of systems (Chapter 4), it is well recognized that the main drawbacks to microfluidic droplet generation are complicated set-ups and low throughput.<sup>2,3</sup> Recent studies have demonstrated the potential for droplet generation with biocompatible chemistries by centrifugal synthesis; this process uses centrifugal forces with in-house fabricated devices and readily available laboratory equipment to produce large amounts of uniform

droplets.<sup>4-6</sup> However, these methods for droplet generation have yet to be fully implemented for (1) the generation of cell-sized droplets that enable the stabilization and study of biological components such as vesicles and proteins outside the context of cellular compartmentalization; (2) the formation of spherical constructs for the encapsulation of low cell occupancies; and (3) the generation of instant multicellular tumor spheroids (iMTSs) by encapsulating high cell occupancies (Figure 5.1). This chapter demonstrates the use of improved centrifugal droplet generating device designs for the first instance of cell-sized droplet generation by centrifugal force, cell encapsulation in size-controlled and uniform calcium alginate droplet populations, and the generation of droplets that contain enough cells to instantly form a MTS. The improved methodology, from device fabrication and operation to establishing cell culture protocols, is easily implemented into standard cell culture practices and accessible to a wide range of laboratories interested in adopting 3D cell culture.



**Figure 5.1 Centrifugal Droplet Generation and Applications.** General design, implementation, and application space for centrifugal droplet generation. Clockwise from top left shows a diagram of the high-level device design and droplet generation by centrifugal force. Right panel shows both a diagrammatic representation and microscopy of small droplets without cells, as well as larger droplets with a low concentration of cells and with a high concentration of cells. Bottom left is a concise description of the droplet populations depicted in the panel on the right.



## 5.2 Centrifuge tube assemblies and hybrid nozzle designs

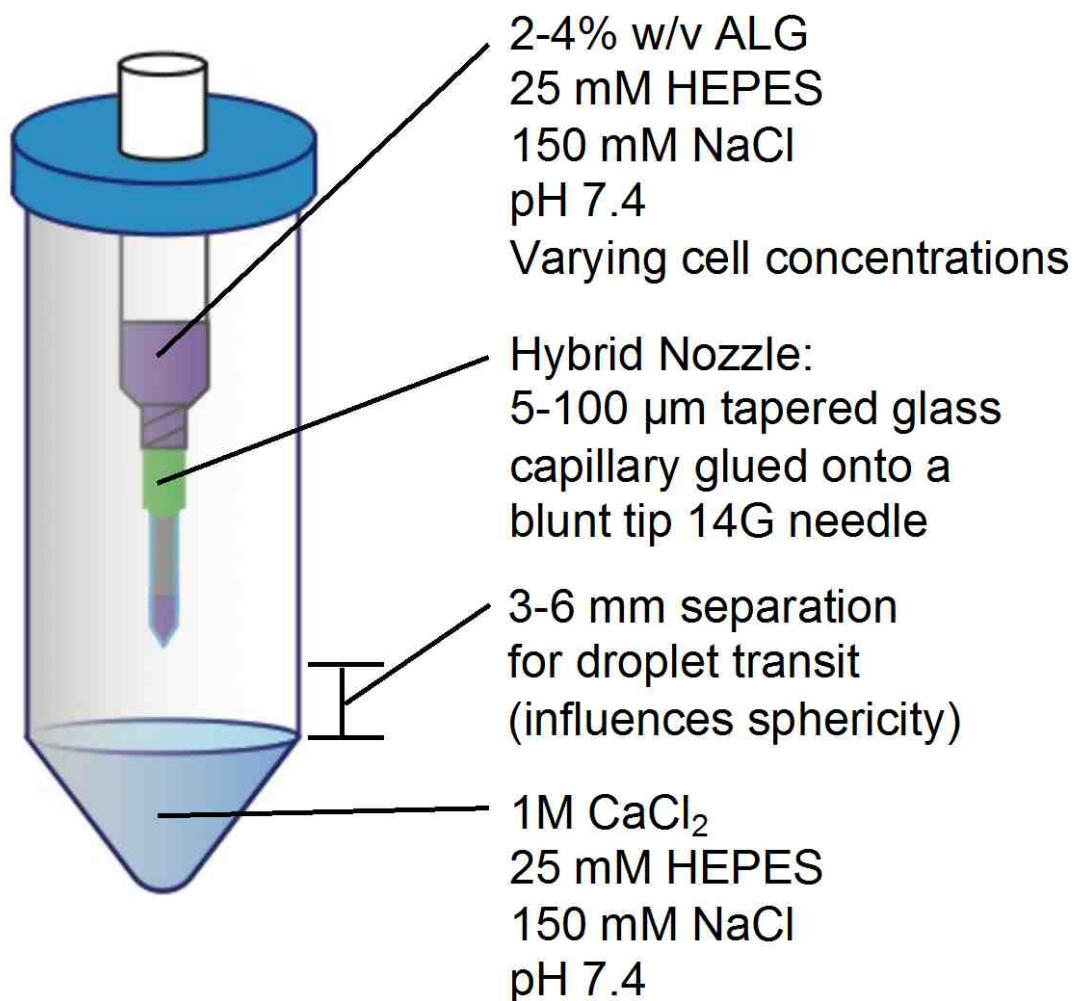
*Droplet generating centrifuge tube assemblies are designed with new hybrid needle/glass capillary nozzles of various combination and diameters to produce controllable and uniform droplets down to sizes not previously observed.*

The droplet generating centrifuge tube assembly design is inspired by previous centrifugal synthesis approaches.<sup>4</sup> The general approach is to produce a centrifuge tube that contains as a lower layer the catch/solidification solution, and an upper layer as a pre-gel solution that will form droplets in air to be captured in the catch solution. Implementation involves using two nesting tube layers (an inner construct for pre-gel/nozzle attachment and a normal outer tube for the droplet catch/solidification solution) assembled for integration into a swinging arm centrifuge. The purpose of the nesting nature of the droplet device assembly is to spatially separate a sodium alginate pre-gel solution in the inner (upper) compartment from a  $\text{CaCl}_2$  crosslinking solution partitioned in the outer (lower) tube until droplet formation in air has occurred. When centrifugal force is applied to the tube assembly, the swing arm of the centrifuge positions the tube such that the central axis of the tube assembly is orthogonal to the rotation axis. The solution in the inner nested tube is then drawn through the inner tube nozzle under the force of artificial gravity induced by the rotation. Droplets are formed that transit in air and then submerge into the 1 M  $\text{CaCl}_2$  catch solution for solidification. The devices are operated in pairs to balance the centrifuge during rotation. One should also

note that the throughput of this system can be enhanced by simply operating multiple paired devices in parallel, limited only by the number of positions available in the centrifuge to hold tube assemblies.

Compared to prior work<sup>4</sup>, one improvement made here is to greatly reduce or adjust the nozzle size of the tube assembly by threading a custom cut glass capillary (pulled to a taper with a Sutter Instrument Co. P-97 glass capillary puller and soldered to a defined diameter using a Narishige Microforge) over a blunt tip 14G needle (Integrated Dispensing Solutions) and applying epoxy to produce an easily attachable hybrid nozzle. Previous work only used commercially available needles as the nozzle component in device assemblies, and the smallest inner diameter needles commercially available are 108  $\mu\text{m}$  (Nordson EFD). With these conditions, the smallest possible 4% ALG droplet diameter is limited to  $\approx 300 \mu\text{m}$ . In general, a mismatch in nozzle diameter to droplet diameter is observed because of the highly viscous nature of the ALG. By fabricating in house glass capillary nozzles with diameters down to 50  $\mu\text{m}$  (depending on the application, diameters down to 5  $\mu\text{m}$  are feasible) and coupling these to blunt tip needles, customized nozzles are easily attached to centrifuge tube assemblies and increase the range of possibilities for nozzle diameter, which governs droplet diameter.

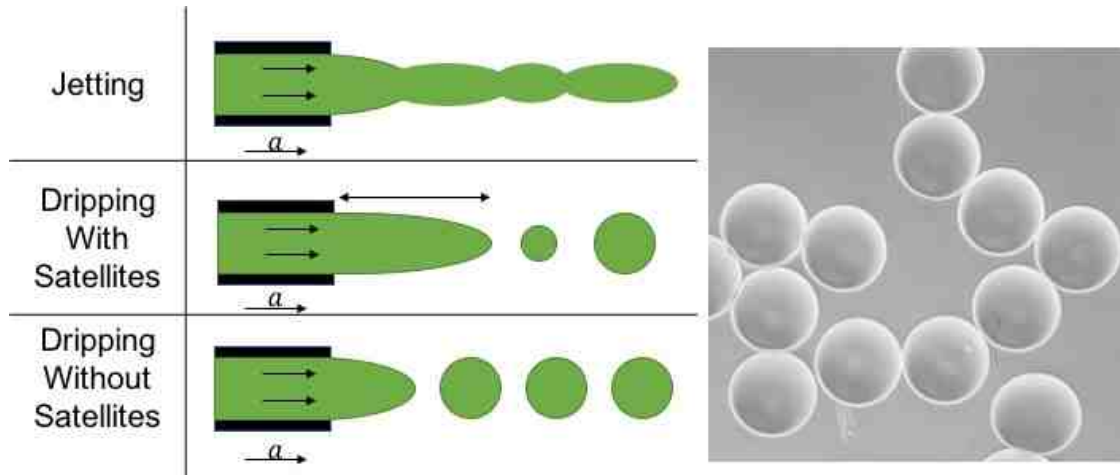
The inner nozzle attachment is built by first using a drill press to make a 15 mm ID hole in the center of the twist cap from a standard 50 mL centrifuge tube. The plunger of a 10 mL Luer-Lok Tip syringe (BD) is removed and the casing is smoothly cut using a Dremel tool to roughly 60 mm length (from needle attachment



**Figure 5.2 Device Schematic.** Diagram of the centrifuge tube assembly showing the design of nesting compartments to partition solutions in the inner tube (sodium alginate) and outer tube (calcium chloride) in order to prevent premature crosslinking before centrifugal synthesis. Additionally, the hybrid nozzle is detailed along with the height parameter that defines the sphericity of the droplets produced. If the distance is too long, the droplets will be oblong and if too short a loss of individual particles is observed.

to top). The inner nesting layer is achieved by inserting the 10 mL syringe into the 15 mm hole of the centrifuge tube cap, Luer-Lok in the downward position, and arranging it to provide the desired height. The distance between the nozzle tip and catch solution is an important parameter that determines the sphericity of the solidified droplets. For example, if 2 mL of droplet precursor solution and 8 mL of crosslinking solution are used (as is the convention for the work detailed herein), then the distance between the catch solution and nozzle tip should generally be between 3-6 mm for spherical droplets. This is measured by marking the catch solution surface in the 50 mL centrifuge tube and attaching a hybrid nozzle to the syringe Luer-Lok tip to estimate the distance between the catch solution surface and the nozzle tip. Once the appropriate height is achieved, a thin layer of hot melt adhesive is applied to permanently set the syringe in the cap (Figure 5.2).

For centrifugal alginate droplet production, recent investigations have modeled and defined how the relationships between device parameters such as the height between nozzle tip and catch solution surface, droplet solution viscosity, and nozzle diameter directly affect the size distribution and shape of the droplets.<sup>4</sup> During centrifugal droplet generation optimization with our new hybrid nozzles, three operational states were defined depending on the centrifugal force applied to the tube assembly (set as revolutions per minute on the centrifuge and flow rate of the inner tube sodium alginate measured by displacement in mL per minute). With hybrid nozzle centrifuge tube assemblies, the most important parameters for producing spherical alginate droplets are the viscosity of the solution, the diameter of the nozzle, and the acceleration of alginate solution out of the nozzle. When



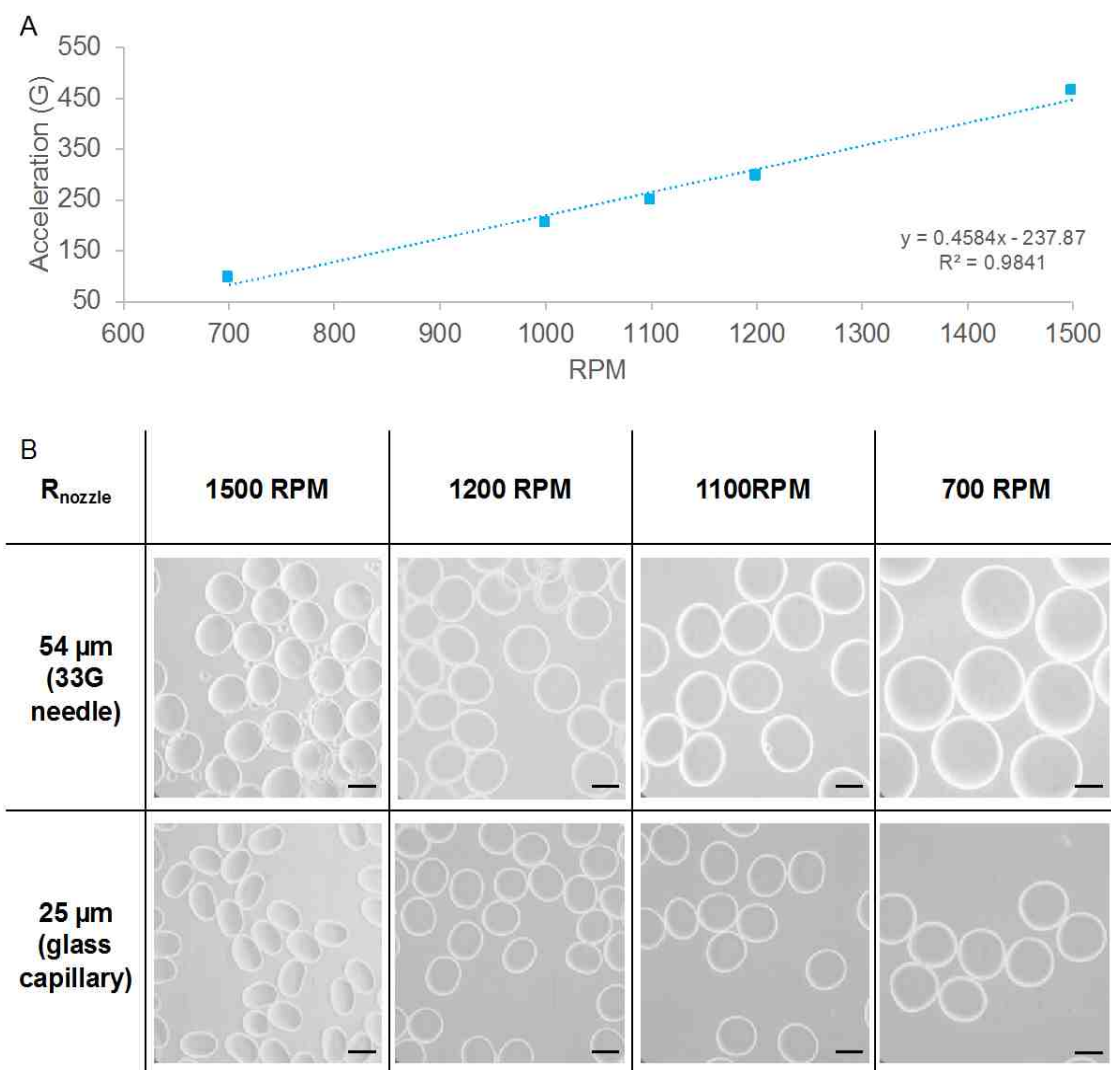
**Figure 5.3 Droplet Generating Flow Regimes.** Diagram showing the three operational states observed in centrifugal droplet generation with a hybrid needle/glass capillary nozzle design. Assuming the height parameter is optimized and the nozzle diameter is constant, if the acceleration is too high or if the solution viscosity is too low the jetting regime will dominate the operation of the device. Likewise, if the acceleration and viscosity are not within a certain range it is possible to create a satellite regime where droplets with a bimodal size distribution are produced (usually with one population being close to the desired diameter and the other being too small). When the parameters are optimized, a range of centrifugal force may be defined for generating and collecting a droplet population with a narrow size distribution and nearly perfect aspect ratio, with the diameter of the droplet being directly correlated to the acceleration of the device is generated and collected.

these parameters are optimized, a range of centrifugal force is established and the revolutions per minute during droplet generation will control the size of the particles collected from the catch solution depending on the solution viscosity. When operating the devices at suboptimal conditions, jetting and satellite regimes are observed where strings of crosslinked alginate or a bimodal droplet size distribution occur, respectively. The image inlay in Figure 5.3 demonstrates the desired monodispersed droplet population.

For simplicity in the discussion below, the centrifugal spin speeds for the centrifuge used to generate droplets (Eppendorf 5810 Centrifuge) are reported in revolutions per minute (RPM), with ramp-up and deceleration times being an accepted experimental error. As shown in Figure 5.4 A, the speeds in RPM can be converted to an approximate acceleration that depends on the radial distance from the center of the rotor to the location of droplet formation within the centrifuge tube assemblies when the swing arm has moved into position under artificial gravity (roughly 19 cm for the Eppendorf 5810). These values are included so that individuals interested in adapting this technology to a different centrifuge model can approximate the acceleration for their own apparatus. Droplet generation is optimized by comparing both a 108  $\mu\text{m}$  diameter needle and a 50  $\mu\text{m}$  diameter hybrid nozzle over a range of centrifuge spin speeds. These studies use sodium alginate solution without cells to determine the parameters best suited for uniform droplet shape and size, which will then be translated to cell encapsulation. All solutions and chemicals used for droplet generation are designed with buffering capacity, osmolarity, and sterility in mind to achieve biocompatible cell culture

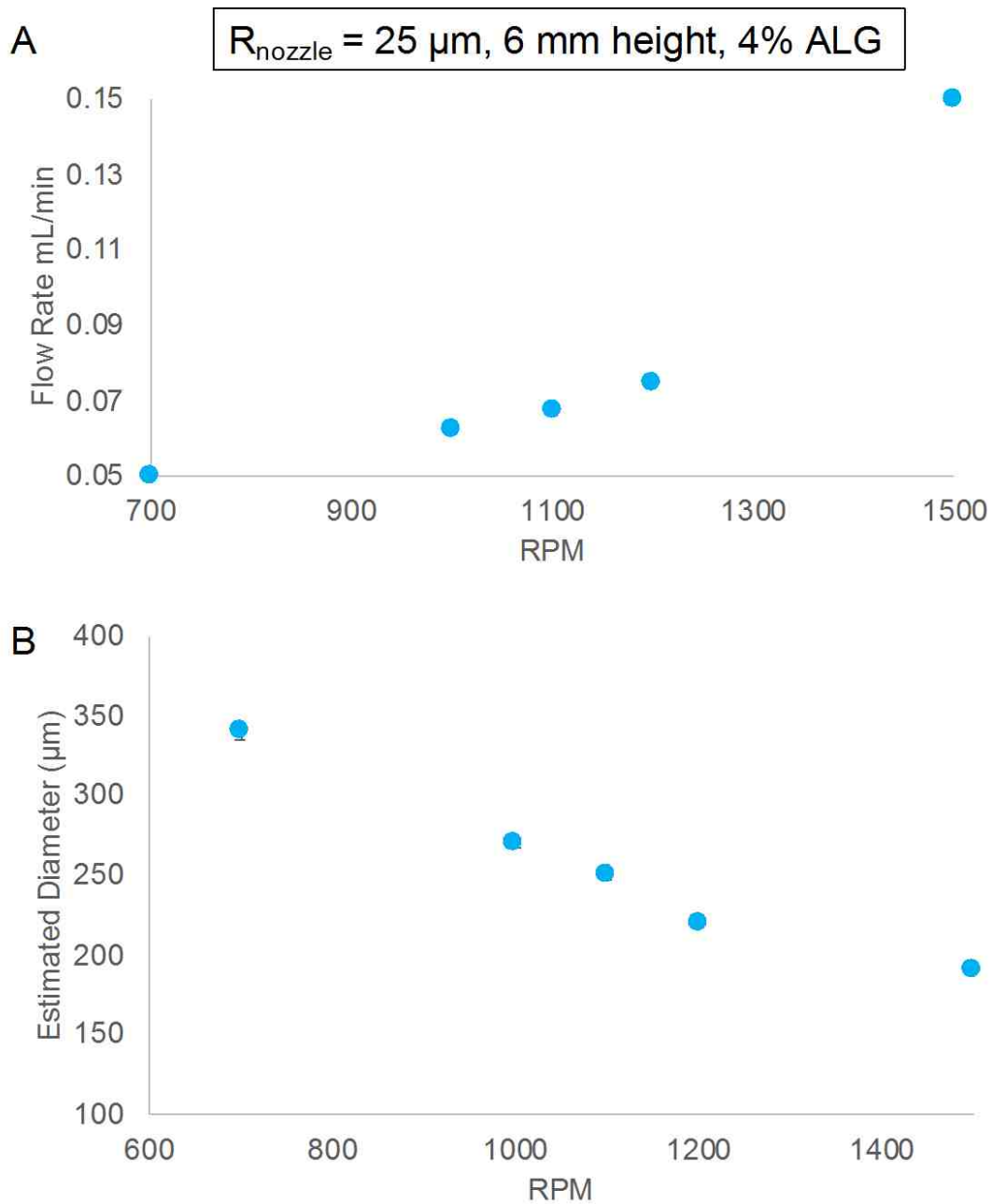
conditions (all reagents from Sigma Aldrich unless otherwise noted). In order to prepare the centrifuge tube assembly pairs for operation, 8 mL of the crosslinking catch solution (1 M CaCl<sub>2</sub>, 25 mM HEPES, 150 mM NaCl, pH 7.4, 0.2 µm sterile filtered using Nalgene APES bottle top vacuum filter apparatus) is pipetted into the 50 mL centrifuge tubes. The nozzles to be used are connected to the Luer-Lok attachment of the 10 mL syringe/screw top arrangements, carefully positioned into the 50 mL tubes, and locked into place by tightly securing the cap to the tube making sure to keep the assemblies upright. Then 2 mL of sodium alginate solution, prepared by dissolving 4% w/v alginic acid sodium salt in physiological buffer (25 mM HEPES, 150 mM NaCl) with vigorous stirring overnight and pH adjustment to 7.4 using a specialized electrode for highly viscous solutions (Orion™ Ross™ Sure-Flow™ pH Electrode with Sure-Flow Junction, Thermo-Fisher), is carefully and slowly pipetted into the syringe inner compartment. The centrifuge tube assemblies are weighed to ensure the centrifuge rotor will be balanced, adjusted as needed by removing fluid if one of the devices in the pair is heavier than its counterpart, and loaded into the centrifuge swing arm compartments for operation.

For the purpose of comparison and validation, a parameter matrix using the smallest gauge needle commercially available (nozzle radius 54 µm) and the new hybrid nozzle (radius 25 µm) design has been established using the centrifuge tube assemblies described above. The devices were operated in pairs across the range of centrifuge RPMs of 700-1500 (Figure 5.4 B) (along with flow rates measured by displacement of the alginate out of the inner compartment as seen



**Figure 5.4 Hybrid Nozzle Characterization.** (A) The approximate acceleration as it depends on RPM with our centrifuge is shown here as a reference for other centrifuges. (B) Microscopy of droplets generated using centrifuge tube assemblies comparing the use of a needle as a nozzle and a smaller diameter hybrid needle/glass capillary nozzle at a range of centrifugal forces. Qualitatively, the hybrid nozzle generates much smaller droplets at all speeds and across this range never transitions into the dripping with satellites regime as is the case for 1500 RPM and the needle. (Scale bars 200  $\mu\text{m}$ )





**Figure 5.5 Hybrid Nozzle Optimization.** (A) Flow rates measured (in triplicate with standard error bars smaller than the point) by displacement of 4% alginate in the device assembly using a 50  $\mu\text{m}$  hybrid nozzle and (B) corresponding geometric mean diameter of particles produced across the range of speeds ( $n = 25$ , standard error bars also smaller than most points).

in Figure 5.5 A), which was established to be the range where droplets with a relatively narrow size distribution are generated. The collected droplets are then imaged using brightfield microscopy and a Nikon camera with Spot Basic microscopy software. The droplet images are analyzed using an ImageJ batch macro to determine the geometric mean diameter of each particle, the aspect ratio, and the average size of the population (at least an  $n=25$  for each size distribution measured). The geometric mean diameter is calculated as the square root of the product of the longest distance (major axis) and the shortest distance (minor axis) across the surface of the particle in an image and is used to determine the geometric droplet diameter (Figure 5.5 B). The aspect ratio is determined by dividing the length of the major axis by that of the minor axis. A value of 1 indicates perfect circularity (sphericity), and the population distribution is determined by the average of the measured geometric mean diameters.

It is observed that as centrifugal acceleration (reported as spin speeds in RPM) increases, the geometric mean diameter of the collected droplets becomes smaller. Although both the needled and the hybrid nozzles operate within the same range of speeds, the droplets generated with the hybrid nozzle have a much smaller geometric mean diameter range and are some of the smallest values reported using centrifugal synthesis. The generation of droplets with a 50  $\mu\text{m}$  hybrid nozzle/centrifuge tube assembly has been well characterized by flow rate measurements and analysis of droplet populations. This droplet generation technology is explored to push the size limit of droplets by fabrication of smaller

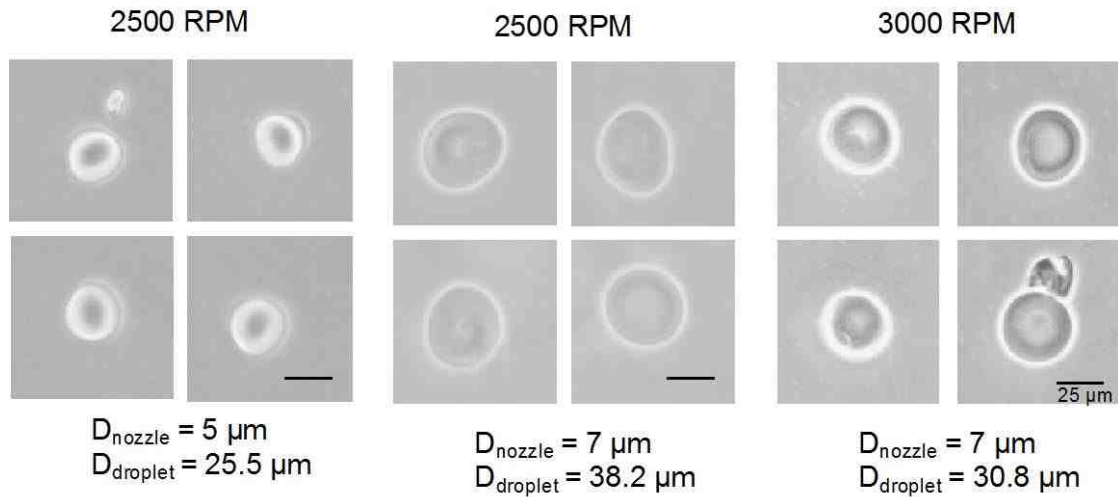
hybrid nozzles and adapted for cell encapsulation as demonstrated in the remainder of Chapter 5.

### 5.3 Cell-Sized Droplets

*Centrifuge tube assemblies with hybrid nozzles are used for the first time to produce super small droplets with sizes on the order of a large cell.*

Large populations of biocompatible droplets with a narrow size distribution and geometric mean diameter on the order of a large cell (25-30  $\mu\text{m}$ ) are desirable for cell-free applications and enzyme immobilization studies. Droplet-based microreactors are being investigated as synthetic compartmentalization platforms to be used for the isolation and stabilization of vesicles of all lipid-derived architectures, for example giant unilamellar vesicles, multilamellar vesicles, multicompartiment vesicles, and phase separated vesicles.<sup>5,6</sup> The main limitation of these artificial cell systems in bottom-up synthetic biology approaches is that the lifetime of the vesicles once formed is roughly 1 hour due to the large osmotic differences that are required to stabilize the phases.<sup>7</sup> Other applications for populations of cell-sized droplets include uses in high-throughput drug screening, biomolecule analysis (proteins, nucleic acids, amino acids, DNA), molecular interactions, and drug delivery investigations all within a 3D biomimetic environment.<sup>8</sup> Until this work using hybrid nozzles with in-house nozzle diameters fabricated down to 5  $\mu\text{m}$  ID, centrifugal droplet generation had yet to be realized as a robust platform for the generation of large, uniform populations of cell-sized droplets that can facilitate studies in the application spaces mentioned above.

The general design of the tube assemblies and hybrid nozzle is consistent with the methods detailed in Section 5.2. The important modifications to note are (1) the glass capillary is pulled with a long taper and soldered to 5  $\mu\text{m}$  and 7  $\mu\text{m}$  diameters to be glued onto the blunt tip needles, and (2) the height parameter (the distance between the solidification solution surface and the tip of the nozzle) is found to be optimized at 3 mm. Experiments using a short-tapered glass capillary, 10  $\mu\text{m}$  diameter nozzles, and heights up to 6 mm produced undesirable particle geometries and are not shown here. Finally, the cell-sized droplets were found to only be generated at higher centrifugal forces moving the highly viscous 4% ALG solution out of a small diameter nozzle requires higher input energy. However, this is not a limitation as most standard swing arm centrifuges can spin up to 4000 RPM, and it was also found that using 3% ALG solutions is an option that still maintains a robust particle sphericity. This brief investigation of using hybrid nozzles with centrifuge tube assemblies is a proof-of-principle study that demonstrates the use of 5 and 7  $\mu\text{m}$  diameter nozzles, 3 mm heights, and speeds of 2500 and 3000 RPM to produce cell-sized droplets that can be used for cell-free systems.



**Figure 5.6 Cell-Sized Droplets.** Microscopy of droplets generated using centrifuge tube assemblies comparing the use of small diameter (5 and 7  $\mu\text{m}$ ) hybrid needle/glass capillary nozzles at two centrifugal forces (2500 and 3000 RPM). Qualitatively, the hybrid nozzle generates small droplets (25-30  $\mu\text{m}$  geometric mean diameter with an  $n = 10$  for each analysis by ImageJ) at speeds attempted thus far and has the potential to be improved with higher speed centrifugal generation. (Scale bars 25  $\mu\text{m}$ )

## 5.4 Cell Encapsulation by Centrifugal Droplet Generation

*Centrifuge tube assemblies using hybrid nozzle designs are used to encapsulate cancer cell lines at low and high cell occupancies to demonstrate the use of this platform for cancer biology applications.*

The cell encapsulation method is necessarily a simple and rigorous protocol in order to produce a biocompatible single cell suspension for droplet generation. Achieving a single cell suspension is important for standardized cell culture conditions as well as for homogeneity in the droplet population, and also helps avoid cell clumping that will cause clogs in the nozzles. In addition, it enables applications discussed in Chapter 6 by, for example, addressing the need for each droplet to have effectively the same numbers of cells when initiating proliferation experiments. Cell processing procedures for encapsulation have been established that use buffers without  $\text{Ca}^{2+}$  to count, wash, and introduce single cell suspensions into ALG pre-gel solution without prematurely crosslinking the gel. Using this protocol, it is possible to control the initial number of cells/droplet starting from low cell numbers up to hundreds of cells/droplet. In addition, cell processing procedures and buffers for recovering and counting encapsulated cells over time from crosslinked droplets have been designed. To achieve sizing of the droplets generated in a population, bright field microscopy imaging and analysis with ImageJ has been implemented. These protocols enable statistically relevant

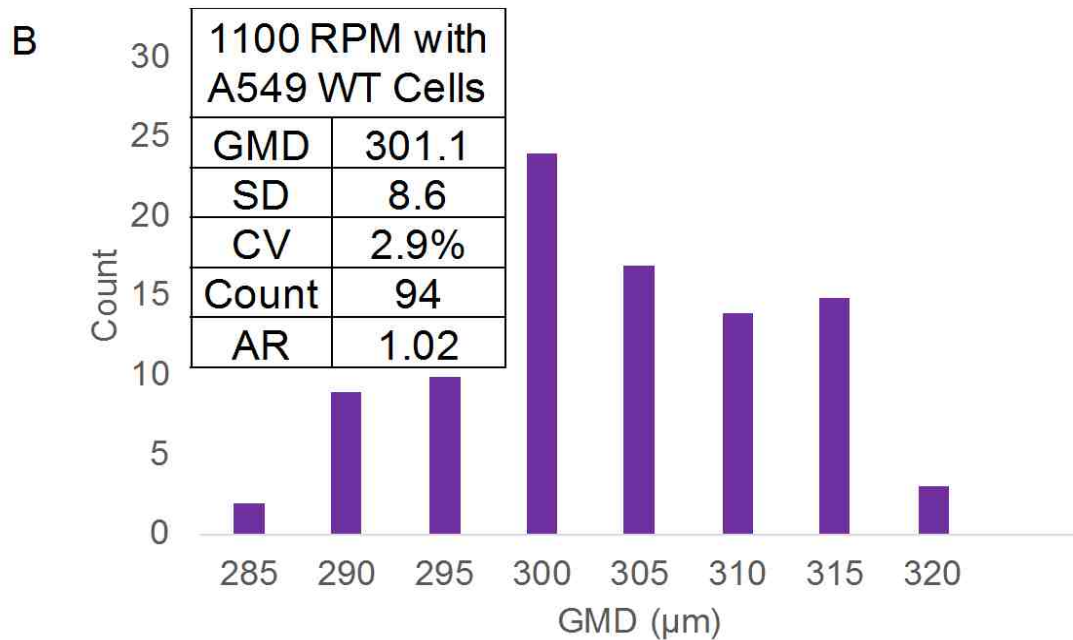
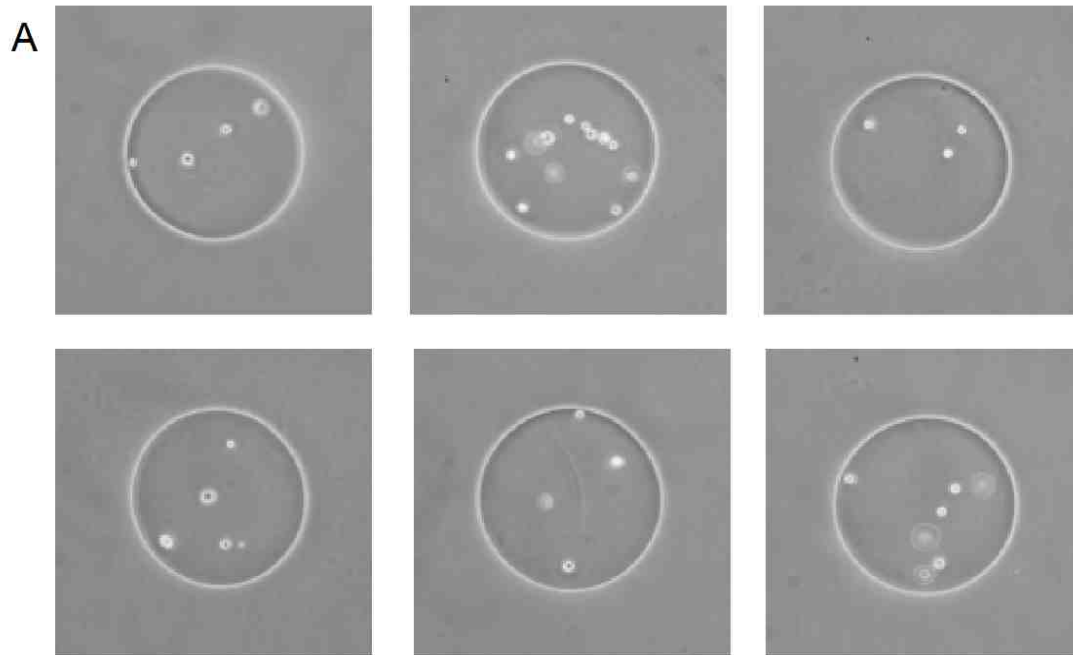
measurement of the average droplet geometric mean diameter generated with encapsulated cells at low and high cell occupancy.

The centrifugal droplet assemblies are prepared as described in Section 5.2. The difference here is that the ALG solution added to the inner compartment of the droplet generating assembly contains a cell suspension. In the low cell occupancy experiments described herein, the human non-small cell lung carcinoma cell lines A549 WT and KO for HIF-1 $\alpha$  are used; and in the high cell occupancy experiments, the human malignant melanoma cell line MEL28 are used. All cell lines are handled using the same conditions (complete Minimal Essential Media with 10% Cosmic Calf Serum and 1% Penicillin and Streptomycin from Hyclone and 37°C, 5% CO<sub>2</sub> in the incubator) and protocols for standard cell transfers or preparation into single cell suspensions (using 0.25% Trypsin with EDTA from Hyclone, referred to as “trypsin”) have been developed. Cells are plated at low density and grown over 5 days on 150 mm dishes to grow up for encapsulation. The dishes are trypsinized with 5 mL of trypsin for 20- 30 minutes at 37°C, 5% CO<sub>2</sub> in the incubator and suspended by adding 5 mL of media to transfer the entire 10 mL suspension per dish into a 50 mL centrifuge tube. A small volume is taken to count the combined cell suspensions and measure the concentration of cells. The cell suspension is pelleted by centrifugation at 2000 RPM for 10 minutes. The supernatant is aspirated and the cell pellet is washed by resuspending into 20-50 mL of a cell encapsulation buffer (1 mM EDTA, 25 mM HEPES, 150 mM NaCl, pH 7.4), depending on the cell concentration to be used, to sequester any calcium ions and prevent the generation of crosslinks when the

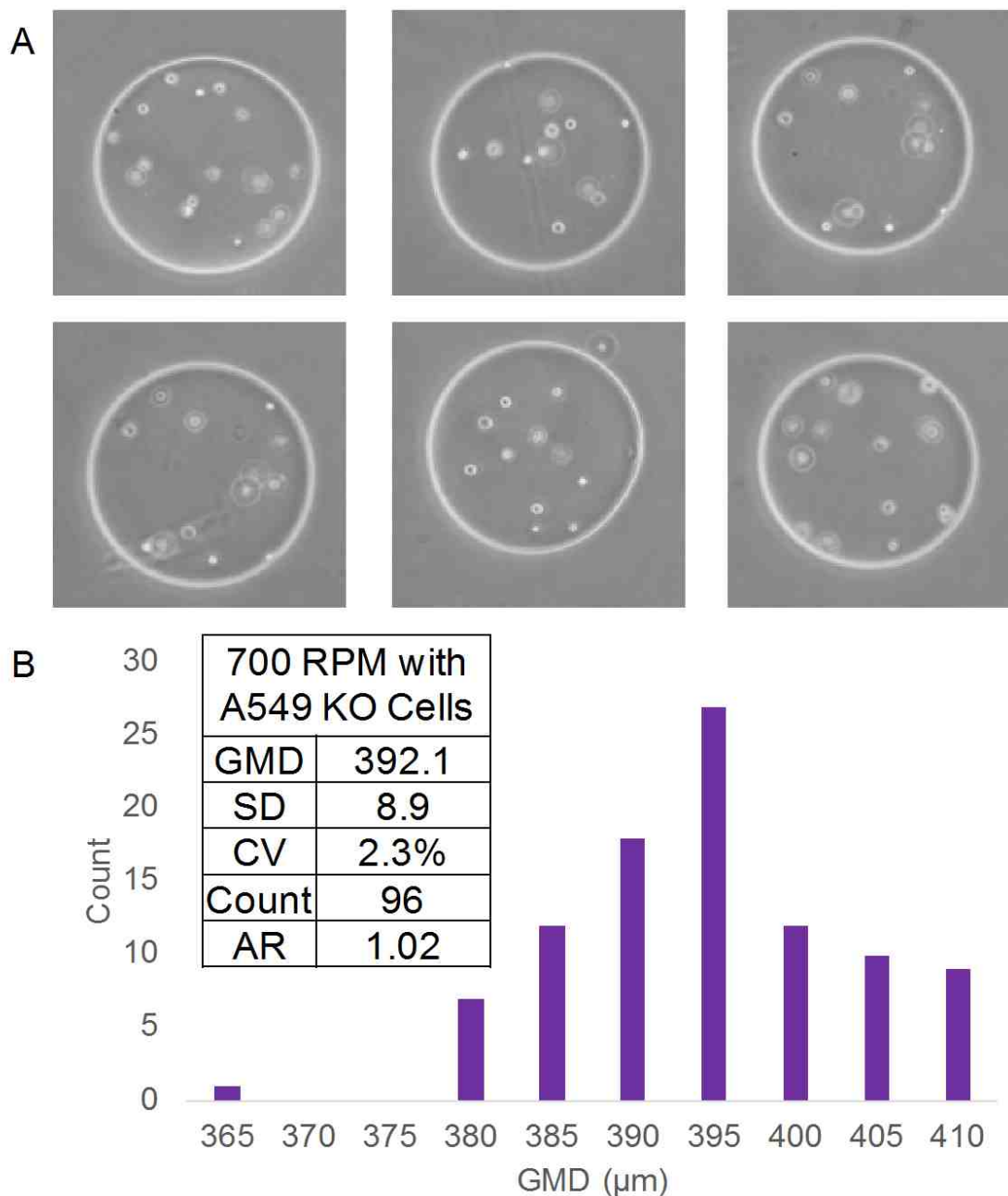


cells are added to the ALG that could cause premature crosslinking. The cell suspension in encapsulation buffer is then centrifuged into a pellet for the second time at 2000 RPM for 10 minutes. The supernatant is aspirated once more, and the cell pellet is resuspended in 100  $\mu$ L of encapsulation buffer with gentle pipetting up and down using a 1000  $\mu$ L pipette tip. 400  $\mu$ L of 4% ALG is added to the 100  $\mu$ L of cells and mixed. This step is necessary as direct resuspension of the cell pellet into 4% ALG produces a suspension high in cell multiplicity (doublets, triplicates and larger cell clumps) because of the viscosity. By resuspending cells into 100  $\mu$ L of buffer (low viscosity) and adding dropwise into the ALG, clumps can be broken up and a single cell suspension is achieved. This is important for uniform distribution of cells in the droplets as well as to prevent clumps from clogging the devices. This 500  $\mu$ L of cells in ALG is then drawn up into an 18G needle/10 mL syringe (BD) and added dropwise to 4.5 mL of 4% ALG while vortexing to produce a 5 mL total volume single cell suspension. The 5 mL cell suspension is passed through a 40  $\mu$ m cell strainer filter mesh to remove any residual debris. Finally, 2 mL of the cell suspension in ALG is added to the inner compartment of centrifuge tube device assembly pairs. This makes the final preparation for device operation.

A549 cells have been encapsulated at low cell density under two different cell concentrations and operating parameter combinations in order to demonstrate cell encapsulation across the range of frequencies in which we observed robust droplet generation without cells. A549 KO and WT cells were each prepared for low cell occupancy encapsulation as described above. Briefly, a cell suspension in ALG of  $4 \times 10^5$  cells/mL is used to produce cell encapsulating droplets using a 70



**Figure 5.7 A549 WT Droplet Distribution.** (A) Microscopy of droplets generated using 70  $\mu\text{m}$  diameter hybrid nozzles in centrifuge tube assemblies operated at 11000 RPM to encapsulate A549 WT cells. (B) Statistical analysis showing the size distribution and other features in the table inlay of the collected cell encapsulating droplets ( $n = 94$ ).



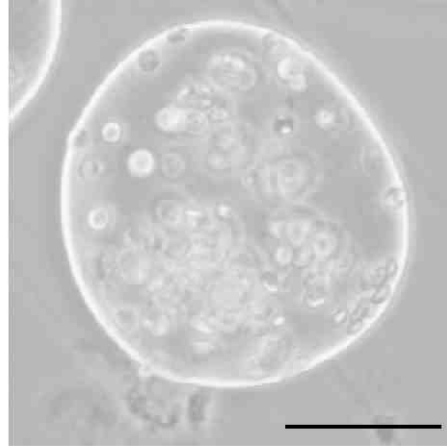
**Figure 5.8 A549 KO Droplet Distribution.** (A) Microscopy of droplets generated using 70  $\mu\text{m}$  diameter hybrid nozzles in centrifuge tube assemblies operated at 700 RPM to encapsulate A549 KO cells. (B) Statistical analysis showing the size distribution and other features in the table inlay of the collected cell encapsulating droplets ( $n = 96$ ).

$\mu\text{m}$  diameter hybrid nozzle and 1100 RPM or 700 RPM for the WT and KO, respectively (Figures 5.7 and 5.8). Because the droplets were generated at different speeds, they were measured to have different geometric mean diameters and a slightly different cell occupancy (WT estimated 5 cells/drop and KO estimated 10 cells/drop), which is itself governed by a Poisson distribution. The aspect ratio of the particles is nearly perfect at 1.02. The coefficient of variation of particle size is 2-3%, which indicates a narrow size distribution. To reduce or eliminate the presence of significant intra-droplet concentration gradients during cell culture, droplet size is an important consideration. Ideally, one might use droplets of  $\approx 200 \mu\text{m}$  diameter or less, and these droplets are larger than this (KO 392.1  $\mu\text{m}$  diameter and WT 301.1  $\mu\text{m}$  diameter). However, they are still within a size range that is compatible with matching diffusional transport to metabolic consumption, and the generation of substantial intra-droplet gradients is not expected (especially for low cell occupancy numbers). Finally, these initial proof-of-principle cell encapsulating droplet populations are generated using the lower end of the centrifugal force range that was observed to produce monodispersed droplet populations, so further investigation into low cell occupancy encapsulations may produce even smaller particles.

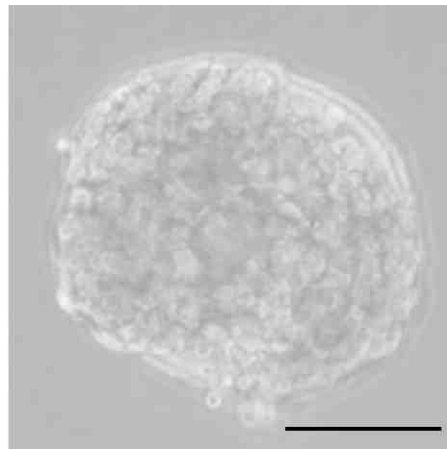
High cell occupancy experiments are designed to produce droplets with essentially the same number of cells as an early stage multicellular tumor spheroid, forming an instant spheroid. The formation of scaffold-supported instant spheroids is an application not yet realized in the field that could have major implications for studying the chemical microenvironment, large particle flow cytometry, high-

throughput drug discovery, and tissue engineering. The same device construction and cell preparations are used as described in Section 5.2 and 5.4 with the main distinction here being the cells for encapsulation were the MEL28 cell line and the concentration to be encapsulated was largely scaled up using multiple 150 mm tissue treated polystyrene dishes. A range of cell concentrations was investigated to determine the maximum number of cells in 4% ALG able to flow through a 50  $\mu\text{m}$  hybrid nozzle/centrifuge tube assembly. For high cell occupancy, the cell distribution per droplet follows a near Gaussian distribution (large number limit of Poisson distribution), so the encapsulated concentration and thus the cells/droplet is a measure of the average number of cells expected to occupy a droplet. High cell occupancies were achieved for droplets generated with a 50  $\mu\text{m}$  diameter nozzle at 1250 RPM producing  $\sim 230$   $\mu\text{m}$  diameter droplet populations for each of the three successfully attempted encapsulations ( $n = 25$ , coefficient of variation of 2.6%) (Figure 5.9), and no droplets for the upper limit due to nozzle clogging and a high multiplicity (cell clumping even after filtering through a 40  $\mu\text{m}$  cell strainer) in the cell suspension. Specifically, four cell concentrations were attempted for encapsulation: (1)  $1.6 \times 10^7$  cells/mL (100 cells/droplet); (2)  $3 \times 10^7$  cells/mL (200 cells/droplet); (3)  $6 \times 10^7$  cells/mL (400 cells/droplet); and (4)  $8 \times 10^7$  cells/mL (500 cells/droplet), with the highest causing nozzle clogging. For the purpose of this Chapter, the data displayed is exclusively from microscopy of instant spheroid populations immediately after encapsulation. Additional studies and their results are presented in Chapter 6.

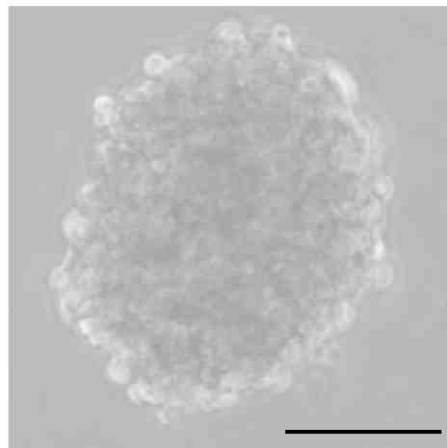
~100 Cells



~200 Cells



~400 Cells



**Figure 5.9 Instant Spheroid Formation.** Microscopy of scaffold supported instant spheroid formation using a 50  $\mu\text{m}$  diameter hybrid nozzle/centrifuge tube assembly operated at 1250 RPM. (Scale bar is 200  $\mu\text{m}$ ).

## 5.5 Discussion and Future Directions

The improved method for droplet-based 3D cell encapsulation by centrifugal droplet generation demonstrates an alternative technology that addresses the limitations of microfluidic and droplet generation in-air platforms. A single centrifuge tube assembly with hybrid nozzle has a moderate throughput on order of 1000 droplets/second depending on the operating parameters, which in itself is a significant improvement to microfluidics throughputs that are on order of 10 droplets/second. As mentioned previously, this moderate throughput in centrifugal synthesis can enter the high-throughput regime by operating up to 16 centrifuge tube assemblies in parallel (depending on the centrifuge). The centrifuge tube assemblies, in a way, are to be included in the droplet generation in-air category as the flow out of the hybrid nozzle and droplet formation under artificial gravity occurs in an air gap that is an optimized parameter (3-6 mm height). Unlike droplet generation in-air which typically uses a stirring or mixing droplet collection mechanism with shear forces, the droplet collection in centrifugal synthesis is not subjected to shear forces and therefore produces nearly perfect spheres (also dependent on solution viscosity). The adaptation of this technology for cell encapsulation requires protocol development and optimization (as described in Chapter 6) however all studies are designed and constructed with readily available materials that most biomedical research labs would have in house. Therefore, the implementation of centrifugal droplet generating technologies into labs interested in using 3D cell cultures to investigate cancer research questions is feasible.

## 5.6 List of References

- (1) Leong, J.-Y.; Lam, W.-H.; Ho, K.-W.; Voo, W.-P.; Lee, M. F.-X.; Lim, H.-P.; Lim, S.-L.; Tey, B.-T.; Poncelet, D.; Chan, E.-S. Advances in Fabricating Spherical Alginate Hydrogels with Controlled Particle Designs by Ionotropic Gelation as Encapsulation Systems. *Particuology* **2016**, *24*, 44–60.
- (2) Sugiura, S.; Oda, T.; Izumida, Y.; Aoyagi, Y.; Satake, M.; Ochiai, A.; Ohkohchi, N.; Nakajima, M. Size Control of Calcium Alginate Beads Containing Living Cells Using Micro-Nozzle Array. *Biomaterials* **2005**, *26* (16), 3327–3331.
- (3) Liu, K.; Ding, H.-J.; Lij, J.; Chen, Y.; Zhao, X.-Z. Shape Controlled Production of Biodegradable Calcium Alginate Gel Microparticles Using a Novel Microfluidic Device. *Langmuir* 9453–9457.
- (4) Eral, H. B.; Safai, E. R.; Keshavarz, B.; Kim, J. J.; Lee, J.; Doyle, P. S. Governing Principles of Alginate Microparticle Synthesis with Centrifugal Forces. *Langmuir* **2016**, *32* (28), 7198–7209.
- (5) Nuti, N.; Verboket, P. E.; Dittrich, P. S. Multivesicular Droplets: a Cell Model System to Study Compartmentalised Biochemical Reactions. *Lab Chip* **2017**, *17* (18), 3112–3119.
- (6) Weiss, M.; Frohnmayer, J. P.; Benk, L. T.; Haller, B.; Janiesch, J.-W.; Heitkamp, T.; Börsch, M.; Lira, R. B.; Dimova, R.; Lipowsky, R.; Bodenschatz, E.; Baret, J.-C.; Vidakovic-Koch, T.; Sundmacher, K.; Platzman, I.; Spatz, J. P. Sequential Bottom-Up Assembly of Mechanically Stabilized Synthetic Cells by Microfluidics. *Nat Mater* **2017**, *17* (1), 89–96.



- (7) Trantidou, T.; Friddin, M.; Elani, Y.; Brooks, N. J.; Law, R. V.; Seddon, J. M.; Ces, O. Engineering Compartmentalized Biomimetic Micro- and Nanocontainers. *ACS Nano* **2017**, *11* (7), 6549–6565.
- (8) Šalić, A.; Tušek, A.; Zelić, B. Application of Microreactors in Medicine and Biomedicine. *Journal of Applied Biomedicine* **2012**, *10* (3), 137–153.

## **Chapter 6**

### **Droplet-based Cell Encapsulation in Cancer Research**

## 6.1 Realistic and Standardized Approaches for Cancer Research

*The disparity in translation observed between in vitro (2D and 3D model systems), preclinical trials (animal models) and the results observed in clinical trials is attributed, in part, to the unrealistic synthetic systems that are the current standard in cancer research approaches.*

In cancer research, treatments have been discovered that enable a drug compound to be directed to a specific type of cell. Often, these approaches are developed by using model cell-line screening processes or in vivo xenograft models that identify unique genetic biomarkers (usually because of a single mutation).<sup>1</sup> However, these models have poor clinical translation because of a systematic inability to mimic key pathophysiological features. For example, 2D tissue culture conditions are entirely unrealistic in that tissue culture media (concentrations of nutrients such as glucose, glutamine, and other essential amino acids)<sup>2,3</sup> as well as incubator conditions (oxygen levels in particular) are designed to sustain mammalian cells on a dish rather than to mimic the physiologically restrictive conditions of an in vivo primary tumor. In addition, 2D cultures lack cellular, biochemical, and metabolic heterogeneity as well as the complexity of a 3D tissue microenvironment<sup>4</sup>, which directly influences the translatability of in vitro drug screening. Xenograft models suffer from the limitations of the biology of the mouse itself. In comparison to the human systems it is designed to mimic, the mouse has a higher metabolic rate, is inbred, has a short lifespan, is reared in

sterilized environments, and in immunodeficient mice, transplantable tumors grow to treatment size over weeks (not years as is typical in humans).<sup>5</sup> In comparison to 2D cultures, xenograft models lack parametric control for mechanism of action investigations, and in many cases the animal system is actually too complex for meaningful controls. In addition, the use of monogenic human tumor cell lines in xenograft models is lacking the genomic instability of a primary cancer and is one of the main reasons why xenotransplantation data fails to translate to human clinical results.<sup>6</sup> Although recapitulating all of the pathophysiological aspects of an in vivo tumor may never be fully realistic, there is a need to define a new paradigm in tissue culture practices in order to implement new assay formats that mimic more of the essential aspects of heterogeneity in human tumors.

The multicellular tumor spheroid (MTS) model is a 3D in vitro cell culture system containing growth kinetics, cellular heterogeneity, nutrient and waste gradients, hypoxia, acidosis, drug penetration, drug response/resistance, and metabolic interactions mimicking that of an in vivo tumorigenic tissue.<sup>7,8</sup> This imitation of key pathophysiological conditions makes 3D cell culture an improvement when compared to overly simplistic 2D tissue culture or overly complex xenograft models. In fact, it is common opinion that intelligently designed 3D culture systems will bridge the gap between 2D and animal models.<sup>9</sup> However, there are practical drawbacks currently preventing 3D model systems from being widely implemented between standard 2D cell culture and xenograft experimental model systems. Conventional aggregation-based (or scaffold-free) spheroid formation methods are limited in that the resulting MTSs have a polydisperse

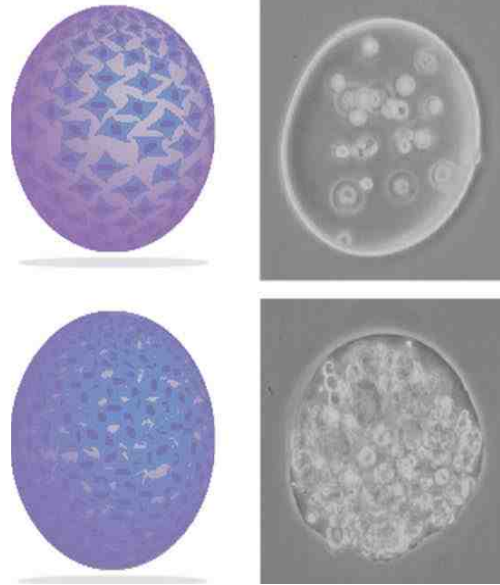
distribution, are low yield because of multiple factors (size selection to obtain a population with the same sized spheroids, number of wells on a plate to form spheroids etc.), are characterized by an inability to control cell ratios in co-culture populations, and have a marked lack of standardized assays for evaluation (proliferation tracking, viability, correlation to local biochemical microenvironments etc.). Cell encapsulation by droplet generation to produce MTS templates (scaffold-based using biomaterials) has been attempted using both in-air and microfluidic platforms<sup>10-12</sup>, but generally falls short in terms of overall cost, simplicity of device fabrication, high throughput operation, monodispersity, biocompatibility, and recovery of cells for downstream assays.

The results presented in Chapters 4 and 5 have demonstrated droplet generation with biocompatible chemistries by microfluidic (Chapter 4) or centrifugal (Chapter 5) synthesis methods to produce uniform cell encapsulating droplets. The studies shown in Chapter 4 specifically validated a qualitative approach to cell encapsulation in droplets and growth over 9 days using spinner flask bioreactor culture and verified that the method of encapsulation was not cytotoxic using a LIVE/DEAD flow cytometric assay. These validation studies for 3D cell culture are a good step in progress towards developing standardized evaluation methods. However, as previously discussed, the microfluidics approach to cell encapsulation is still technologically limited in certain aspects, especially throughput. In contrast, the results in Chapter 5 demonstrate the use of centrifugal generation methods to produce droplets with encapsulated cells in a relatively high throughput manner and with excellent reproducibility. Therefore, in this Chapter centrifugal droplet

generation is used to begin the process of demonstrating (1) the formation of spherical constructs for cell proliferation tracking with the goal being comparison to results observed in 2D monolayer cultures; (2) the generation and culture over time of scaffold-supported spheroids and instant MTSs (iMTS); and (3) the culturing of cells in encapsulating droplets in altered chemical environments (Figure 6.1). The work here uses mouse and human cancer cell lines with a wildtype +HIF-1 $\alpha$  phenotype (WT) and knockout -HIF-1 $\alpha$  phenotype (KO), HKO3-TR and A549 respectively, as well as human MEL28. The use of these cell lines is relevant to the biomedical hypothesis posed in Chapter 1 so that discussion of the methods in progress are ultimately tied to a significant question concerning the interaction of pH, oxygen, and HIF-1 $\alpha$ .

**Bioassay Applications:**

1. Cell proliferation tracking 2D vs 3D
2. Culture into spheroids over time/  
Instant Spheroids
3. Controlled culture conditions for  
extreme environments



**Figure 6.1 Droplet-based Bioassay Applications.** Summary of the approaches in development for the standardization of evaluation methods used to measure proliferation of droplet encapsulated cells, culturing of scaffold supported templates for spheroid formation, and the use of cell encapsulating droplets in altered environment experimental designs.

## 6.2 Adapting 2D Growth Assays to 3D Cell Culture

*New methods are needed to measure the proliferation of cells encapsulated in droplets and to improve 3D cell culture evaluation methods to achieve more realistic measurements of cell growth.*

The doubling time of a cell culture is the fundamental measure of the period of time it takes for a cell to undergo one cell cycle, resulting in the replication of DNA and cell division to produce two new daughter cells. The quantity is used in cancer research to describe the average growth rate of a cancer cell population over time in vitro. However, in 3D cell cultures, the situation is more complex. A length vs width method is used to measure the geometric mean diameter of multicellular spheroids by simply using a microscope reticle to measure a population of spheroids over time. This reports the growth of a spheroid population<sup>13</sup>, but does not directly measure the discrete growth of cells within the spheroid, does not take into account cell death by either apoptosis or necrosis, and there is currently no measurement techniques to analyze biochemical gradient information. In preclinical and clinical studies, the volume of a tumor oftentimes provides qualitative insight to the stage and malignant potential of the tumor as well as treatment efficacy when the tumor size is observed to shrink.<sup>14</sup> Depending on the location of the tumor in vivo, measurement of the tumor can be achieved in situ by using calipers to take the length versus width and calculate the tumor volume as an ellipsoid, which provides a measure similar to the multicellular tumor



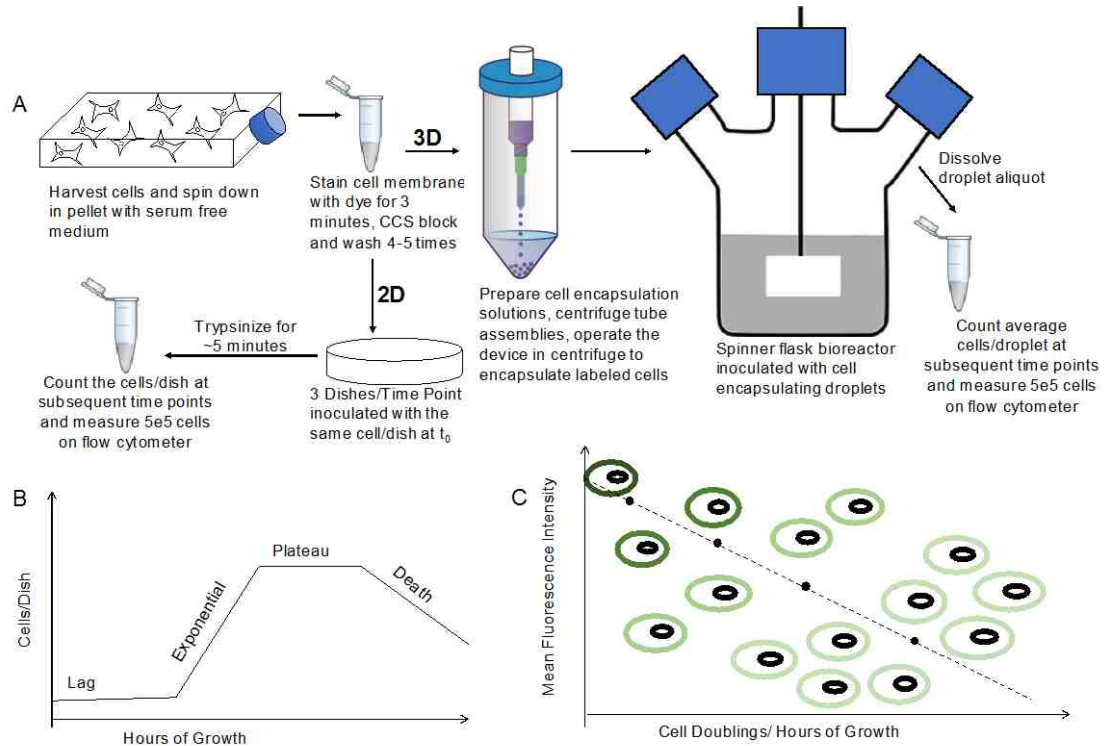
spheroid but, again, is not a discrete measure of the proliferation rate of the cells. Although non-invasive imaging is the gold standard for measurement of tumor volume in vivo<sup>15</sup>, it is expensive and oftentimes logistically unrealistic to apply these techniques to the routine measurements of in vitro 3D cell cultures. It is therefore desirable to develop quantitative proliferation measurement techniques that are inspired by the inexpensive and in-house nature of standard 2D cell culture methodologies but that are adapted to handle the increased complexity of sample processing to measure the growth of cells within a droplet scaffolding biomaterial.

The conventional method for measuring the doubling time of a 2D monolayer cell culture is by counting cells over time. However, recently, a class of membrane-intercalating fluorescent reporter molecules have also been used to measure the doubling time of cells grown in 2D cell culture.<sup>16</sup> These fluorescent molecules have a lipophilic group attached to the fluorophore and insert into the lipid membrane of cells at an initial high concentration and thus intensity when measured by flow cytometry. When the cells divide, the fluorescence intensity per cell reduces to half of the initial value, and therefore the fluorescence dilution by half is a measure of the doubling time of the stained cell population. This method of measuring fluorescence dilution by flow cytometry is useful in that cells in a coculture can be stained with different colored fluorophores and be differentiated from one another.

In order to benchmark our ultimate transition of these methods to 3D cultures, an initial detailed study is performed using these combined methods of standard cell counting and fluorescence dilution to measure the doubling times of

the HKO3 WT, HKO3 KO, A549 WT, and A549 KO cells in 2D mono- and co-cultures. The standard cell counting growth curve analysis is combined with the fluorescence dilution assay for these experiments to have a method for differentiating the WT cells from KO cells in a coculture. The growth curves and fluorescence dilution experiments are initiated by culturing enough cells (using the cell culture protocols and materials detailed in Chapters 4 and 5) to yield  $2 \times 10^7$  cells for staining with either green reporter molecules, known as PKH 67, or red reporter molecules, known as CellVue Claret Far Red (SigmaAldrich, all staining protocols are followed as published in the technical bulletin). To establish the convention, the groups for both the HKO3 and A549 cells are consistent and as follows: (1) WT monoculture labeled green with PKH67; (2) KO monoculture labeled red with CellVue Claret Far Red; and (3) 50% WT green and 50% KO red mixed evenly to produce the coculture.

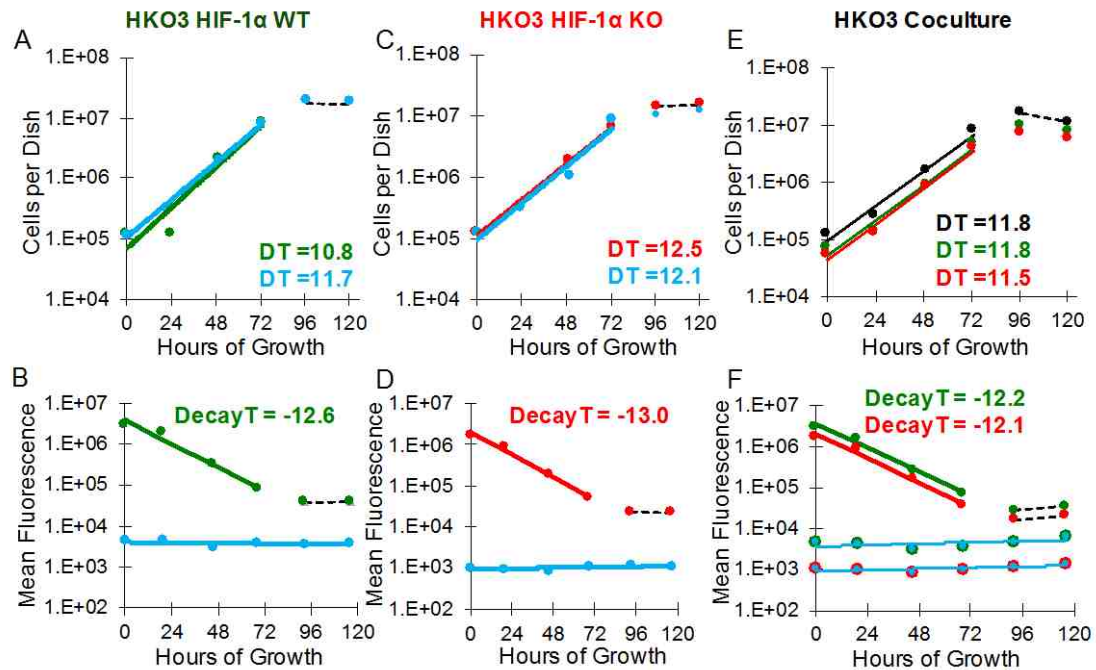
The actual cultures are initiated by inoculating up to 30 tissue culture treated dishes (60 mm diameter) with the same lower cell concentration to establish the cell concentration per dish at  $t_0$  for each of the WT, KO and 50WT/50KO groups using both HKO3 and A549. The cells in the dishes are grown in standard culture conditions and sampled in triplicate by trypsinization to obtain a cell suspension, counted using a Z1 Coulter Counter at determined time points for the duration of the experiment (5 days HKO3 and 10 days A549) to measure the number of cells per dish, as well as measured by flow cytometry using an Accuri C6 Flow Cytometer to obtain the mean fluorescence intensity over time (methods depicted in Figure 6.2 A and expected outcomes for growth curve in Figure 6.2 B as well as



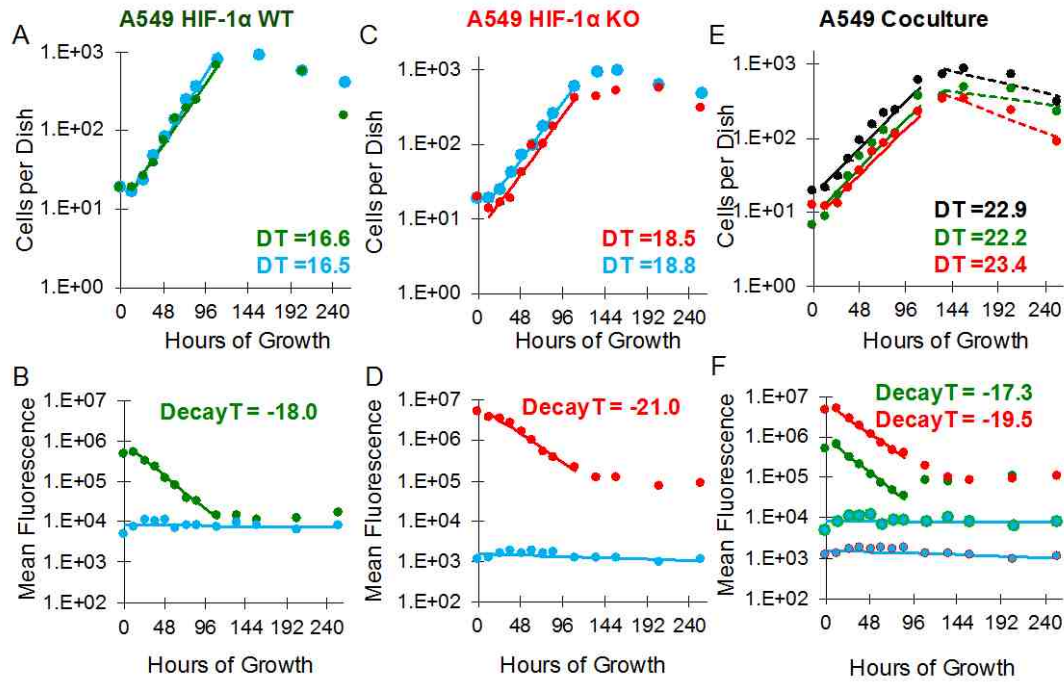
**Figure 6.2 Growth Assay Methodologies.** Summary of the growth and fluorescence dilution protocols. Following the 2D arrows shows the procedure for using the established protocols to track mono- and co-cultured cell proliferation in monolayers. Following the 3D workflow arrows details the general protocol for adapting the method to 3D cell culture using droplet encapsulated cell populations (A). An example of a typical growth curve is depicted in (B) with the different phases in growth. The fluorescence dilution curve is depicted in (C) showing the decrease in the fluorescence intensity signal per cell over time as the cell population exponentially increases.

fluorescence dilution curve in Figure 6.2 C). The data is collected and plotted as growth curves by number of cells per dish over time and as fluorescence dilution curves by the mean fluorescence intensity value per cell measured over time. For completeness, each growth and fluorescence dilution curve is executed in parallel with control groups that are unstained but still follow the convention set using each cell line. Figures 6.3 and 6.4 show the HKO3 and A549 WT, KO and Coculture experiments respectively, with the growth curves on the top row, the fluorescence dilution curves on the bottom row, and each point is an averaged measurement from 3 samples with error bars that in most cases are smaller than the point itself. Each plot has a curve in green for WT, red for KO, and blue for the unstained control.

Although the growth curve coculture (Figure 6.3 E and 6.4 E) should only have one curve because the cells cannot be differentiated by simple counting, it is possible to use the flow cytometry data to determine the percentage of each cell type in the coculture and plot the resulting values as a growth curve. Specifically, the coculture is counted over time as *cells/dish* with no distinction between the red and green cells by the cell counter (black line). The coculture population is subsequently measured by flow cytometry where the mean fluorescence intensity is measured in two channels for the two colors of dye used with each cell type over time. In analysis, a gate is set around the population of cells in each green and red channel that provides the *percentage of cells* of that relative color within the total population. The *cells/dish* value is then multiplied by the *percentage* of either green or red cells and this value indicates the number of cells in the dish that are either



**Figure 6.3 HKO3 2D Growth Assay Results.** Growth and fluorescence dilution assay of HKO3 WT (green), KO (red) and Cocultures. All time points are done in triplicate and error bars are smaller than the point in all cases. The doubling and decay times in hours for mono and cocultures are indicated as inlays for the growth curves in A, C, and E and fluorescence dilution curves in B, D, and F. The blue lines indicate the measurement of unstained control groups, which are a measure of autofluorescence in the fluorescence dilution curves.



**Figure 6.4 A549 2D Growth Assay Results.** Growth and fluorescence dilution assay of A549 WT (green), KO (red) and Cocultures. All time points are done in triplicate and error bars are smaller than the point in all cases. The doubling and decay times in hours for mono and cocultures are indicated as inlays for the growth curves in A, C, and E and fluorescence dilution curves in B, D, and F. The blue lines indicate the measurement of unstained control groups, which are a measure of autofluorescence in the fluorescence dilution curves.

green or red. These values are then plotted as green and red curves on the coculture growth curves.

The doubling times and fluorescence decay times in hours are reported as inlays on their respective plots. In some instances, the growth curves demonstrate exponential growth and a plateau phase (Figure 6.3 A, C and E) whereas in other instances there is a faster transition to the cell death phase (Figure 6.4 A, C and E). In the fluorescence dilution curves, the length of time that cell division can be monitored is limited by the autofluorescence of the cell line. For example, there is an order of magnitude difference between the fluorescence intensity of the stained populations in comparison to the unstained control groups in Figure 6.3 B, D and F even after the plateau phase is reached. In contrast, Figure 6.4 B demonstrates a case where the fluorescence dilution signal intensity eventually decays to the same level of the autofluorescence of the unstained cells, and so time points past that level are no longer useful in determining the doubling (decay) time. To summarize, each cell line doubling time was calculated for the instances of cells grown in both mono and co-cultures.

Although the cells were grown in 2D monolayer cultures in culture conditions designed to support cell growth, the methods described for culturing and measuring cell growth in mono- and co-culture above demonstrate a robust and validated approach. Similar methodology is now needed to implement 3D cell culture into standard lab practices. The remainder of this section focuses on the development and proofs of principle of such methodology in order to take a step

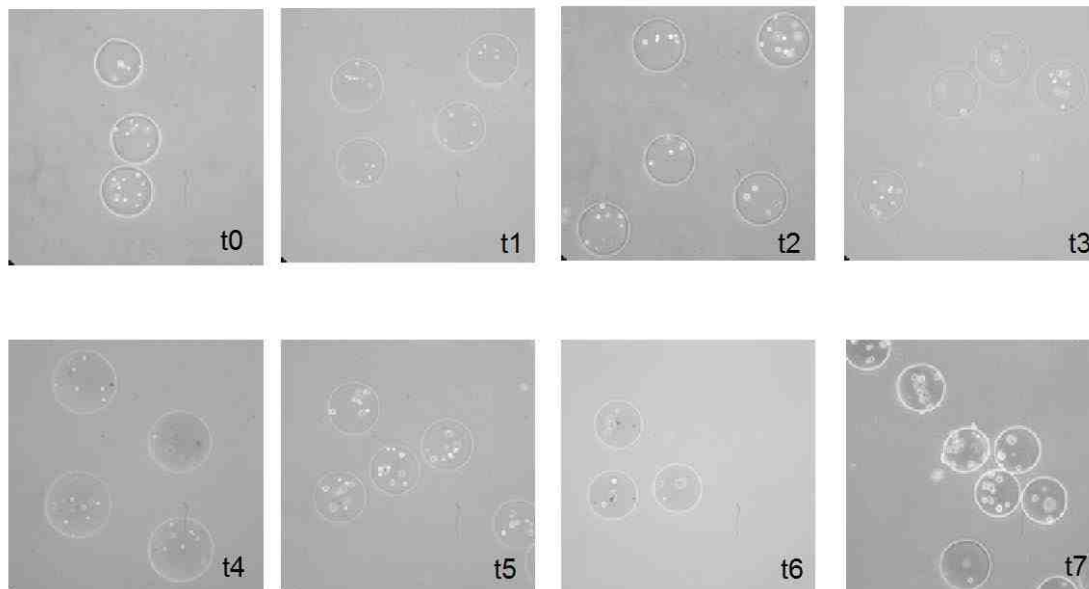
towards using cell encapsulation in droplets as a more robust method for measuring cell growth.

Initially, unstained A549 WT and KO cells were encapsulated at low cell occupancy in droplets using 70  $\mu\text{m}$  diameter hybrid nozzles and two different centrifugal forces (1100 RPM for WT, and 700 RPM for KO) as described in Chapter 5, to produce a proof-of-principle experiment for a 3D growth curve. The droplets collected in the catch were washed using physiological buffer (25 mM HEPES, 150 mM NaCl, pH 7.4, SigmaAldrich) and then pipetted into a 125 mL spinner flask bioreactor (Corning) containing 125 mL of complete Minimal Essential Media (10% Cosmic Calf Serum, 1% Penicillin/Streptomycin, Hyclone) with an added 25 mM HEPES, pH adjustment to 7.4, and 5% CO<sub>2</sub> gas backfilled into the head space to enhance the buffering capacity of the culture conditions for the experiment. The cell encapsulating droplets were then cultured in the spinner flask on a low speed magnetic stir plate (VWR) in a warm room at 37°C for 7 days with daily sampling for observation using brightfield microscopy and media changes every 24 hours (Figures 6.5 and 6.6). For a media change, briefly, the spinner flasks are removed from the stir plate and droplets settle to the bottom of the flask over ~20 minutes. The spent media is aspirated, fresh temperature-equilibrated medium is replaced up to 125 mL in the flask, and the flask is placed back into suspension culture conditions in the warm room. The resulting data presented in Figures 6.5 and 6.6 is at this point primarily qualitative and a demonstration that over 7 days in culture, the droplets are acceptably stable and the cells show some proliferation at later time points (especially with the WT). For

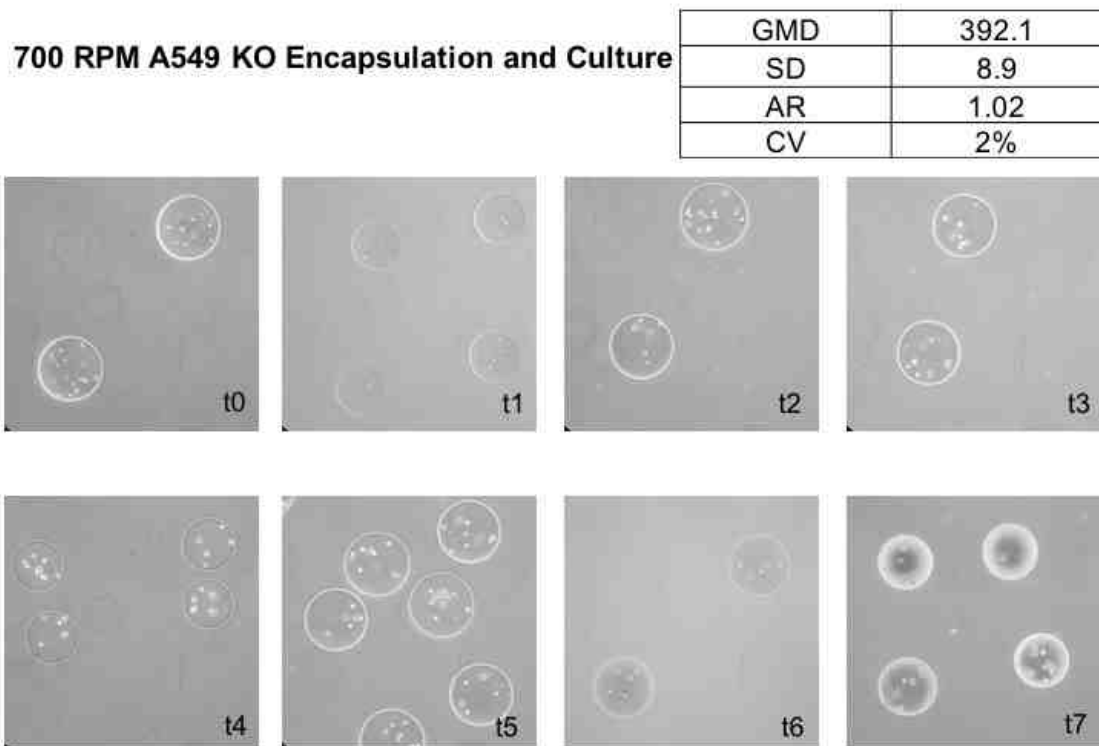


### 1100 RPM WT Encapsulation and Culture

GMD	301.1
SD	8.6
AR	1.02
CV	3%



**Figure 6.5 A549 WT Qualitative 3D Growth Assay.** Qualitative growth curve using microscopy of A549 WT cell encapsulating droplets generated by centrifugal droplet synthesis from a 7-day growth experiment to observe droplet stability and cell growth over time. The population is analyzed using ImageJ to measure the geometric mean diameter, standard deviation, aspect ratio, and coefficient of variation of the culture.

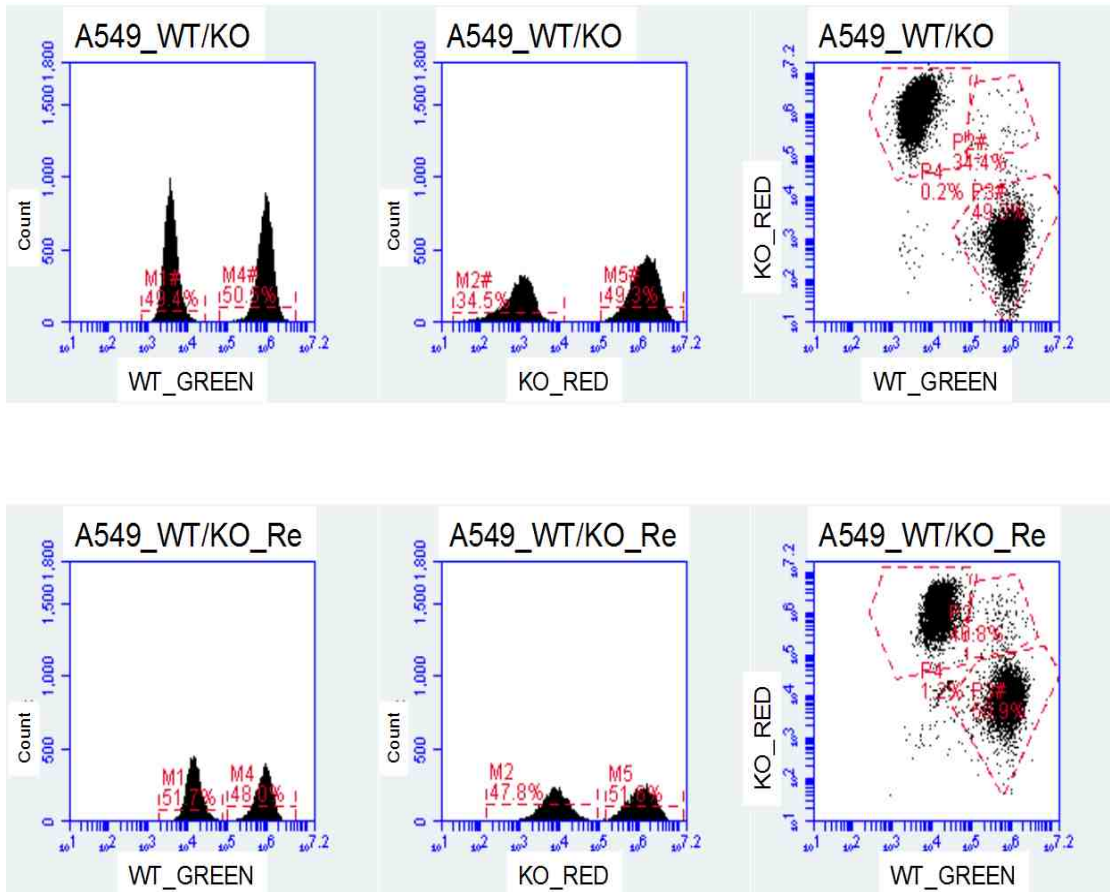


**Figure 6.6 A549 KO Qualitative 3D Growth Assay.** Qualitative growth curve using microscopy of A549 KO cell encapsulating droplets generated by centrifugal droplet synthesis from a 7-day growth experiment to observe droplet stability and cell growth over time. The population is analyzed using ImageJ to measure the geometric mean diameter, standard deviation, aspect ratio, and coefficient of variation of the culture.

quantitative cell counting to be implemented into daily time points, the initial concentration of the cells/drop should be measured at  $t_0$  and the concentration of droplets in the 125 mL spinner flask bioreactor should be estimated to make sure that a large enough population of cells is recovered from droplets at each subsequent time point such that the cell count is above the limit of detection of the cell counter and the number of cells/droplet can be approximated. These types of measurements are quite feasible, as recovering the cells from the droplets is a very straightforward chemical dissolution process where the droplets with cells are washed using a 0.5% trypsin, 50 mM sodium citrate, 25 mM HEPES, 150 mM NaCl pH 7.4 dissolution buffer for 20 minutes and centrifuged at 2000 RPM for 10 minutes to pellet the cells. The pellet is resuspended in PBS and cells are counted on the Coulter Counter. Validation studies have been accomplished where a cell population is counted before and immediately after cell encapsulation to demonstrate reproducible recovery of 98% of the cell population indicating minimal cell loss. This same protocol is used in the experiments described below to recover cells from droplets for measurement of the cell population by flow cytometry.

An additional proof-of-principle study for the use of membrane fluorescence dye dilution curves to measure the doubling time of cells encapsulated in a 3D coculture has also been completed. Referring back to Figure 6.2, the cell population to be encapsulated is stained with the respective fluorophore before centrifugal droplet generation. An important experimental note is that the wash steps after staining but before the cells are processed into a single cell suspension in 4% ALG pre-gel are extremely important in this instance, as they are required

to remove all residual fluorescence staining buffer included with the kits known as “Diluent C”. This additive is intended to help increase efficiency of cell staining, but even small residual amounts can cause slight foaming of the alginate solutions and negatively interferes with droplet generation. Thus, for the studies shown here, two extra wash steps are implemented into the protocol using the standard physiological buffer. Figure 6.7 presents flow cytometry results obtained from measuring A549 WT and KO cells in a 50/50 coculture before encapsulation into droplets by centrifugal synthesis and after encapsulation by the recovery protocol detailed above. Although a full growth curve analysis has not been completed, these proof-of-principle studies, together with the qualitative 3D growth curve results, demonstrate the feasibility of adapting two robust and standardized 2D cell growth rate assays for use in droplet-based 3D cell cultures. These methods are an improvement over conventional methods used to measure multicellular spheroid growth.



**Figure 6.7 Coculture Proof-of-Principle Results.** Flow cytometry of A549 WT (green) and KO (red) cells stained, mixed into a coculture and encapsulated by centrifugal droplet synthesis. The top panel is the fluorescence measured on the coculture cell population before encapsulation. The bottom panel is the fluorescence measured on the coculture cell population recovered from the droplets. Each plot has two distinct populations because of the coculture nature of the experiment where the fluorescence of the dye in one channel is distinct from the autofluorescence of the cells labeled with the opposite dye. This distinct measurement of labeled cells and autofluorescent cells is possible because of the spectral separation of the dyes used in the experiment.

### 6.3 Culture of Instant Spheroids

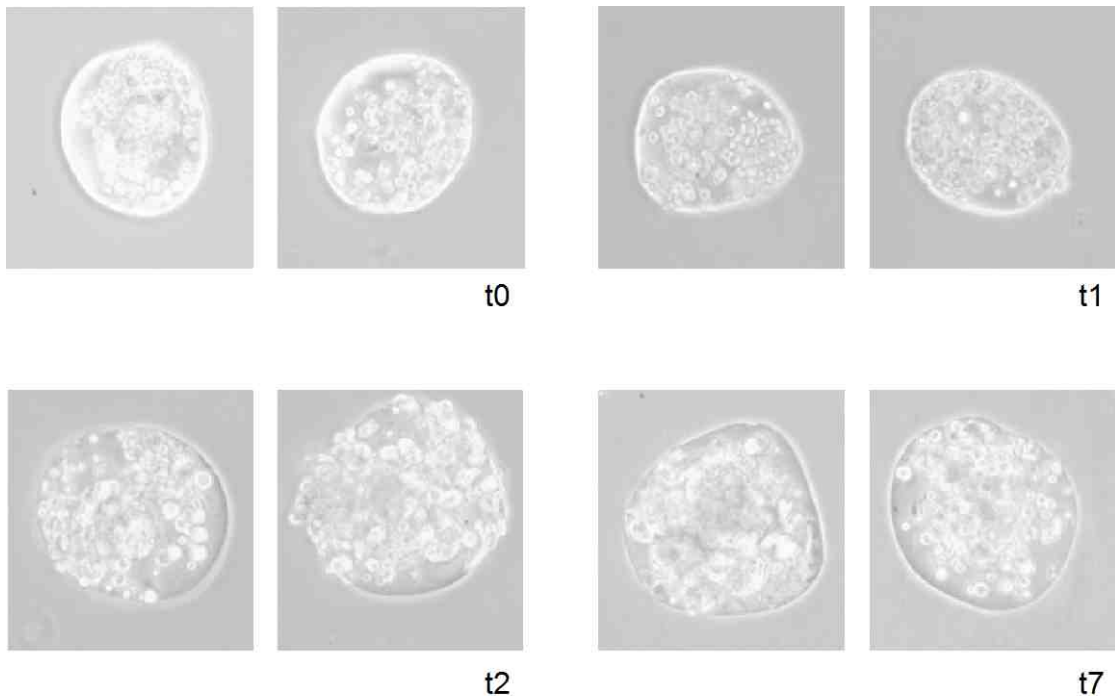
*Cell encapsulated droplets using centrifugal synthesis and hybrid nozzles at high cell occupancy concentrations produce scaffold-supported instant spheroids that are stable and show cell aggregation in suspension culture over 7 days.*

The technical ability to generate large, uniform populations of multicellular tumor spheroids generated by droplet-based methods has the potential to enable wide-spread use of 3D culture in place of less realistic alternatives. There is an economic trade-off between the supplies and equipment needed to generate and maintain 2D vs 3D cell cultures and if consistent 3D culture methodology becomes accessible, it is feasible to envision an enduring shift in the cancer research paradigm to more realistic in vitro model systems. This section builds on the instant spheroid cell encapsulation discussed in Chapter 5, and the MEL28 encapsulation preparation at high cell occupancy used here is exactly as described for 200 cells/droplet in Section 5.4. The 50  $\mu\text{m}$  hybrid nozzle/centrifuge tube assembly is operated at 1300 RPM to produce droplets that had an average geometric mean diameter of 230  $\mu\text{m}$ . Then, the instantly formed spheroids are washed out of the catch solution by allowing the droplets to settle, aspirating the solution, resuspending in 15 mL of complete media and transferring the droplets over to a spinner flask prepared as described in Section 6.2. The instant spheroid culture is maintained for 7 days with intermittent sampling to observe cell behavior in the droplets and daily media changes to maintain a stable culture environment. At day 7, there appears to be proliferation and marked aggregation of cells within the

droplet (Figure 6.8). Adapting the 3D growth curve and fluorescence membrane dye dilution curve described in Section 6.2 to measure the proliferation rate of cells in an instant spheroid is a logical and important next step for the further validation of this proof of principle experiment.

The technical ability to generate large and uniform populations of these types of cell encapsulating constructs is important for applications in high-throughput drug screening. It can take up to weeks to generate a 3D spheroid population depending on the conventional methods of formation and even then, there is likely heterogeneity in the size distribution of the population. In contrast, it takes a few hours to form a 3D cell culture population that has excellent uniformity in size and control over the cell concentration using the centrifugal synthesis method described in Chapter 5. These instant spheroid populations are more realistic models of a tumor and enable high-throughput drug screenings that are amenable to personalized medicine applications because of the quick processing. The ability to coculture in 3D applications is important for building higher order biomimetic structures that move towards an even more realistic model system. Different cell concentration ratios of genetic variant cells or tumor/stromal cells can be encapsulated and 3D cocultured. This enables the culture of mixed cell populations in identical 3D microenvironments where competitive growth rates can be measured. As growth assays are developed and standardized in 3D culture applications (i.e. the use of multicolored fluorescence dye dilution assays which are only limited by the colors available to stain the cells and the capability of the flow cytometer to conduct a multicolor assay), one can envision the generation of

multi-cultures where more than 3 cell types are encapsulated and tracked over time, which has applications at the interface of multidisciplinary fields such as immunology and cancer biology.



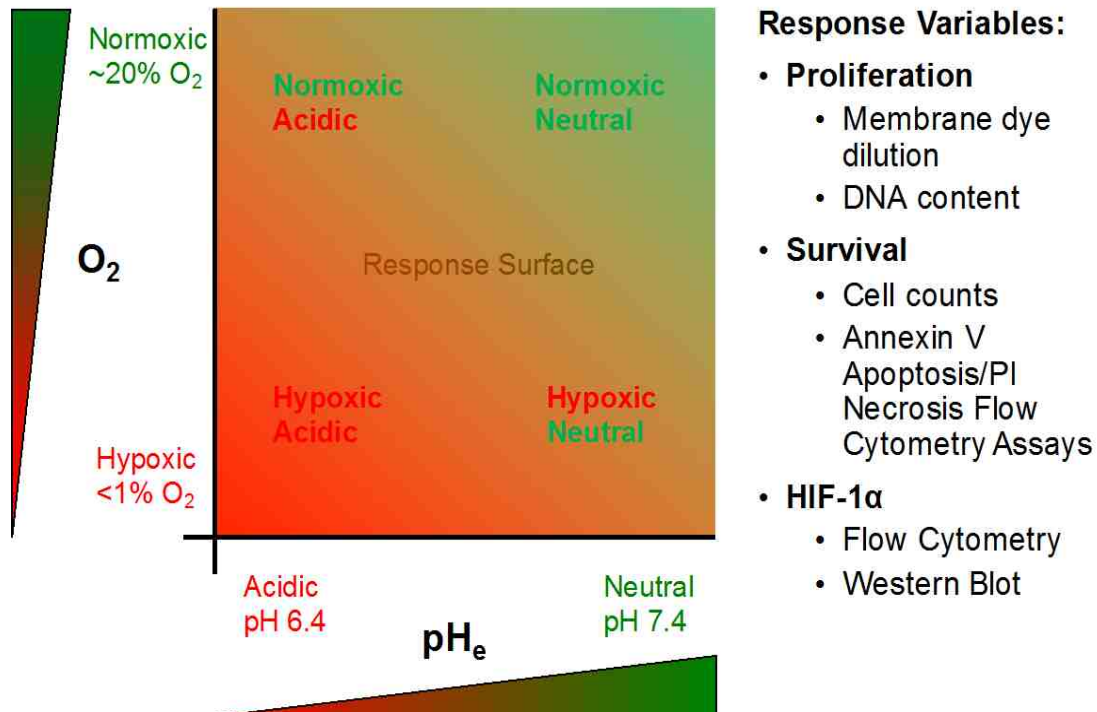
**Figure 6.8 Instant Spheroid 3D Growth Assay.** Microscopy of cell encapsulating droplets formed with high cell occupancy ( $\sim 200$  cells/droplet at  $t_0$ ) and grown in spinner flask suspension culture over 7 days. Qualitatively, there is no difference in the first 24 hours of suspension culture. After 48 hours, the cells begin to proliferate and aggregate, likely entering into an exponential growth phase and after 7 days, the aggregation is more pronounced. This experiment provides a proof-of-principle result for high cell occupancy cell encapsulation and growth in suspension culture and can now be expanded with implementation of quantitative measurement methods.



## 6.4 Altered Chemical Environments System

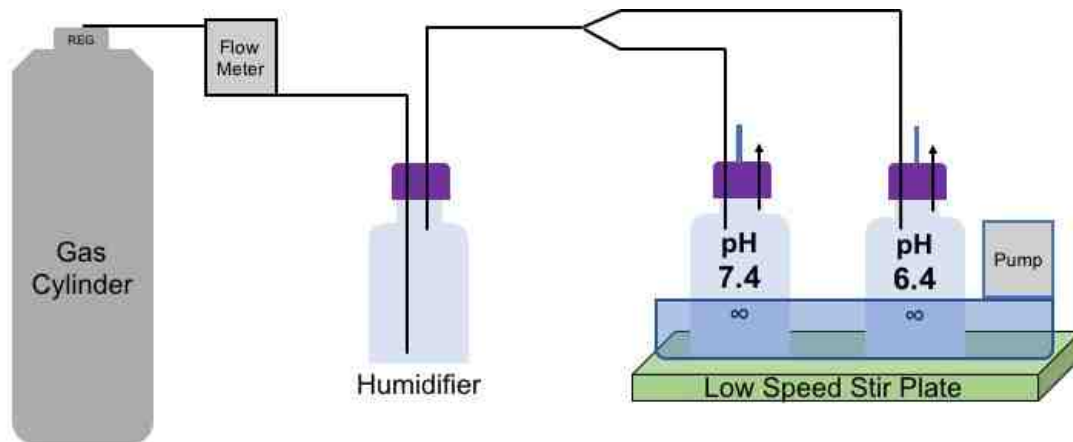
*An inexpensive, controlled, closed bioreactor system is designed to culture cells in 3D environments in combinatorial oxygen and pH environments to begin the process of investigating cellular responses to hypoxia and acidosis as mediated by HIF-1 $\alpha$ .*

By now it has been well established that current cancer research model systems, especially in 2D, do not realistically represent the biochemical microenvironment. Culture media formulations and incubation environments are designed to provide cells with (1) the minimal essential nutrients (glucose, amino acids) required to keep cells alive ex situ; (2) a sodium bicarbonate buffering system that is used to stabilize pH but can interact with other synthetic buffering systems; and (3) ambient oxygen levels that are highly nonphysiological (~21%) in comparison to a tissue (2%-9%). It goes without saying that these media and incubation conditions are nothing like the altered environmental conditions in a tumor that also exist with higher levels of complexity (e.g., with concentration gradients imposed) in 3D. This section describes initial steps and challenges towards the design and implementation of the technical ability to establish altered environmental conditions for droplet-based 3D cultures. The overarching goal is to design 3D discrete environment experiments with the ability to investigate the biomedical question discussed in Chapter 1 (Figure 6.9 depicts the 4 groups of interacting environmental parameters as well as the proposed response variables to be measured for each cell line, A549 WT and KO).

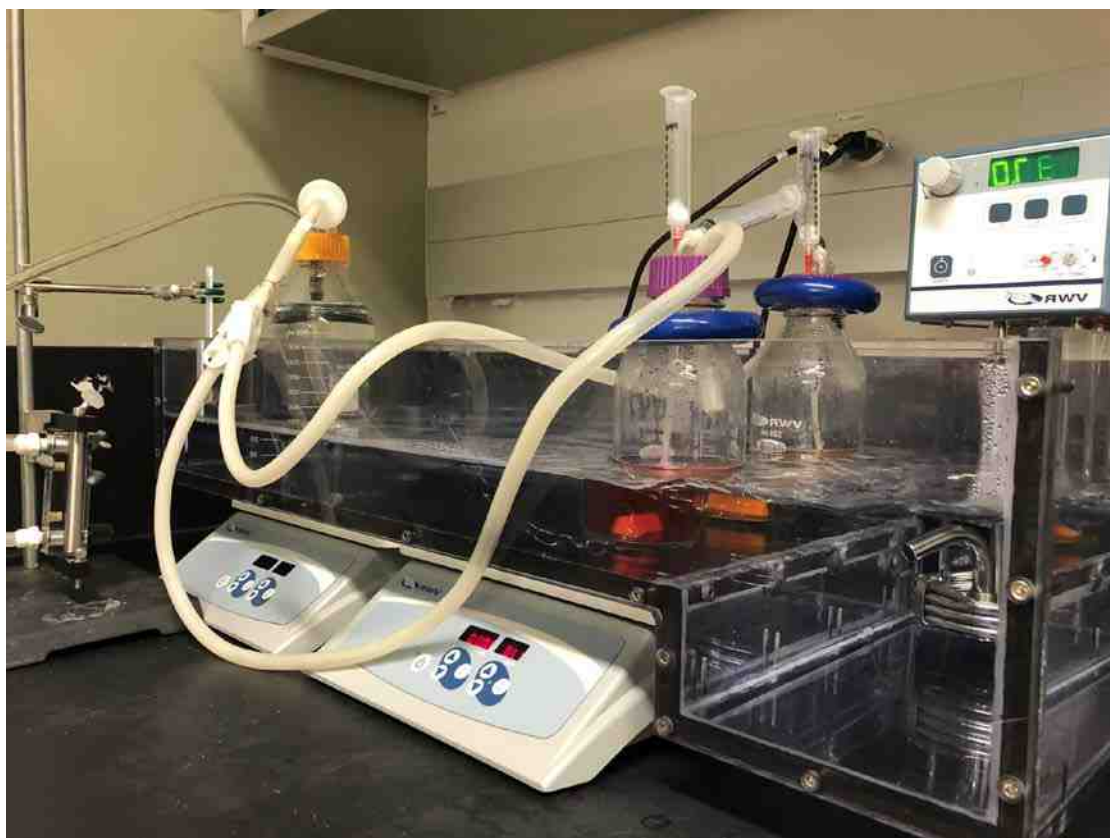


**Figure 6.9 Experimental Design for Altered Environments.** The left is a drawing of the combinatorial pH and oxygen environments to be established with A549 WT/KO cells encapsulated by centrifugal droplet generation and cultured in suspension for 24 hours. These environmental conditions establish the parameter limits for cell culture and will be amenable to establishing a functional culture system as well as provide the control groups for further investigations into the response surface. The right is a detailed list of the possible response variables and features to be measured on cell populations after recovery from droplets exposed to the altered environments. For the purpose of this dissertation, this list is simply an example of standardized experimental parameters that will enable the correlation of environmental parameters to cellular physiology.

The system designed to enable altered environment experiments is inexpensive and simple but allows comprehensive investigation of conditions so that stable cultures may be run in parallel under different environments. In addition, collection and processing of samples is easy as well as sterile. The bioreactors are constructed using 500 mL glass flasks (VWR) with modified caps to implement tubing ports for gas flow into the head space of the flask, a sampling line, and an off-gas line. All tubing and connectors used are selected to have low oxygen permeability so that leakage into the gas line during anoxia experiments is not an issue. Moreover, these components meet the specification of being sterilizable by autoclaving (Tygon E-3603 1/4" and 1/16" hose barb size/autoclavable and connectors from Cole-Parmer). The gas flow line is simply 1/4" ID tubing tightly threaded through a drilled hole in the cap and measured so that the tubing end is suspended above the media level in a flask during an experiment. The sample line is a 1/16" ID tubing threaded through a second hole drilled into the cap and measured to extended to the bottom of the flask. The exterior end of the tube is connected to a hose-barb Luer-Lok connector threaded onto a 10 mL syringe (BD) so that samples may be drawn up into the syringe without disturbing the equilibrated culture environment during an experiment. Finally, the off-gas line is made by drilling a third, small hole in to the cap and inserting an 18G needle. A 10 mL syringe with a small piece of cotton and without the plunger is attached to give a gas permeable buffer zone for the off-gassing while maintaining a sterile environment. Simple estimates of gas flow conditions and diffusional transport verify the ability to maintain equilibrated anoxic (or reduced oxygen) environments,



Normoxic: 5%CO<sub>2</sub> BAL-AIR  
 Hypoxic (anoxic): 95% N<sub>2</sub> 5%CO<sub>2</sub>

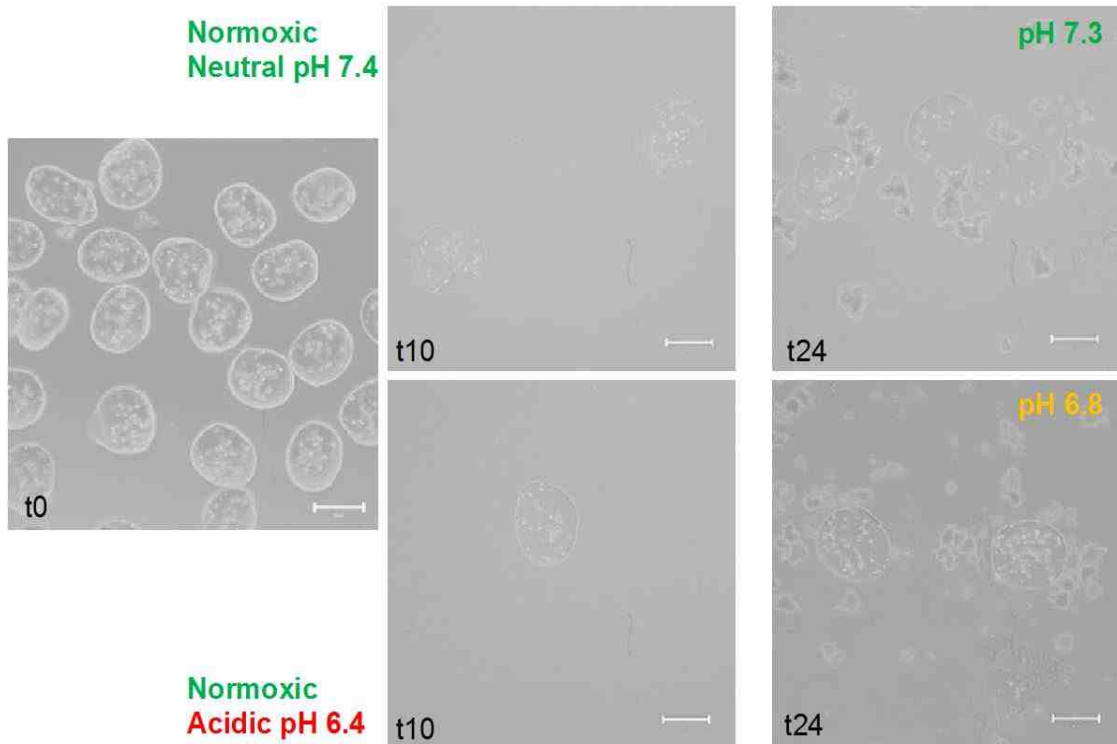


**Figure 6.10 Experimental system for altered environments.** Top is the drawing of the system and bottom is a picture of the system on the benchtop with two flasks operating.

depending on the composition of the gas mixture used. The suspension cultures are maintained by low speed stir plates (VWR) with triangular stir bars for gentle mixing and temperature is regulated by placing the culture flasks in an in-house fabricated Plexi-glass water bath with a circulating heating pump set to 37°C (placed on top of the magnetic stir plates). For the studies reported here, gas flow into the flasks is supplied by either a 5%CO<sub>2</sub> BAL-AIR (normoxia) cylinder or by a 5%CO<sub>2</sub>/95%N<sub>2</sub> cylinder (anoxia) (Argyle) that is connected with tubing to a flow meter (VWR). After the flow meter, the gas is humidified by passing through a water bubbler, also sitting in the water bath, followed by passage through an in-line flow filter and circulation into the culture flasks (Figure 6.10). The system has been designed to operate 8 culture flasks in parallel using an in-house fabricated gas manifold constructed from tubing tee-connectors and is easily controlled by changing the orientation of the manifold or by simply using hose-clamps to regulate the gas flow. Finally, before an experiment begins a sterile environment for cell culturing in the bioreactor flasks is created by autoclaving the entire bioreactor apparatus including assembled flasks with tubing, syringes, needles, stir-bars, and tubing adaptors, which makes using autoclavable components essential to the design considerations.

The media formulations have been the most challenging aspect of implementing these altered environment experiments. Initially, complete cell culture media with an extra synthetic buffer added in moderate concentration was used to produce two pH environments using 25 mM HEPES for pH 7.4/neutral experiments and 25 mM MES for pH 6.4/acidic experiments. These two media

groups were adjusted to the desired pH after the addition of the buffer under ambient gas conditions (i.e. open to the air). However, as described below, a complicating factor is that CO<sub>2</sub> gas flow in combination with the sodium bicarbonate buffer system interacts with the other added buffers, in some cases leading to subsequent changes in pH. In the above case, the 250 mL volumes of the respective neutral or acidic media were added to two 500 mL culture flasks assembled for gas flow and allowed to sit under gas flow for 12 hours. After this time, cells were added as follows. A549 WT cells were encapsulated into droplets using 50 µm hybrid nozzle centrifuge tube assemblies operated at 1100 RPM (detailed description in Chapter 5). The cell encapsulating droplets were washed and resuspended into 10 mL of media from the preequilibrated flasks using the sampling line and then injected into the culture flasks to establish normoxic/neutral and normoxic/acidic altered environment conditions. The initial droplet population was imaged using brightfield microscopy and measured by ImageJ analysis to have a geometric mean diameter of 222 µm, 2%CV. Samples were taken from each culture flask at 10 hours and after 24 hours the experiments were terminated. At the 24-hour end point, some precipitates had formed in both culture conditions and the pH of each culture was remeasured and found to have drifted (Figure 6.11). After further investigation into the sodium bicarbonate buffering system, it was found that there is an equilibrium interaction between the sodium bicarbonate and the added pH buffers. In the case of the normoxic/acidic condition, which showed a larger shift in pH after 24-hour from 6.4 to 6.8, the concentration of bicarbonate ion in the cell growth media interacting with 5% CO<sub>2</sub> gas, over time,



**Figure 6.11 Preliminary Altered Environments Results.** Microscopy of A548 WT cells encapsulated by centrifugal droplet generation and grown in altered environment suspension culture for 24 hours. The left image shows the droplets immediately after generation. The middle and right show the droplets sampled from normoxic/neutral conditions (top) and normoxic/acidic conditions (bottom) over 10 hour and 24 hours. After 24 hours in culture it appears that the pH was slightly destabilized due to the sodium bicarbonate buffering system interacting with the additional synthetic pH buffers added to the media. In addition, some precipitates were apparent, believed to be due to the interaction of the bicarbonate/carbonate equilibrium interacting with  $\text{Ca}^{2+}$  ions leached out of the crosslinked alginate droplets.

leads to a substantial modification of the pH away from the originally established value of 6.4. This likely occurred because the initial media was pH adjusted under ambient conditions and not under gas flow. In the long run, and as discussed below, the more problematic matter is the formation of precipitates that were observed to form after 24 hours in culture with the calcium alginate droplets. These are hypothesized to be caused by an interaction of the carbonic acid/bicarbonate/carbonate buffer system with calcium ions, where, depending on pH and added bicarbonate concentration, the formation of very insoluble calcium carbonate is possible. In this case, the source of the calcium ions is likely the cross-linked calcium alginate, as described below.

The shift in pH and formation of precipitates in the media motivated an investigation into using powdered media (MEM with L-glutamine, Sigma Aldrich) without sodium bicarbonate to create complete media solutions with better equilibrated buffering systems. These media were prepared by dissolving 11g/L of the powdered media into 1 L of Millipore water with 26 mM sodium bicarbonate and 25 mM HEPES for the neutral formulation adjusted to pH 7.4 and 2.6 mM sodium bicarbonate with 25 mM MES for the acidic formulation adjusted to pH 6.4 (all media sterilized by 0.2  $\mu$ m filtering through a Nalgene bottle top filter assembly). In both cases, the bicarbonate concentration was chosen to provide optimal buffering at pH values matching the desired 7.4 or 6.4, respectively. The 4 culture flasks were equilibrated for 12 hours under humidified normoxic gas flow and in the water bath. This time, A549 WT and KO cells were encapsulated as before and processed for suspension into their respective altered environmental



conditions as follows: WT and KO each in normoxic/neutral flasks as well as WT and KO each in normoxic/acidic flasks. The cell encapsulating droplets were injected into the culture flasks and sampled after 12 hours. The pH remained stable under these conditions. However, at that time, the media in all groups was found to have developed a striking cloudy white consistency, so in this group of experiments 12 hours became the end point. Samples were observed by bright field microscopy and found to contain distinct crystalline structures, with essentially complete disintegration of the alginate droplets. A likely explanation is the interaction of calcium ions initially localized in the cell encapsulating droplets with carbonate ions to form insoluble calcium carbonate precipitate, but the detailed chemistry involved and the dependence of these observations on the presence of continuously flowing CO<sub>2</sub> or specific growth media composition is a matter of ongoing investigation. For future experiments and for the standardization of 3D culture environments, particularly for those under altered culture conditions, it is paramount to have a comprehensive understanding of all cell culture conditions, including media formulations, incubation environments and buffering systems. Once a comprehensive system is implemented, it will then be feasible to investigate the interacting parameters such as those suggested by our exemplary biomedical question concerning HIF-1 $\alpha$ , hypoxia, and acidosis.

## 6.5 Discussion and Future Directions

This chapter explored the design and implementation of standardized 3D culture methodology and applications that are enabled by the technical ability to generate large populations of controlled cell encapsulating droplets. Growth assays on two model cell lines with a HIF-1 $\alpha$  WT and KO phenotype were completed as reference experiments for using growth curves and fluorescence dilution curves to measure proliferation rates in mono and cocultures. The adaptation of 2D cell culture growth assays to 3D mono and cocultures was validated by proof-of-principle studies that demonstrated: (1) qualitatively measured growth of A549 WT and KO cells encapsulated at initial low cell occupancy over 7 days in suspension culture and (2) the ability to adapt a membrane fluorescence dilution assay to a 3D coculture by recovering cells from encapsulating droplets and conducting a two-color fluorescence assay by flow cytometry to measure and differentiate two populations of cells from the same coculture. Cells were also encapsulated at high cell occupancy to produce instant spheroids and were demonstrated to be viable in standard suspension culture conditions for 7 days. Finally, steps toward creating a 3D cell culture system with controlled altered environments was designed and implemented. The interaction between the media and atmospheric conditions required for creating altered environmental conditions for 3D cell culture is in progress and once complete, will make a significant contribution to multidisciplinary fields interested in creating culture conditions that are more realistic for modeling the chemical tumor microenvironment.

## 6.6 List of References

- (1) Horvath, P.; Aulner, N.; Bickle, M.; Davies, A. M.; Del Nery, E.; Ebner, D.; Montoya, M. C.; Östling, P.; Pietiäinen, V.; Price, L. S.; Shorte, S. L.; Turcatti, G.; Schantz, von, C.; Carragher, N. O. Screening Out Irrelevant Cell-Based Models of Disease. *Nature Publishing Group* **2016**, *15* (11), 751–769.
- (2) Eagle, H. Buffer Combinations for Mammalian Cell Culture. *Science* **1971**, *174*, 500–503.
- (3) Eagle, H. Nutrition Needs of Mammalian Cells in Tissue Culture. *Science* **1955**, *122*, 501–504.
- (4) Muir, A.; Vander Heiden, M. G. The Nutrient Environment Affects Therapy. *Science* **2018**, *360* (6392), 962–963.
- (5) Morgan, R. A. Human Tumor Xenografts: the Good, the Bad, and the Ugly. *Molecular Therapy* **2009**, *20* (5), 882–884.
- (6) Lee, J.; Kotliarova, S.; Kotliarov, Y.; Li, A.; Su, Q.; Donin, N. M.; Pastorino, S.; Purow, B. W.; Christopher, N.; Zhang, W.; Park, J. K.; Fine, H. A. Tumor Stem Cells Derived From Glioblastomas Cultured in bFGF and EGF More Closely Mirror the Phenotype and Genotype of Primary Tumors Than Do Serum-Cultured Cell Lines. *Cancer Cell* **2006**, *9* (5), 391–403.
- (7) Nath, S.; Devi, G. R. Three-Dimensional Culture Systems in Cancer Research: Focus on Tumor Spheroid Model. *Pharmacology & Therapeutics* **2016**, *163*, 94–108.

- (8) Weiswald, L.-B.; Bellet, D.; Dangles-Marie, V. Spherical Cancer Models in Tumor Biology. *Neoplasia* **2015**, *17* (1), 1–15.
- (9) Yamada, K. M.; Cukierman, E. Modeling Tissue Morphogenesis and Cancer in 3D. *Cell* **2007**, *130* (4), 601–610.
- (10) Knight, E.; Przyborski, S. Advances in 3D Cell Culture Technologies Enabling Tissue-Like Structures to Be Created in Vitro. *J. Anat.* **2014**, *227* (6), 746–756.
- (11) Moshksayan, K.; Kashaninejad, N.; Warkiani, M. E.; Lock, J. G.; Moghadas, H.; Firoozabadi, B.; Saidi, M. S.; Nguyen, N.-T. Spheroids-on-a-Chip: Recent Advances and Design Considerations in Microfluidic Platforms for Spheroid Formation and Culture. *Sensors & Actuators: B. Chemical* **2018**, *263*, 151–176.
- (12) Alessandri, K.; Sarangi, B. R.; Gurchenkov, V. V.; Sinha, B.; Kiessling, T. R.; Fetler, L.; Rico, F.; Scheuring, S.; Lamaze, C.; Simon, A.; Geraldo, S.; Vignjevic, D.; Domejean, H.; Rolland, L.; Funfak, A.; Bibette, J.; Bremond, N.; Nassoy, P. Cellular Capsules as a Tool for Multicellular Spheroid Production and for Investigating the Mechanics of Tumor Progression in Vitro. *Proceedings of the National Academy of Sciences* **2013**, *110* (37), 14843–14848.
- (13) Freyer, J. P. Role of Necrosis in Regulating the Growth Saturation of Multicellular Spheroids. *Cancer Research* **1988**, 2432–2439.
- (14) Jensen, M. M.; Jørgensen, J. T.; Binderup, T.; Kjær, A. Tumor Volume in Subcutaneous Mouse Xenografts Measured by microCT Is More

Accurate and Reproducible Than Determined by 18F-FDG-microPET or External Caliper. *BMC Med Imaging* **2008**, 8 (1), 229–229.

- (15) Chen, Y.; Chen, X.; Li, F.; Ji-an, L. Delineation Gross Tumor Volume Based on Positron Emission Tomography Images by a Numerical Approximation Method. *Ann Nucl Med* **2014**, 28 (10), 980–985.
- (16) Chung, S.; Kim, S.-H.; Seo, Y.; Kim, S.-K.; Lee, J. Y. Quantitative Analysis of Cell Proliferation by a Dye Dilution Assay: Application to Cell Lines and Cocultures. *Cytometry* **2017**, 91 (7), 704–712.

## **Chapter 7**

### **Conclusion of the Dissertation**

## 7.1 Concluding Remarks for the Dissertation

The over-arching motivation of this dissertation is that improvement in 3D cell culture methods by cell encapsulation in droplets will enable more controllable and realistic investigations of the heterogeneous environments in which cancer develops. Each chapter has contributed to the investigation of this high-level theme. Robust technological developments have been established for the generation of droplets encapsulating cells and steps toward realizing and implementing what is needed to create more realistic cell culture conditions have been discussed. The following Specific Aims have been achieved:

***Specific Aim 1: Development and implementation of droplet generation technologies for cell encapsulation***

Droplet generating instrumentation and methodology has been developed and demonstrated to encapsulate cells for 3D cell culture through the design and implementation of three droplet generating platforms.

High-throughput droplet generation in the air was addressed in Chapter 3. The work in Chapter 3 focused on the design and implementation of instrumentation built from the bottom-up to generate droplets at high rates with highly optimized device parameters for two different device designs (dual and single channel device arrangements). Biocompatible chemistries were investigated using straight alginate gelation as well as water-in-water aqueous two-phase separation chemistry (ALG/PEG-in-DEX/Ca<sup>2+</sup>). Two collection mechanisms were implemented and characterized, those being droplet collection in a stirring collection solution and by rigid body rotation, the latter of which is novel and shows

great promise for future experimentation. Although the instrumentation platforms designed in Chapter 3 demonstrated droplet generation using highly viscous fluids, flow and modulation rates, and sizes in the air that have yet to be observed when using other methods with similar sized nozzles, the challenge of collecting perfectly spherical particles with encapsulated cells was not fully overcome because of the high-speed generation rate of droplets in all of the design iterations and collection mechanisms investigated. However, there were still technical advancements made and all of the expertise and knowledge gained enabled the designs, technology implementation, and results presented in the subsequent chapters. Finally, some advancements have been made with the further characterization of the aqueous two-phase separation chemistry (detailed in Chapter 4) that is hypothesized to enhance the sphericity in collection of high-throughput acoustically generated droplets and possibly enable cell encapsulation using this platform.

Microfluidic droplet generation using acoustics and redesigned aqueous two-phase separation chemistries is addressed in Chapter 4. The work in Chapter 4 was a highly collaborative effort that focused on the encapsulation of cells by generating water-in-water droplets in a microfluidics device where the break-up of the immiscible flow streams within the device was modulated by a speaker. The aqueous two-phase separation chemistry was investigated further and an improved protocol for preparing enriched solutions of phase separated PEG and DEX was developed. These enriched polymer solutions (characterized and validated with rheology and index of refraction investigations) were then used in the microfluidics device with speaker modulation to optimize the system for flow



rate and frequency combinations that produced monodispersed populations of droplets both with and without cells. The system was then used to demonstrate the encapsulation of EMT6 mouse mammary carcinoma cells and suspension culture over 9 days, using a robust protocol developed to initially make a single cell suspension within a highly viscous biomaterial and validated to be a biocompatible approach by LIVE/DEAD assay. Cell proliferation within the droplets was observed with microscopy of the droplets at time points over the 9-day interval and the method was demonstrated to be a robust and viable technology to encapsulate and culture cells in 3D.

Centrifugal droplet generation for mass production of cell encapsulating droplets is presented in Chapter 5. The work in Chapter 5 expands the application space of preexisting centrifugal tube assembly methodology for droplet generation by implementing the design and construction of hybrid glass capillary/needle nozzles to control the diameter of the nozzle that ultimately influences the droplet diameter of the population produced. This improved droplet generation method is validated and optimized by investigating the artificial gravity under which the droplets are generated using the smallest gauge needle in comparison to hybrid (glass capillary/needle) nozzles, which have a radius of nearly half that of the commercially available needles. Improved droplet generation was demonstrated by measuring the populations of droplets generated over a range of centrifugal forces with both types of nozzles and showing that the hybrid nozzle enabled smaller sized and monodispersed droplet populations under equivalent generation conditions. The generation of cell-sized droplets using a hybrid nozzle with a small

(5-7  $\mu\text{m}$ ) diameter nozzle was investigated and demonstrated the new ability to generate alginate droplets down to a size range of 25-40  $\mu\text{m}$  diameter. These droplets that are produced with a size on order of a large cell are a highly desirable platform for applications in cell-free systems such as the stabilization of vesicles, proteins, and other biomolecules outside the context of cellular compartmentalization. Centrifugal droplet generation using the hybrid nozzle was demonstrated to be a viable technology for the encapsulation of a range of cell types and concentrations. This centrifugal droplet formation technology became the preferred method of generation for the development of biological assays in Chapter 6 because of the reproducibility in device operation, high-throughput mode of droplet generation, adaptability to any desired format of cell encapsulation for 3D culture, and the strikingly monodisperse droplet populations produced.

***Specific Aim 2: Development of standardized biological assays to measure droplet-based 3D cell cultures***

Chapter 6 demonstrated the development of cancer research applications to measure qualities of cells that have been encapsulated and grown (using the approaches described in Specific Aim 1). Chapter 6 presents the development, implementation, and in some instances challenges of creating standardized biological assays for 3D cell culture. Proliferation assays in 2D and proof-of-principle adaptation to 3D cell mono- and co-cultures was presented and demonstrates a feasible method of measuring cell growth for multiple cell types. The growth and fluorescence dilution assays establish improved 3D cell culture protocols that have a high probability of easily being adapted into standard lab

practices and in more complex 3D constructs. The formation of multicellular tumor spheroids either instantly by initial high cell loading in droplets or over time with initial low cell loading was demonstrated using droplet generation methods established in Chapters 4 and 5. Finally, a 3D suspension culture system with altered biochemical microenvironments was built and the validation process is currently under way. In addition, the implementation of this new technology is discussed in the context of the cancer research question posed in Chapter 1 involving the HIF-1 $\alpha$  mediated responses to both coupled and uncoupled variations of hypoxia and acidosis. Evaluating the technology and assay development presented in this dissertation through the lens of a relevant and currently unanswered multiparametric cancer research hypothesis provides a compelling reason for the overall effort.

In summary, Specific Aim 1 was successfully accomplished through the improvement and advancement in droplet generating technologies for cell encapsulation. The three droplet generation platforms described in Chapters 3, 4, and 5 make advancements in multidisciplinary fields. The knowledge gained by the individual dynamics investigated in each droplet generation method will enable the continued development of improved cell encapsulation strategies. Specific Aim 2 was accomplished by generation of viable 3D constructs and measurement techniques for use in advanced cell culture systems. The findings presented in this dissertation have implications for the future development of 3D cell culture in terms of overall cost, high throughput operation, monodispersity, biocompatibility, and widespread implementation of the technology.